Energy and Feasibility Analysis of Gasoline Engine Start/Stop Technology

Undergraduate Honors Thesis

Presented in Partial Fulfillment of the Requirements for

Graduation with Distinction

at The Ohio State University

By

Luke A. DeBruin

* * * * *

The Ohio State University

2013

Defense Committee:

Professor Marcello Canova, Research Advisor

Dr. Shawn Midlam-Mohler, Capstone Advisor

Abstract

The national mandate set forth by the Environmental Protection Agency (EPA) to increase fuel efficiency and reduce greenhouse gas (GHG) emissions by 5% each year for all new model mid-size cars, medium-duty cars, and light-duty trucks is pushing automobile makers to convert their fleets to hybrid-electric and micro-hybrid vehicles. Implementing automated start/stop (SS) technology in a passenger vehicle is a cost effective way to improve fuel economy (FE) and reduce emissions without affecting consumer acceptance. In urban areas, where much of the vehicle driving time is spent idling at stop lights or in traffic, the engine can be shut down when the vehicle is stopped to save fuel. Then, the engine is quickly and quietly restarted as the driver demands torque for acceleration. This operating strategy is often utilized in full hybrid-electric vehicles that have powerful electric systems, but is becoming more popular in micro-hybrid vehicles that use traditional starter/battery configurations. It is challenging to maintain drivability and achieve efficient startups using a micro-hybrid configuration. This research investigated the feasibility of using a micro-hybrid configuration to achieve efficient start transients for SS technology. The energy consumption of the starter/battery was analyzed by creating a model of the engine SS dynamics. The model was calibrated and validated through experimental testing on a vehicle and engine that had been provided. The model was used to simulate start transients for different component packages. Preliminary simulation results suggest that traditional starter/battery combinations may be appropriate and a fuel savings of over 5% may be expected in regulatory urban driving cycles. The model and selected component package will be used for development and control of a SS system in a test vehicle.

Acknowledgements

I would like to thank Dr. Giorgio Rizzoni for sparking my interest in system dynamics and for extending the invitation to complete an honors undergraduate research project with the Center for Automotive Research. Special thanks go to my mentor, Professor Marcello Canova, for the time and effort he has committed to help me complete this research, and for providing to me the diesel engine dynamics model, upon which the startup model of this research is based. I would also like to thank research scientists Dr. Fabio Chiara and Dr. Lisa Fiorentini for their help and support to understand the subject matter surrounding my research. Thanks to Neeraj Agarwal for the time he spent discussing and explaining his research to me; these talks ultimately led me to join the Chrysler Project. Ben Grimm's analysis of start/stop using the VES provided instrumental motivation for this work; thanks to him for the extra time he committed to produce those results. Finally, I would like to thank graduate students Kyle Merical, Jeremy Couch, Sandeep George, and Saba Gurusubramanian for teaching me about the engine and chassis dynamometers and for helping me collect the experimental data used in this research.

Table of Contents

Page

List of Tables

List of Figures

Chapter 1: Introduction and Background

1.1 Broader Impact

In response to President Obama's May 2010 directive to reduce greenhouse gas (GHG) emissions and fuel consumption (FC), the National Highway Traffic Safety Administration (NHTSA) and the Environmental Protection Agency (EPA) are mandating an increase in fuel economy (FE) and reduction of GHG emissions by 5% each year for all new model mid-size cars, medium-duty cars, and light-duty trucks [1]. National mandates like this, along with rising fuel prices, continue to push the automotive industry to improve its corporate average fuel economy (CAFE).

By 2025, the fleet-wide average FE will by 54.5 miles per gallon (mpg). Mid-size and medium-duty cars will jump from 32 mpg as of 2012, to 62 mpg in 2025. The FE of light-duty trucks will go from the 26 mpg in 2012, to 44 mpg by 2025. In order for new vehicles to reach these standards, the average price of a vehicle in 2025 will increase by about $1800. However, a family that purchases a new vehicle in 2025 will save $8200 in fuel costs compared to a similar automobile in 2010 [2] .

Automakers are reaching out to find new ways to quickly and affordably stretch the fuel economy of their vehicles to meet the new standards. Improvements are being made to the engines, transmissions, and auxiliary loads of conventional vehicles. Many manufacturers are beginning to produce hybridized vehicles where much of the powertrain architecture and auxiliary loads of the vehicle are electrified. This increases the vehicle efficiency because of the potential to recuperate energy that is otherwise lost in a traditional vehicle structure. Precise

control of electrified components also minimizes losses during driving to improve overall vehicle efficiency. An overview of the varying degrees of hybridization for current production automobiles is shown in Table 1.

There are significant inefficiencies associated with the conversion of fuel energy into the final motive force that drives a vehicle. Figure 1 shows a breakdown of the energy losses for a mid-sized sedan over the EPA Urban and Highway drive cycles. After accounting for all of the energy losses involved in converting the fuel into useful energy, called brake energy in vehicles, only around a quarter of the original energy is available to drive the vehicle. Propulsion related improvements can be made to reduce the losses related to the conversion device itself, which is the engine. However propulsion improvements fall outside of the scope of this work.

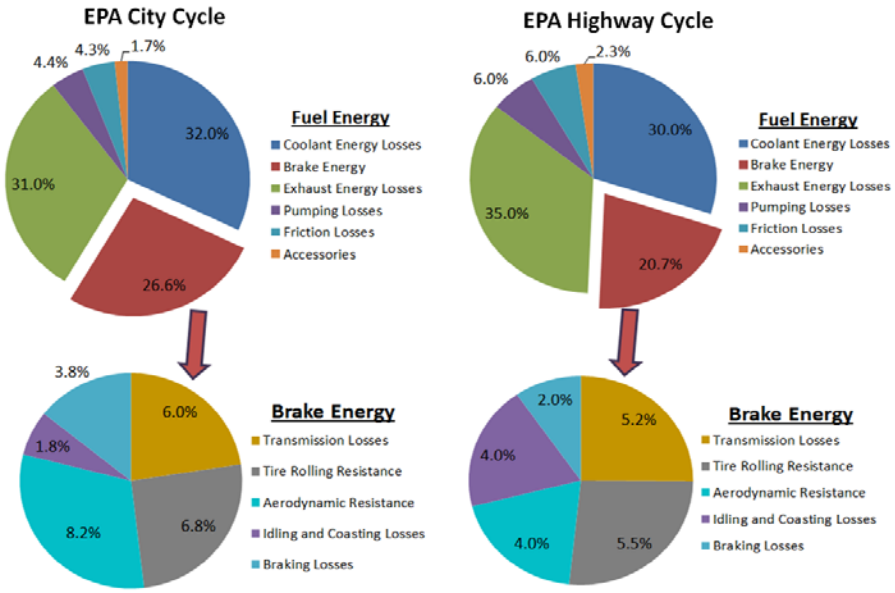

Figure 1: Energy Usage in a Mid-sized Sedan during the EPA City and Highway Cycles [3]

A small portion of the non-propulsion related losses linked with the brake energy are due to engine idling and vehicle coasting. The focus of this work was to eliminate the vehicle idling losses during the EPA Urban drive cycle by using start/stop (SS) technology.

1.2 State of the Art

Start/stop (SS), sometimes termed idle-stop or auto start-stop, is a vehicle operating strategy that shuts down the engine during periods when the vehicle is not moving. This eliminates the fuel consumption that would normally be spent to keep the engine running. During idle periods the engine is not providing any useful energy to move the vehicle, therefore the engine is technically operating at a zero efficiency state. However, the vehicle auxiliary loads require power even when the vehicle is stopped, making it is necessary to have a secondary energy source to meet those needs. For this reason, past use of SS technology had be restricted to hybrid powertrains with larger secondary power sources and electric machines that provided ample power for the auxiliary loads and on-demand engine restarting.

Note that it is not necessary to limit SS to hybrid powertrains, so long as proper control is exercised. Table 1 shows that SS can be used with varying levels of hybridization.

Table 1: Various Degrees of Vehicle Hybridization [4]

		Full Hybrid	Mild Hybrid	Micro Hybrid
Functions	Electric Drive	Yes	No	No
	Torque Assist	Yes	Yes	No
	Stop/Start	Yes	Yes	Yes
	Regenerative Braking	Yes	Yes	Yes (limited)
Hardware	Electric Machine	High power electric motor	CISG, BISG	BISG, ESM
	Power Source	High voltage NiMH or Li-Ion battery pack	High voltage NiMH or Li-Ion battery pack	Lead/acid batteries , Ultracapacitors
Hybridization cost		High	Medium	Low
Market		High end	High and middle end	Entry level
Examples		Ford Escape Toyota Prius Lexus RX400h	Honda Civic GM VUE	Citroen C2 BMW 1 Series

SS can be implemented across all levels of vehicle hybridization including mild and micro hybrid applications where a non-hybrid powertrain is utilized [4] [5] [6] . This can be done with only a few component modifications, which normally includes a high-power starter, appropriate electrical system, and controller. Depending on the level of hybridization, SS systems can be used in conjunction with regenerative braking and electric motor torque assist during startup to significantly increase the overall vehicle FE. In literature reviewed here, it has been seen that FE improvements can range from as little as 3% to around 20%. Various SS systems and the included components are covered in the following sections.

1.2.1 Overview of Start/Stop Systems

Many conventional vehicles, or vehicles with non-hybrid powertrains, are being equipped with SS. Because adding SS technology to a vehicle is the lowest form of hybridization these vehicles are classified as micro hybrids. Companies that have SS systems on vehicles available in the U.S. market today include Audi, BMW, Ford, GM, Honda, Kia, Mercedes-Benz, Porsche, and others. Some of these systems will be reviewed here.

Ford has introduced a SS system for their 2013 Fusion vehicle that only costs $235 to implement and has an 18 month payback [7]. This system increases the FE by 3.5%. The only added cost comes from the addition of an upgraded starter along with an electric hydraulic pump to maintain the internal pressure of the automatic transmission. The controls for the system closely regulate the vehicles auxiliary loads to determine when the SS function is appropriate to use. The controls also use voltage blending to maintain driver acceptance when SS is enabled. The electrical system is unmodified and uses a lead-acid 12V absorbent glass mat (AGM) battery, which has become the industry standard for vehicles with small SS systems. To protect the

battery from advanced aging, Ford has strict controls on the battery depth of discharge (DOD) and regulation of dynamic charge acceptance (DCA). DCA directly affects the amount of energy that the battery can accept during regenerative braking.

BMW implemented a SS system for its 3-series that uses the system to perform auto start-stop function (ASSF) and regenerative braking [8]. This system uses the traditional 12V AGM battery to gain a 3.5% increase in FE. The electrical system closely manages a partial battery state of charge (partial-BSOC) in order to maintain the battery. The BSOC range is approximately 79-85%. The only additional components for the SS system are a battery sensor and a power management software module that controls the decision making process for SS and regenerative braking. This system runs on manual transmissions where the start and stop process are shown in Figure 2. Here the engine startup and shutdown is controlled by the driver engaging and disengaging the clutch.

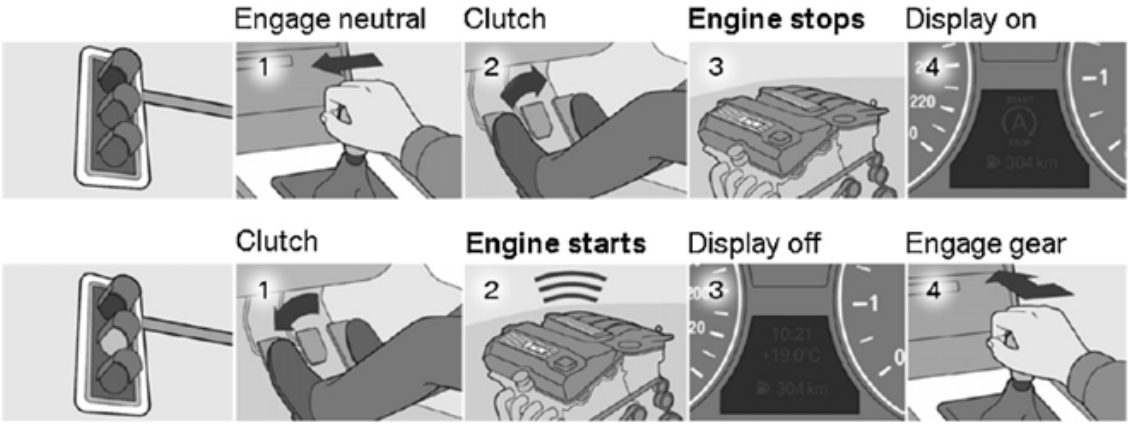

Figure 2: Start/Stop Procedure of BMW's with Manual Transmissions [8]

General Motors has had a progressive evolution of their SS system called eAssist [9], which was first used on the 2006 Saturn VUE, then the 2012 Buick LaCrosse, and most recently the 2013 Chevy Malibu. The most recent system architecture appeared on the LaCrosse and the Malibu

and is covered here. The SS system features a 15kW belted starter alternator (BSA) or belt alternator starter (BAS) that was connected to the auxiliary side of the engine by a belt transmission. The battery was upgraded from a 36V system to an 115V lithium-ion battery that can provide enhanced energy recuperation during braking along with DFSO. The electrical system contained a DC/DC converter and a DC/AC inverter in order to allow power flow to and from the BSA, high voltage battery, and low voltage battery. The SS system along with vehicle road load reductions were shown to provide a 33% increase in FE over the EPA city drive cycle.

1.2.2 Start/Stop Components

The main component in any start/stop system is the starter. This can be a conventional starter [6] [8] like that shown in inserts 2 and 3 of Figure 3 as well as an enhanced starter motor (ESM) [4].

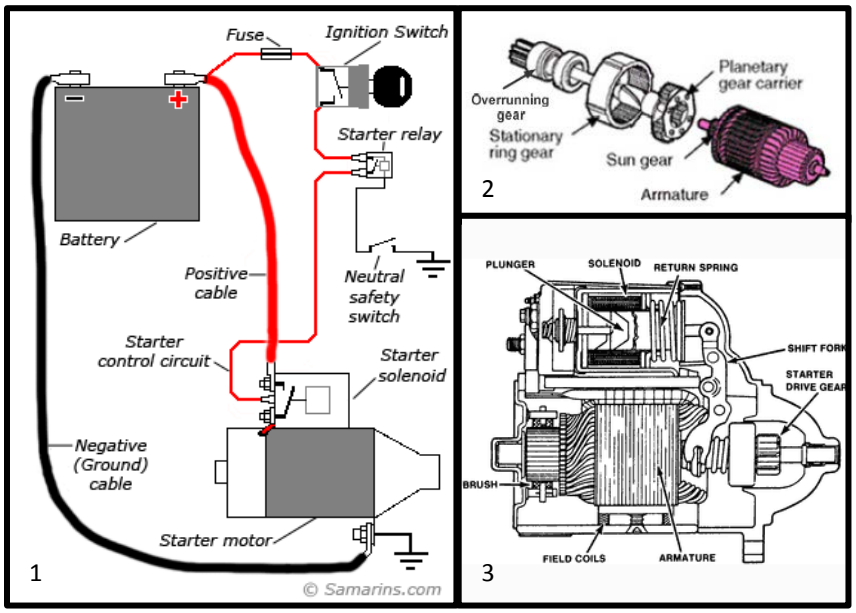

Figure 3: Overview of Starter System in a Conventional Vehicle [10][1][11][2][12][3]

These starters are mounted to the crankshaft flywheel and are generally smaller than 5 kW and provide less FE improvement compared to the larger BSAs due to lesser regenerative braking capabilities.

A robust SS system will usually require a BSA. The BSA is known by many names including BAS [9], integrated starter generator (ISG) [4], and belted starter generator (BSG) [13]. The BSA transmits power to the engine via the auxiliary serpentine belt system. Adding a BSA often requires the use of a bi-directional belt tensioning system to ensure that the belt tension is sufficient for engine starting and regenerative braking [4] [9] [13]. The power signature for a BSA normally ranges from 5 -20 kW depending on how much regenerative braking is desired and taking into account the overall cost of vehicle hybridization. Figure 4 shows the BSA that appears on the 2013 Chevy Malibu.

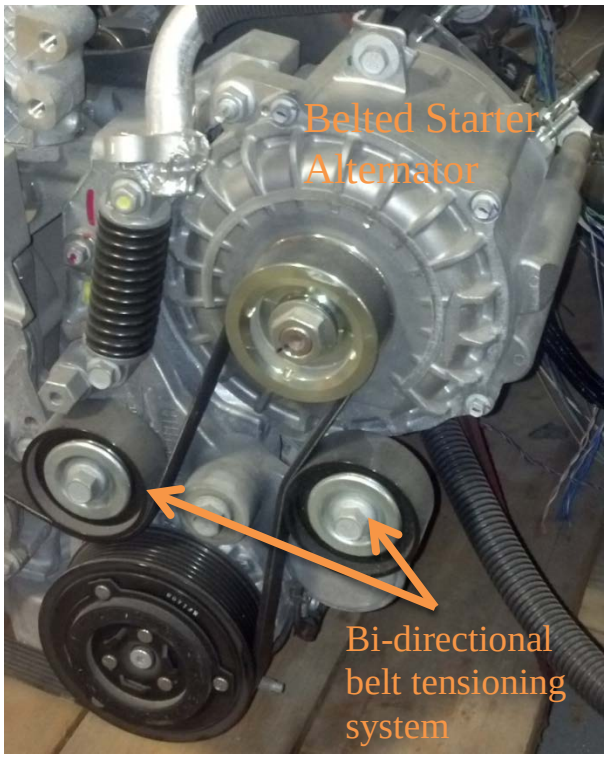

Figure 4: Belted Starter Alternator of GM's 2013 Chevy Malibu

A secondary power source is needed for SS in order to restart the engine and provide power to the vehicle auxiliary loads that run while the engine is off. During the stop, if at any point the auxiliary loads become too great or the BSOC gets too low, the engine must be restarted so that the alternator can recharge the battery and supply power to the auxiliary loads [14]. Numerous SS events can also negatively impact the battery life [8]. This makes the selection of the electrical system extremely important for successful SS operation. SS components in the electrical system may include various combinations of batteries, ultra-capacitors, battery regulators, battery sensors, controllers, DC/AC inverters, and DC/DC converters. Table 2 shows a summary of the common advantages and disadvantages for different battery compositions often utilized in vehicles.

Table 2: Summary of Battery Types [15]

Battery Type	Advantages	Disadvantages
Lead Acid	**Can be designed for high power** **Inexpensive** **Safe** **Reliable** **OLD ESTABLISHED TECHNOLOGY as starter battery**	**Poor Cold temperature Performance** **Short Calendar and Cycle Life**
Nickel- Cadmium	High Specific Energy Good Cycle life compared with lead acid	Does not deliver sufficient power
Nickel-Metal Hydride	**Reasonable Specific Energy** **Reasonable Specific Power** **Much longer cycle life than lead acid** **Safe** **Abuse-tolerant**	High Cost Heat Generation at High Temperatures Low cell efficiency Need to control Hydrogen Losses
Lithium Ion	**High Specific Energy** **High Specific Power** **High Energy Efficiency** **Good High temperature performance** **Low Self-Discharge**	Needs Improvement in: Calendar and Cycle life Abuse Tolerance Acceptable Cost Higher degree of Battery safety

The standard 12V lead-acid AGM battery, ultra-capacitor, and/or DC/DC converter are suitable for SS applications where a conventional starter, ESM, or smaller BSA is used [5] [8]. For the larger BSA it is necessary to use a high voltage NiMH or lithium-ion battery, and a DC/AC

inverter [9]. Both a high and low voltage electrical system need to be properly controlled in order to realize the maximum benefits of regenerative braking and startup torque assist. SS and regenerative braking functions cause increased cycling on the battery as well. Therefore, close regulation of the battery DCA and BSOC are needed in order to maintain battery life and prevent advanced aging. One way to slow the aging process of a 12V lead-acid battery is to periodically provide the battery a refresh charge to 100% BSOC. This prevents hard sulfation that ultimately leads to battery failure [8].

For SS systems, it is common to electrify some of the components that need to have power when the vehicle is either stopped or decelerating. This can include any or all combinations of the following components: transmission hydraulic pump, power steering pump, brake booster pump, AC pump, and accessory drive clutch. It is not necessary to electrify all the components listed in order to develop an adequate SS system. For example, sensors can be used to make sure that the brake booster vacuum stays at an acceptable level and to check the steering angle [13]. If the vacuum becomes unacceptable or driver tries to steer the vehicle while the vehicle is stopped, the SS controller can restart the engine.

1.2.3 Start/Stop Control

Sophisticated control is needed for a fuel-efficient SS system that maintains consumer acceptance, offers enhance vehicle drivability, meets emissions standards, and avoids noise, vibration, and harshness (NVH) signatures due to engine startup and shutdown. Control software must manage regenerative braking, torque assist during vehicle launch (if used), auxiliary load management, transmission operation, advanced startup firing, battery management, and SS logic algorithms. See Section 5.2 and the above references to learn more.

1.3 Chrysler Project and Scope of Work

Chrysler Project

The Center for Automotive Research (CAR) has been helping the automotive industry achieve the new CAFE standards outlined in Section 1.1 by optimizing energy management for specific research sponsors. Recently, CAR has paired up with Chrysler LLC and the U.S. Department of Energy (DOE) to achieve a 25% fuel economy improvement in an EPA City/Highway cycle for the Chrysler Town and Country minivan, through the design and integration of a supervisory controller capable of optimizing the overall energy consumption of the vehicle. Figure 5 shows the project methodology for achieving a 25% increase in FE. CAR has developed improvements in the areas of thermal management, transmission lock-up, decreased fuel shutoff (DFSO), and ancillary (auxiliary) load management. This paper covers the reduction of idling losses using SS.

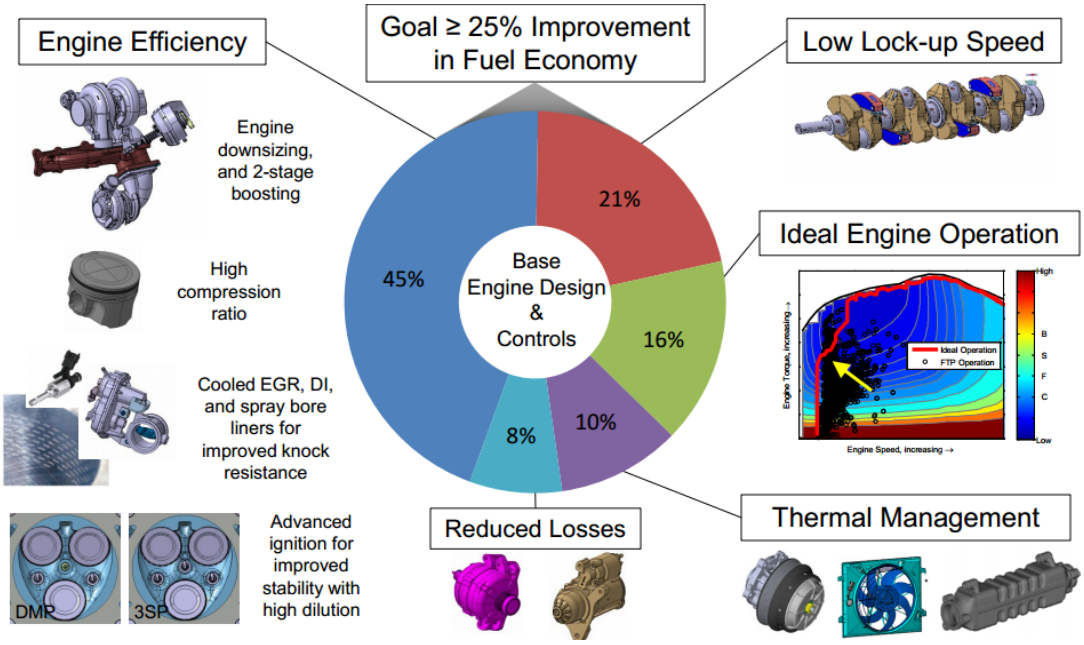

Figure 5: Chrysler Project Methodology [16]

Scope of Work on Start/Stop

There are three main considerations that need to be addressed for start/stop operation.

First, it is imperative that the SS system does not negatively impact the vehicle drivability. Therefore, NVH must be avoided when the engine stops and restarts so that the driver is not affected. The NVH related to a stop event can be minimized by lowering the intake manifold absolute pressure (IMAP) during shutdown and by using proper transmission controls [13]. The NVH signature inherent to a start event is caused primarily by engine speed overshoot and can be addressed by implemented closed loop control of the engine starter to torque cancel the overshoot [17]. The startup NVH signature associated with the engine compression events during the cranking phase can be reduced by selecting an adequately sized starter that increases the cranking speed [6].

Second, the time to restart needs to be as short as possible so that the engine can satisfy any torque demand requested by the driver. Initially, the speed of response for the restart event is limited by the characteristics of the starter torque delivery [13]. The restart time can also be reduced if the controller knows the crankshaft position prior to a restart event; this enables the engine to fire on the first compression event [18].

Third, it is important to optimize the energy consumption during the restart transient so that the extra fuel needed to restart the engine is minimized. If the restart FC is not minimized, then the tradeoff time for using SS increases and SS operation does not effectively increase the FE. Conceptually, tradeoff time is the amount of time that the engine must be shutdown to save at least as much fuel as is consumed by the engine restart event. Tradeoff time is defined formally by equation (4.10) in Section 4.4.

This work addressed the third consideration covered above. For the remainder of this document, the optimization of the energy consumption during the start transient becomes the topic of discussion. In order to determine an ideal improvement of FE for the Chrysler van utilizing start/stop, it was desired to compare the FC for the baseline case and the case where start/stop was enabled. This was carried out using a modeling tool known at CAR as the Vehicle Energy Simulator (VES) over the first 1370 seconds of the EPA Federal Test Procedure (FTP).

1.4 Vehicle Energy Simulator

The Vehicle Energy Simulator (VES) is a forward-looking energy model that is capable of providing comprehensive data about how a vehicle's energy is utilized during driving. Figure 6 provides an overview of the VES structure that was implemented in the MATLAB/Simulink environment. The VES vehicle plant contains various subsystems. To gain an in depth understanding of the subsystems refer to: the thermal management model covered in **Error! Reference source not found.** and [20], the powertrain and mechanical model in [21], and the electrical model in [22]. The VES was calibrated and validated based on experimental data from the engine and powertrain system of the 2011 Chrysler Town and Country minivan to ultimately provide information about FC, FE, and emissions when operated over a driving cycle. A drive cycle is a standard velocity profile that is followed by a vehicle when testing it on a chassis dynamometer. Section 2.1.2 explains the chassis dynamometer. Many standard drive cycles exist; however, the Chrysler Project focuses on showing FE improvement on the EPA FTP city and highway drive cycle.

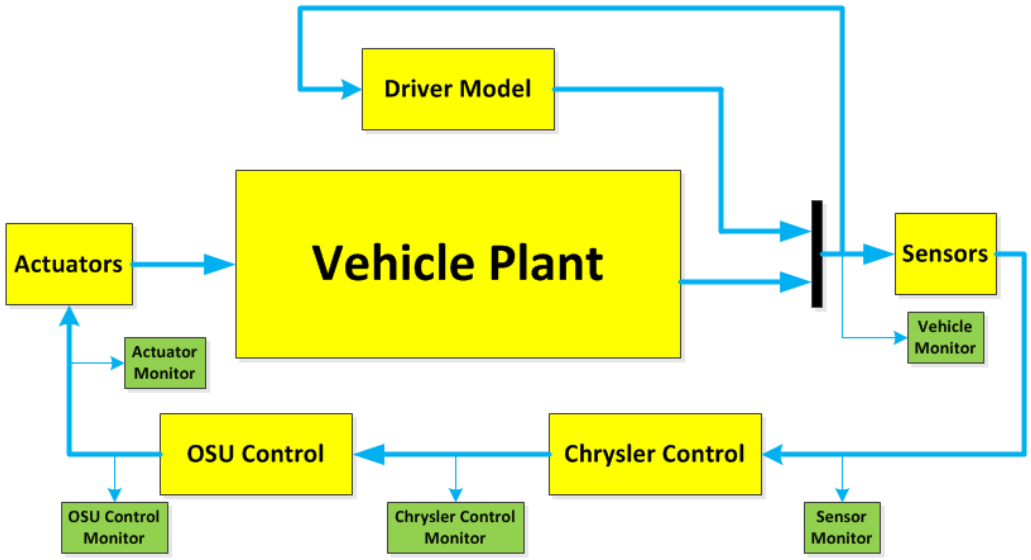

Figure 6: Top-Level VES Simulink Structure [21]

1.5 Motivation for Start/Stop using VES over FTP Cycle

It was desirable to motivate the investigation of start/stop as a significant means of increasing the FE of the Chrysler van using the VES. Once the VES had been calibrated and validated for the minivan based on experimental data, it accurately predicted vehicle FE. The VES was run over the first 1370 seconds of the EPA FTP cycle shown in Figure 7 to establish a baseline condition for FC. The first 1370 seconds of the FTP includes the cold start phase and transient phase shown in the figure. The EPA defines this as the Urban Dynamometer Driving Schedule (UDDS) and was of most interest for SS because it contains more idling events than the highway cycle. In order to realize the benefits of SS, the baseline fuel flow trace for the UDDS was post processed so that the fuel flow rate was zero during periods of zero velocity. This happens 18 times in total for the UDDS. The resulting fuel flow traces for the baseline case and the case with SS enabled is shown in Figure 8. Ignore the red line, “DFSO [21] Enabled” in the figure.

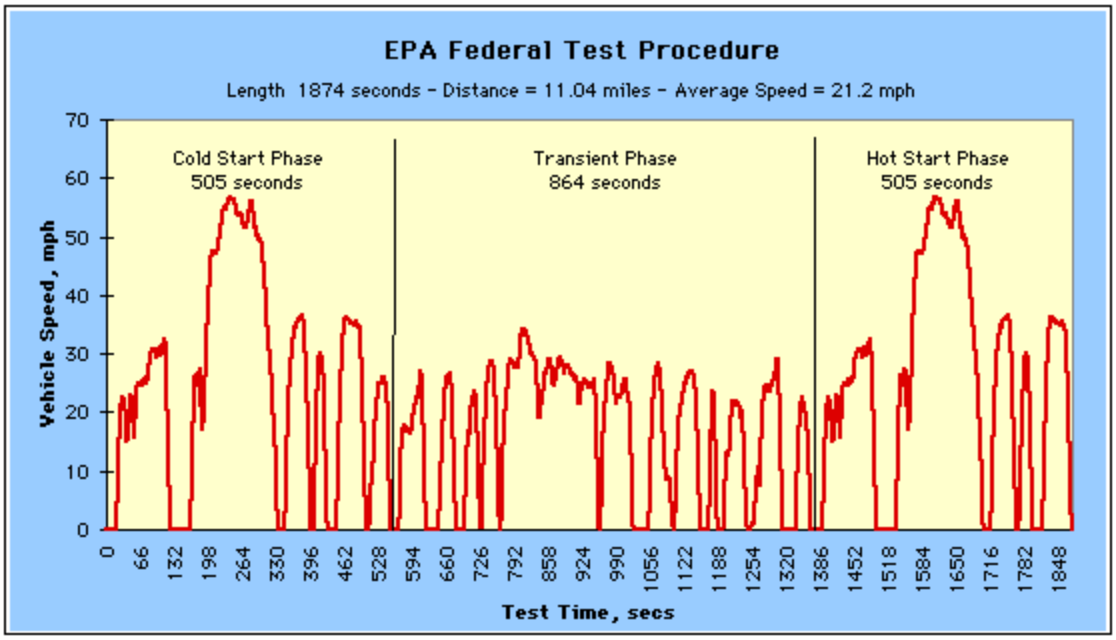

Figure 7: Federal Test Procedure Used by the EPA for determining emissions and FE [23]

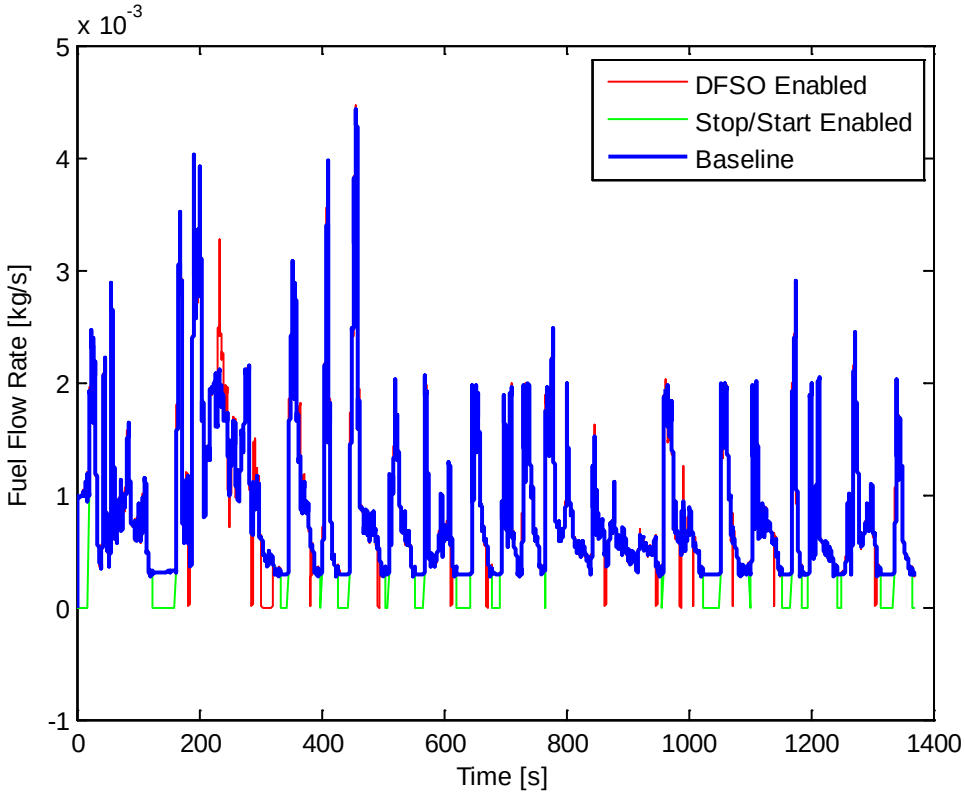

Figure 8: Fuel Flow Rates of Fuel Saving Techniques over UDDS cycle [21]

By integrating the fuel flow traces over time, the vehicle FC for baseline and with SS was accumulated for the length of the cycle. The resulting cumulative fuel flow is shown in Figure 9.

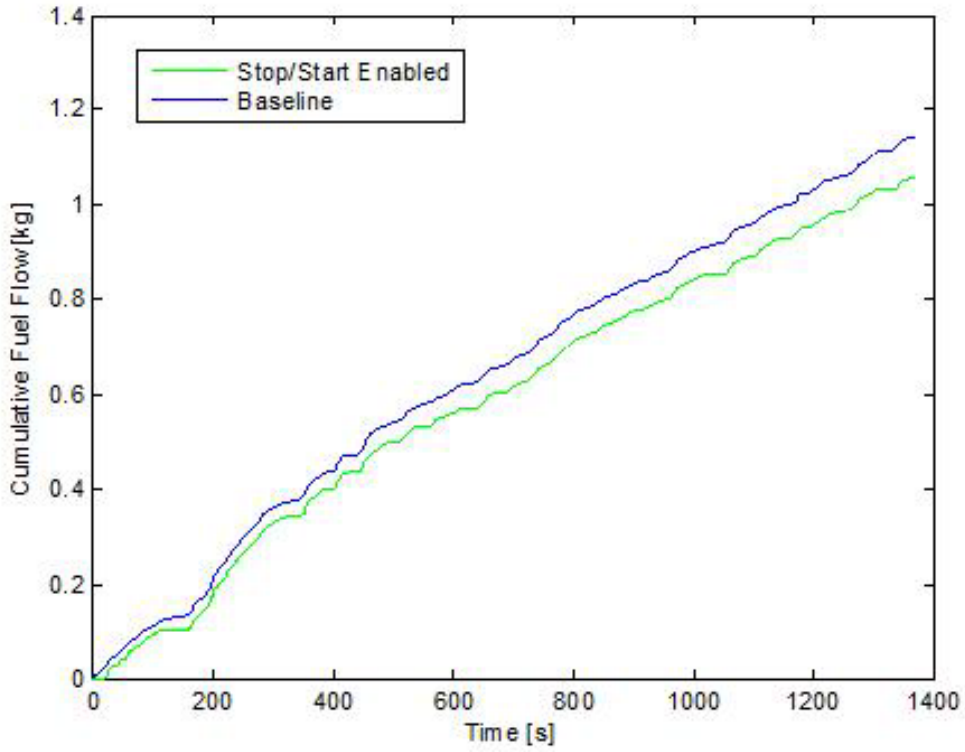

Figure 9: Cumulative Fuel Consumption over First 1370s of FTP Cycle (adapted from [21])

The figure shows a significant decrease in FC using SS by comparing the final values of cumulative fuel flow for the two cases. Using the final values, it was possible to quantify the decrease in cumulative fuel use for SS $M_{fuel_{savedSS}}$ and is shown in equation (1.1).

$$M_{fuel_{savedSS}}[kg] = FC_{base} - FC_{SS} \tag{1.1}$$

In equation (1.1), fuel consumption FC is the maximum or final value of cumulative fuel flow shown graphically in Figure 9 and defined by equation (1.2) where $\dot{m}_{fuel}$ was the fuel flow rate.

$$FC\ [kg] = \max\left(\int \dot{m}_{fuel}\, dt\right) \tag{1.2}$$

The percent decrease in FC $\%\Delta FC$ was calculated using equation (1.3).

$$\%\Delta FC = \frac{FC_{base} - FC_{SS}}{FC_{base}} \times 100 = \frac{M_{fuel_{savedSS}}}{FC_{base}} \times 100 \quad (1.3)$$

Fuel Economy FE in miles per gallon, was found using equation (1.4) where v was the instantaneous vehicle velocity during the cycle and ρ_{fuel} was the fuel density.

$$FE\ [mpg] = \frac{\int v\ dt}{\left(1/\rho_{fuel}\right) \cdot FC} \quad (1.4)$$

The percent FE improvement $\%\Delta FE$ was calculated in equation (1.5).

$$\%\Delta FE = \frac{FE_{base} - FE_{SS}}{FE_{base}} \times 100 \quad (1.5)$$

Table 3 shows the fuel saving benefits when SS was enabled in the VES run over the UDDS. In the table: column 1 is the decrease in cumulative fuel use for SS $M_{fuel_{savedSS}}$, column 2 is the percent decrease in FC $\%\Delta FC$, and column 3 is the percent FE improvement $\%\Delta FE$ as found using equation (1.1), (1.3), and (1.5) respectively.

This analysis showed that a potential increase in FE of up to 8% was possible by implementing a SS system on the vehicle. This FE improvement was the theoretical maximum improvement possible over the UDDS because it did not account for the energy consumed to restart the vehicle after each of the 18 stop events. This work quantified and optimized the vehicle restart energy.

Table 3: Fuel Consumption Benefits of Stop/Start Compared to Baseline (adapted from [21])

Decrease in Cumulative Fuel Use [kg]	Decrease in Fuel Consumption [%]	Increase in Fuel Economy [%]
0.0842	7.3680	7.9540

1.6 Goals, Objectives, and Fundamental Questions

The goal of this work was to investigate the feasibility of using start/stop technology as a means to increase the vehicle fuel economy for the EPA Urban Drive Cycle. To do this, it was desired to analyze and optimize the energy consumption during engine startup. This overarching goal led to the objectives outlined in the following statement.

The objectives for this work were: 1) collect experimental data from the Chrysler minivan that were useful for analyzing the internal combustion engine startup dynamics, 2) create an analysis tool that utilized the experimental data to describe the engine startup dynamics, 3) use the modeling tool to quantify the energy consumption of the baseline engine start transient, and 4) analyze various starter/battery systems to find a combination that yields the optimal startup sequence in terms of quantitative energy consumption.

The fundamental questions on start/stop energy consumption during the engine start transient were: 1) what was the impact on battery energy? and 2) what was the impact on fuel consumed to restart the engine?

Chapter 2: Description of Experiments

2.1 Experimental Setup

Chrysler LLC has provided The Ohio State University's Center for Automotive Research (CAR) with a 2011 Chrysler Town and Country minivan and a separate 3.6L V6 Pentastar Engine for research use. The vehicle and engine were instrumented with various data acquisition (DAQ) tools including sensors and software that allowed experimental data to be collected. The engine was tested on a 300 HP AC dynamometer (dyno) set up in CAR's High Bay area. The vehicle was tested using the chassis dyno located in CAR's anechoic chamber. A detailed description of each setup is described below.

2.1.1 Engine

The 3.6L V6 engine used for experimental testing is a production engine and has been used in the 2011 through 2013 Chrysler Town and Country minivan. The engine is a spark-ignition port-fuel injection engine with a naturally aspirated intake manifold. The engine valvetrain uses dual overhead cams with two intake and two exhaust valves per cylinder and features variable valve timing. Some of the basic engine specifications are shown in Table 4.

Table 4: Chrysler 3.6L V6 Pentastar Engine Specifications [22]

Displacement [L]	3.6
No. of Cylinders	6
Bore [mm]	96
Stroke [mm]	83
Compression Ratio	10.2
Max Torque [Nm @ rpm]	353 @ 4400
Max Power [kW @ rpm]	216 @ 6350

The engine was outfitted with a metered fuel tank and a coolant circuit with cooling tower to operate on the dynamometer. A photo of the setup in CAR's dyno test cell is shown below in Figure 10.

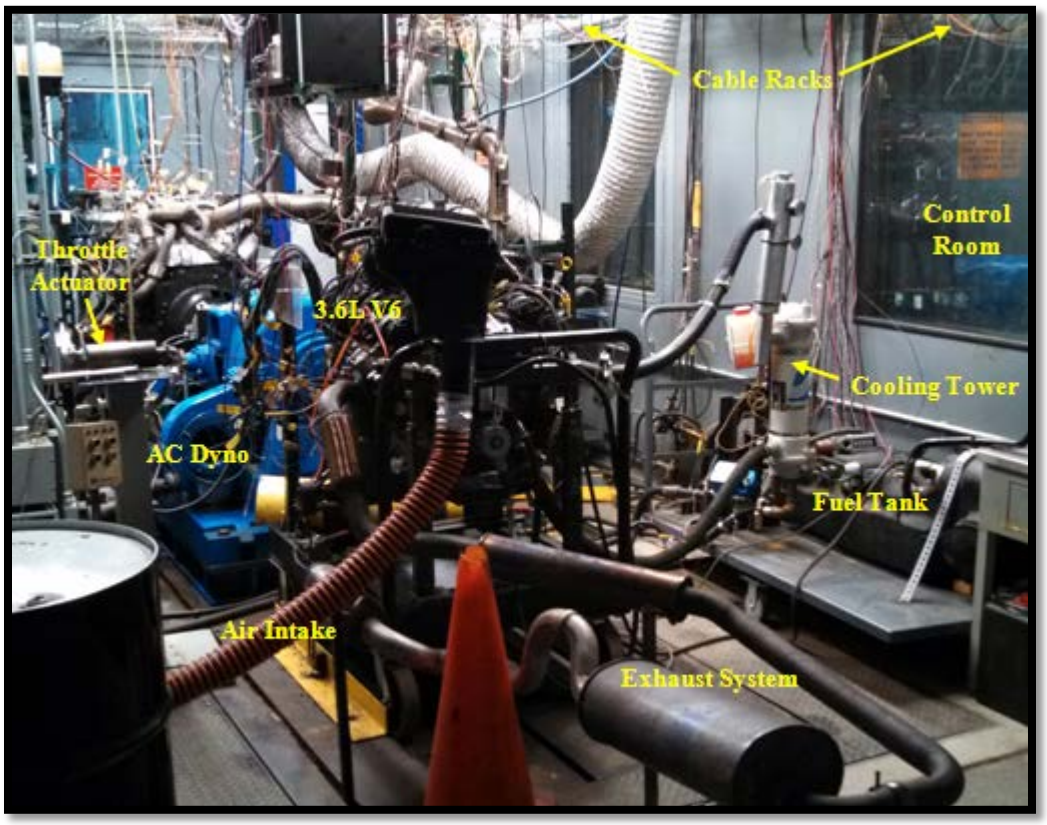

Figure 10: Engine Dynamometer Test Cell [22]

This engine was instrumented with many sensors including thermocouples, pressure taps, and flow meters to monitor and control the flow and combustion. The sensor signals were acquired by a 128 channel DAQ system and a Horiba Mexa 7500 emission analyzer [22]. A diagram of the DAQ system can be seen in Figure 11. The purpose of the dyno test cell was to obtain a characterization of air flow, combustion and torque output at various engine steady-state operating conditions using a controlled environment where variables can be monitored and maintained. This setup allowed for accurate experimental data to be obtained for idle operating

conditions and was used to check the “Big Grid” data provided by Chrysler, which is discussed later in Section 2.2.1.

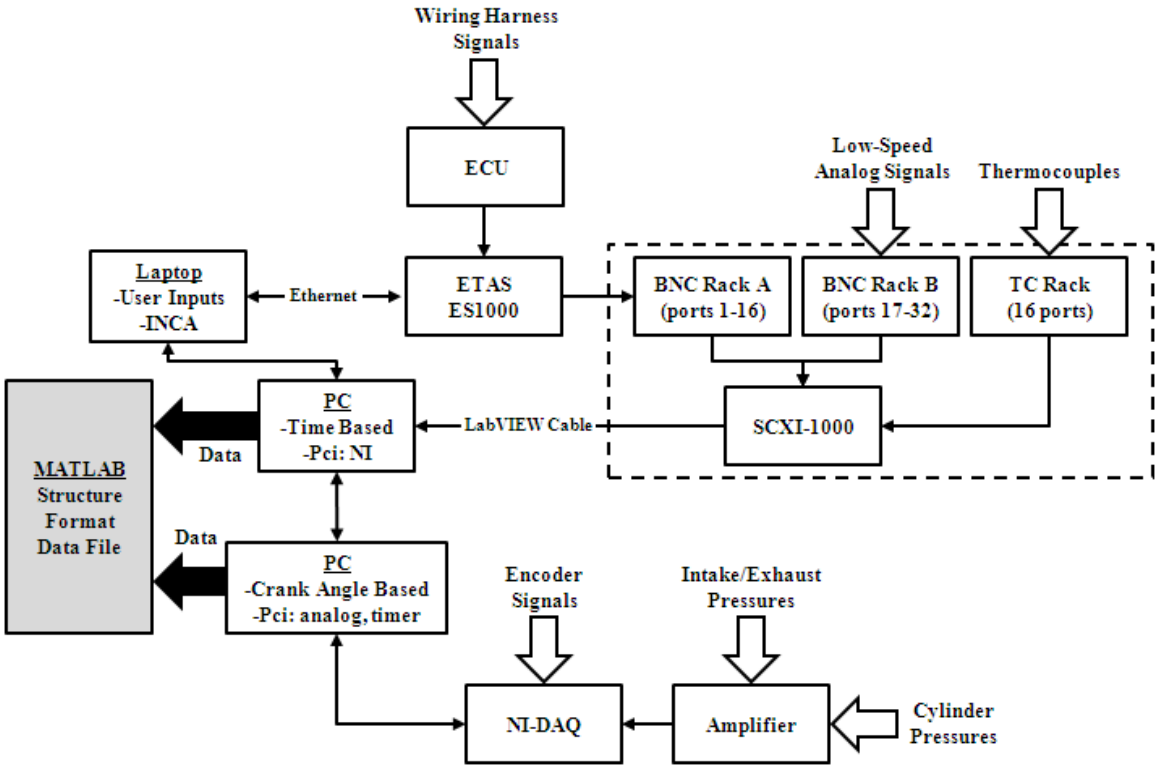

Figure 11: Engine Dynamometer Data Acquisition System [22]

2.1.2 Vehicle

In addition to the engine, Chrysler also provided CAR with a test vehicle that was used to collect experimental data that could not be determined with the engine dyno setup described above. See Table 5 for an overview of various test vehicle specifications. The vehicle test setup was used to acquire data that could not be obtained with the engine dyno test setup. The setup was utilized for collecting data related to the electrical system, transmission, and auxiliary loads of the minivan. The vehicle test setup was integral for this research as it was the sole means of obtaining data related to the vehicle startup dynamics for the engine and electrical systems.

Table 5: Test Vehicle Specifications [22]

Make, Model and Year	2011 Chrysler Town & Country
Mass	2154 kg
Frontal Area	2.42 m^2
Aerodynamic Drag Coefficient (C_d)	0.33
Gear Ratios (1-6)	4.127 - 2.842 - 2.284 - 1.452 - 1.000 - 0.690
Final Drive Ratio	3.16
Tire Radius	0.3514 m
Engine	3.6L V6 SI (see Table 4)
Transmission	62TE 6-Speed Automatic Transmission
Battery	Lead-Acid AGM, 20 hour capacity 75 A-h, nominal 12 V, 100 A max charging current

The vehicle was outfitted with an ETAS DAQ system that recorded information from the engine electronic control unit (ECU), thermocouples for temperatures throughout the engine and auxiliary systems like the AC system, and for current shunts installed on the electrical system. The crankshaft encoder used to acquire the speed of the engine was obtained by bypassing the ECU and collected directly by the DAQ system at very high sampling rate.

The experimental data were recorded on a computer that interfaced with the ETAS DAQ using software called INCA. See Figure 12 for a schematic and picture of the vehicle DAQ system.

The electrical system was instrumented with various current shunts. The two larger current shunts, shown in Figure 13, were installed to determine the battery current and the alternator output current. There were also shunts installed to measure the field current of the alternator and the current consumed to run the ETAS DAQ, which was powered off of the vehicle battery during testing.

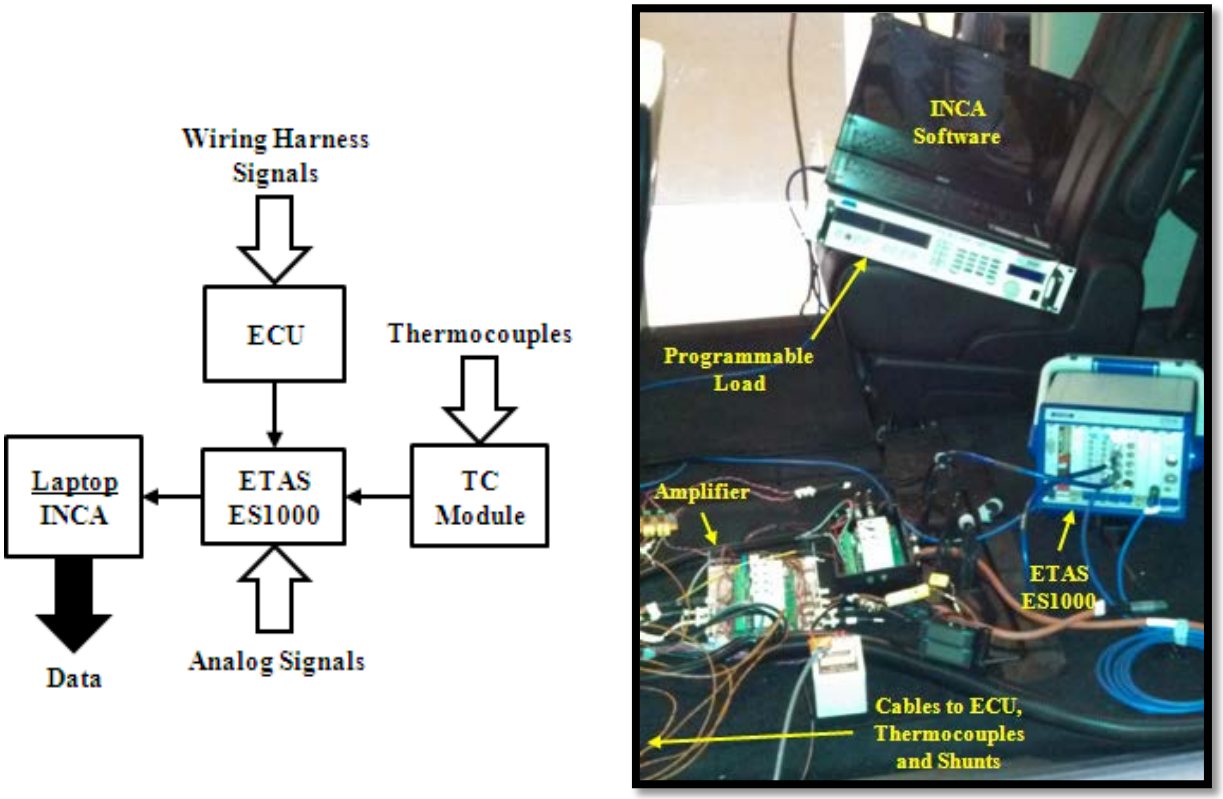

Figure 12: Vehicle DAQ Schematic (left) and Accompanying Components (right) [22]

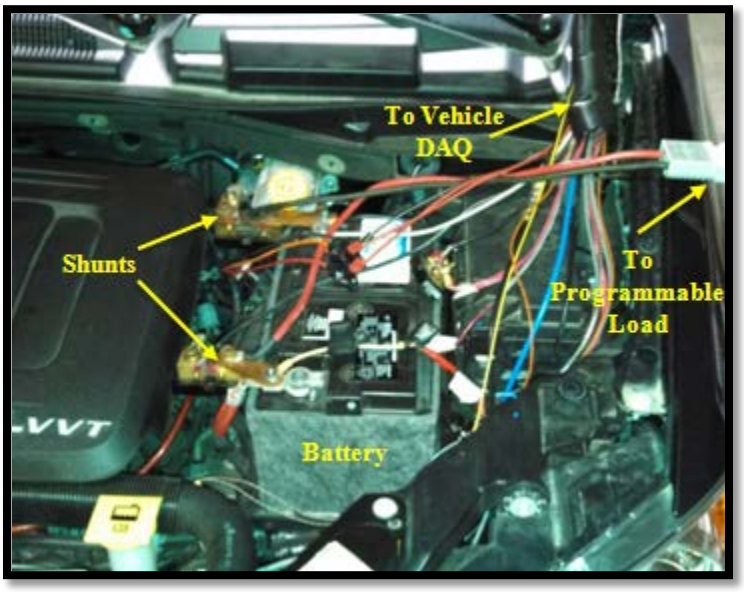

Figure 13: Current Shunts Installed on Electrical System [22]

The standard procedure that the EPA uses to determine a vehicle's published FE and emissions is to run the vehicle over the FTP drive cycle (see Figure 7) on a chassis dynamometer. Because the VES (presented in Section 1.5) was validated over the first two phases of the FTP cycle, it was necessary to test the vehicle on CAR's chassis dyno in order to obtain the experimental data used for the calibration and validation of the VES. Since the VES is used to quantify FE improvement and provide motivation for investigating SS technology, a short description of the dyno is presented and a picture of the chassis dyno is shown below in Figure 14. However, the chassis dyno was not used for collecting the experimental results presented in Sections 2.3.2 and 2.3.3.

Figure 14: Test Vehicle on Chassis Dyno [22]

CAR's chassis dyno is located in an anechoic chamber next to the vehicle High Bay. The dyno uses two 24" diameter rolls to test small and mid-size vehicles [22]. A driver's aid monitor is provided to assist a driver in following the velocity trace while testing the vehicle over a drive

cycle [22]. The monitor displays a LabVIEW interface that shows the upcoming velocity of the cycle and a tolerance band to help the driver minimize the error during testing.

2.2 Experimental Methods

The experimental data obtained from the engine dynamometer was acquired by the DAQ system as a low speed and a high data set and then converted with INCA software to a file format useable in MATLAB. The low speed data set was time-based and included data from the ECU and thermocouples. The high speed data were cycle-based and was collected as a function of crank angle degrees (CAD). These data included intake and exhaust pressures as well as in-cylinder pressures and encoder data. The cycle-based data were important for this work because the model developed in Chapter 4 was crank angle resolved.

The vehicle experimental signals were post processed with MATLAB after being obtained with the vehicle DAQ. The data set was time-based with varying sampling rates for each signal. The crank encoder signal had the highest sampling rate in order to capture the crankshaft startup dynamics completely. The time scales from the ECU and current shunts were scaled to match the encoder time stamp. The signals were collected by the INCA software as .dat files and post-processed as .mat files using a MATLAB graphical user interface (GUI).

2.2.1 Engine

One standard test that is typically conducted on engine dynamometers is to characterize the engine performance over its entire range of operation. The operating region of the engine is characterized by its limits for speed and torque. This test procedure is used at Chrysler and the resulting data from this test for the 3.6L V6 was given to CAR along with the vehicle and the

engine. The results from this test are collected into a spreadsheet that Chrysler terms “Big Grid” data, and it contains many engine operating parameters including temperatures, pressures, flow rates, torques and efficiencies defined for steady-state torque and speed points. The Big Grid data from Chrysler was checked using the engine dyno setup described above in Section 2.1.1. The test procedure at CAR was to match and hold the engine speed at a specific Big Grid point by setting the dyno controller to the desired engine speed. The engine torque output was set to the target value by changing the electronic throttle position. This test procedure was used to acquire steady-state engine data that were compared against the experimental data provided by Chrysler. Additional tests were then conducted to characterize the engine behavior at operating points not included in the Big Grid, specifically at low speed conditions. To this extent, additional data were collected for three engine speeds near idle conditions at 625, 750, and 900 rpm with throttle position set as close to 0% opening as possible. The results of the low speed tests are presented in Section 2.3.1. The data were used to calibrate the portion of the model covered in Section 3.3.1.

2.2.2 Vehicle

The vehicle test setup was instrumental for the research described in this document. Experimental results from the engine dyno alone do nothing to describe the startup dynamics of the engine, which are the main interest for investigating start/stop operation. The only way to obtain experimental results for the vehicle startup dynamics was to run tests on the vehicle in which the start transient of the engine was captured. An initial test showed that the crankshaft signal acquired by the ECU did not capture the area of interest for the engine startup dynamics. In order to obtain the portion of the startup not sensed by the vehicle ECU, the crank encoder

signal was acquired by bypassing the ECU and collecting raw pulse data from the encoder at a very high sampling rate. The encoder signal was later post-processed with MATLAB to obtain the speed trace of the engine during the tests.

Start/stop technology is primarily utilized when the vehicle operating conditions are stable, which is after the vehicle has had time to warm up and adjust to ambient conditions. Therefore, the experimental tests were all conducted with the vehicle in the fully warmed conditions. This was achieved by allowing the van to run for a 30 minute time frame prior to any data being collected. After reaching stable, fully warmed conditions the vehicle was shut down for a few minutes before the first startup test was performed.

The goal of the test procedure was to capture the start transient of the vehicle during the fully warmed up state. First, the vehicle electronics and the DAQ system were electrified and data collection began. Then, a key start was initiated and the resulting start transient was recorded by the DAQ. The vehicle was left running long enough to allow the alternator to recharge the battery. The engine idle speed was higher during the time that the battery was recharging. Once the engine reached its lowest idle speed the van was shut down. This test was repeated three times in succession over a 170 second time interval. The first test was 35 seconds long and tests two and three were around 50 seconds in length each. Test one was not long enough for the engine to reach its lowest idle speed so the time interval for the remaining tests was increased.

An overview of the results from the complete testing conducted on the vehicle is shown in Figure 15. The results show that test one was not long enough for the engine to reach the lowest idle speed. The fuel flow rate between each test was zero. The data showed a constant fuel flow rate for the time between the end of test one and the start of test two. This was a false reading and

was ignored. The results for the three warm startup tests are discussed in detail in Sections 2.3.2 and 2.3.3. The results of a preliminary test similar to the ones presented in Figure 15 were used for calibrating the portions of the model presented in Section 3.3.2.

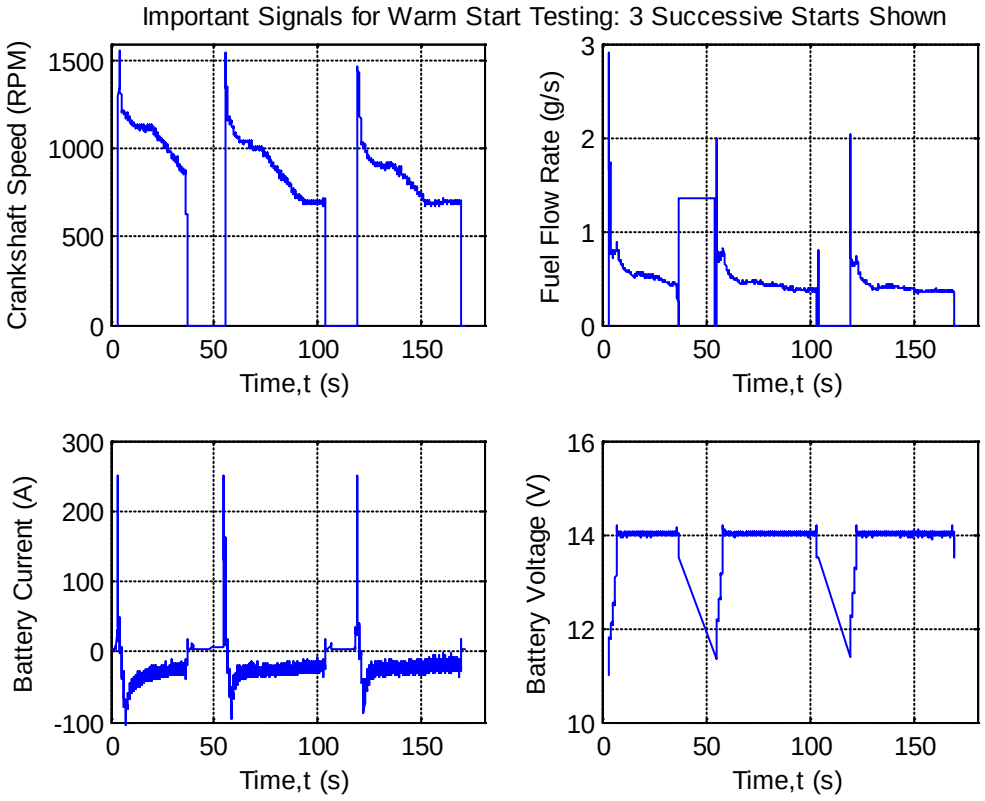

Figure 15: Important Variables for Warm Start Test Procedure: 3 Startups in Succession

2.3 Experimental Results

The experimental tests for the Chrysler Project were mainly carried out by OSU graduate students Kyle Merical, Jeremy Couch, and Saba Gurusubramanian. The engine dyno data presented below in Section 2.3.1 was provided to the author by Kyle Merical using the test procedure described above in Section 2.1.1. The vehicle data presented in the following Sections

2.3.2 and 2.3.3 was obtained by following the testing procedure detailed above in Section 2.2.2 and was carried out by Saba Gurusubramanian and the author.

2.3.1 Fired Engine Test Results

Using the engine dyno test setup described above, results for the in-cylinder pressure of cylinders one, two, and three of the 3.6L V6 engine were obtained. Data were collected for engine operating speeds near idle at 625, 750, and 900 rpms. The throttle was set as close to 0% opening as possible in order to emulate the throttle position during a warm startup on the vehicle. The engine was fired for all tests, which means that combustion occurred in the engine cylinders during testing. More than 200 cycles of data were collected at each operating point and each of the three cylinder pressures were synchronous averaged over this cycle interval. The results for the 625 rpm case are shown below. Figure 16 shows the pressure trace for each cylinder as a function of cylinder volume. This graph shows that for a fired cylinder there was a positive work integral as expected. A positive work integral for each cylinder shows that there was energy being released each time a cylinder fired. Heat generation from combustion caused the pressure inside the cylinders to rise even after the cylinders had reached top dead center (TDC), which is the normal peak of compression when the cylinders are not fired. This is illustrated in Figure 17 where the in-cylinder pressures are shown as a function of CAD over a single cycle. TDC occurs at 360 degrees in the figure and peak pressure was reached around 380 degrees. The average of the three in-cylinder pressures is used to approximate the net heat release per cycle in a typical engine cylinder and can be thought of as the balance between the energy released from the combustion process and the heat losses to the cylinder walls and piston. Section 3.3.1 covers

how the net heat release rate was calculated from the average, in-cylinder pressure per cycle and also how it was used in the model.

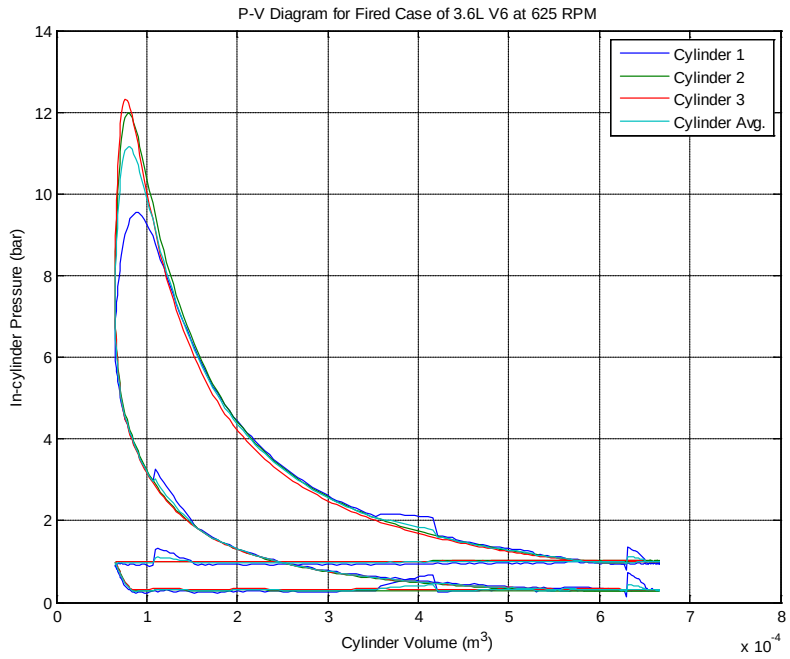

Figure 16: P-V Diagram of In-Cylinder Pressure for Fired Engine

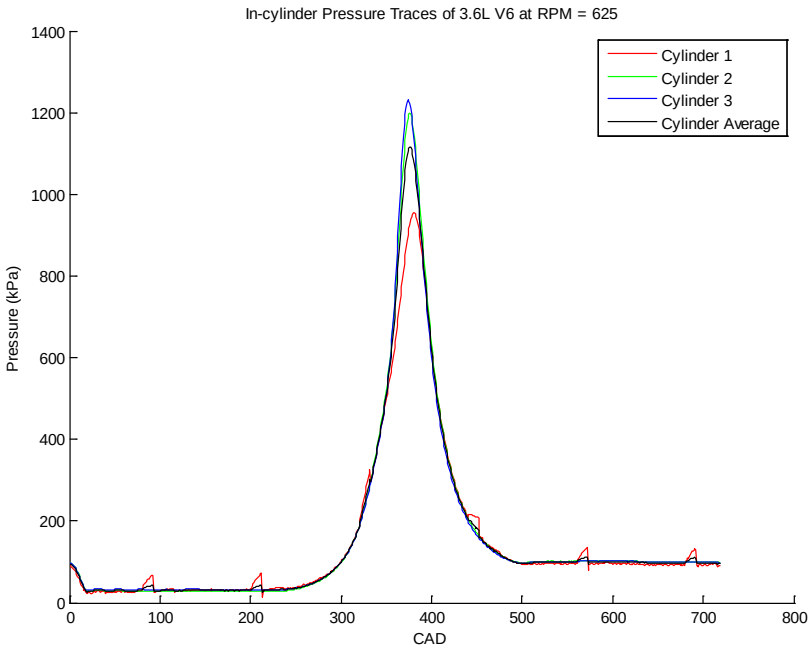

Figure 17: In-Cylinder Pressure vs. CAD for Fired Engine

2.3.2 Warm Start Test Results

The vehicle test setup and DAQ system were used to collect data during three start transients that were recorded in succession as shown in Figure 15 of Section 2.2.2. Table 6 shows the variables that were acquired during the test as well as the units of each variable and how each of the variables was collected. Other variables were obtained in addition to those listed in the table, which included spark timing, alternator field current, and alternator field voltage.

Table 6: Signals Acquired during Warm Start Testing

Variable Acquired	Units	Obtained From
Engine Crankshaft Speed	RPM	ECU/Encoder Raw Data
Battery Voltage	Volts	ECU
Battery Current	Amps	DAQ Current Shunt
Alternator Output Current	Amps	DAQ Current Shunt
Intake Manifold Absolute Pressure	kPa	ECU
Fuel Flow Rate	g/s	ECU

These data were separated into three individual tests and are presented in this section. Figure 18 shows the three tests separated and plotted such that the start of each test aligns with the others at time zero. Time zero was determined using the first positive data point for speed sensed by the crank encoder since it had the highest resolution during testing. The figure shows various signals over the entire length of each test. Note that the variables reached constant values around 10 seconds, except for the engine crankshaft speed which remained at a high idle speed until about 35 seconds.

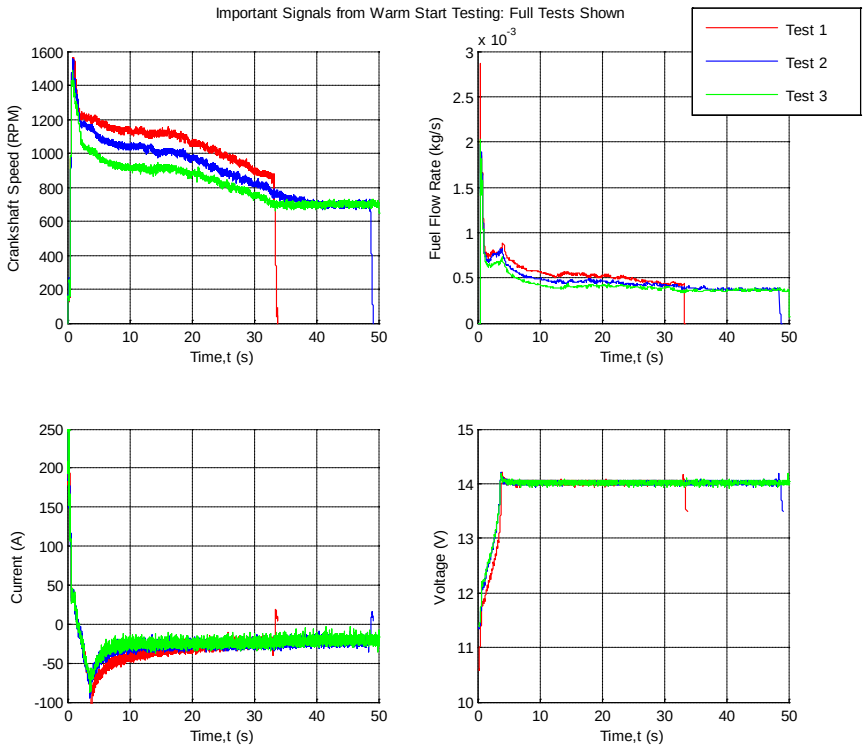

Figure 18: Important Variable of Three Warm Start Tests: Full Length Tests Shown

The high idle speed of the engine was due to the idle control strategy to recharge the battery immediately following the engine startup. The engine speed did not drop off to the normal idle speed, which was 700 rpm, until the battery state of charge (BSOC) reached the threshold set point. Once the battery reached the threshold BSOC the idle control commanded a linear decrease in the speed from the higher, recharging speed to 700 rpm. In each test the start of the linear decrease in idle speed occurred around 16 seconds. The increase in the BSOC was observed as a hyperbolic curve in the battery current. The battery voltage was quickly replenished and held at a constant 14 volts by the electrical system controller after the initial voltage drop due to the energy consumed by the engine starter. This will be explained in detail later, the point here is to note that the increase in the battery current was very small after 10

seconds. For the purpose of investigating data significant to start/stop operation, it was appropriate to ignore the change in the idle speed and 10 seconds was used as the cutoff time for the area of interest in the following results.

Figure 19 shows the engine speed trace of the vehicle during the startup for all three tests. The figure also shows a detail of the engine speed trace during the very beginning of each startup for clarity. This portion of the start transient is called the cranking phase and is the portion of the startup when the only torque applied to the engine crankshaft is produced by the engine starter; this is addressed in detail in Section 2.3.3.

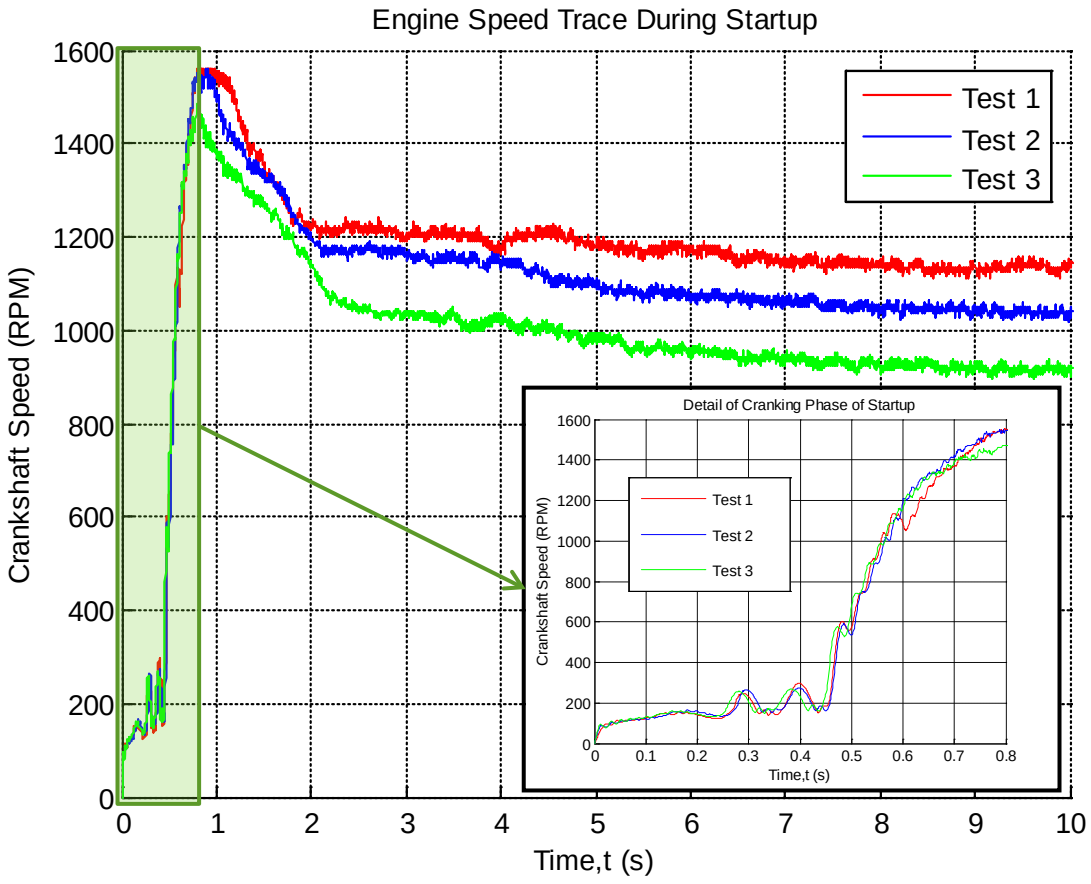

Figure 19: Engine Speed Trace during First 10 Seconds of Warm Start Testing

Figure 19 shows that for each successive start of the vehicle, the engine crankshaft speed peak and high idle speed decreased. For test one, the vehicle had been electrified for some time and the vehicle auxiliary loads and the DAQ system had been draining the battery prior to the start of test one; more so than in tests two and three, which were preceded by a reduced engine shutdown time and hence a higher BSOC. Once the vehicle was started in test one, the vehicle idle control commanded a high idle speed of around 1200 rpm in order to more aggressively recharge the battery than in the other tests. In tests two and three the high idle speed was around 1100 and 1000 rpm, respectively. This successive decrease in the high idle speed commanded by the idle controller was due to the BSOC being higher for test three than test two, and the BSOC being higher for test two compared to test one.

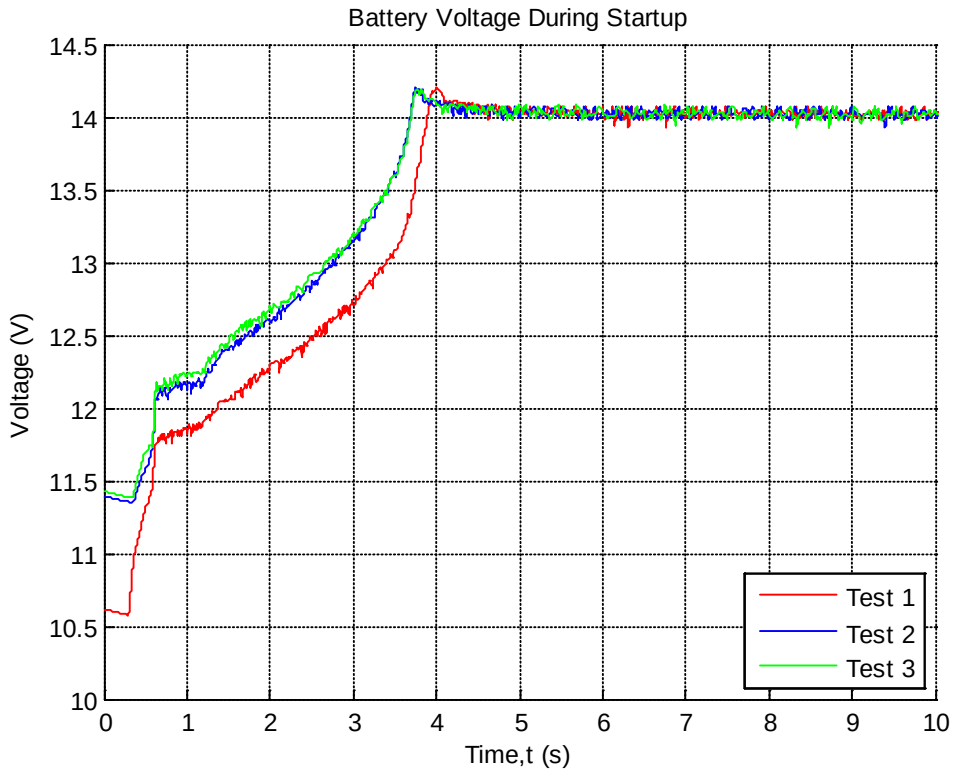

Figure 20: Battery Voltage during First 10 Seconds of Warm Start Testing

These same observations are shown by looking at the battery voltage in Figure 20. The battery voltage showed that test one had a lower initial voltage of around 10.5 volts compared to 11.5 volts for tests two and three. Once again, the extended period of vehicle and DAQ electrification before the start of test one accounts for the difference in initial voltage of test one compared to tests two and three.

At the very beginning of the start transient the only torque produced to spin the crankshaft was produced by the DC electric starter. The starter consumed energy from the battery to turn, or crank, the engine. The energy consumed was observed in the battery voltage and current. The initial voltage drop was due to this energy consumption. The battery voltage remained stable after the starter stopped cranking from 0.6 to 1.14 seconds. After this point, the battery voltage was quickly replenished. The nominal 14 volts was reached at around 4 seconds into each test. The energy used to replenish the battery was harvested from the engine by the alternator and was created as a direct result of the alternator field current and the high idle speed used during the startup. This is verified by observing that the engine idle speed began to drop after 4 seconds in Figure 19.

Figure 21 shows the battery current during the startup tests. Initially 250 amps were drawn from the battery to supply the starter with the power to crank the engine. The current drawn dropped to 30 amps after 0.6 seconds; this was the current necessary to power all of the vehicle ancillary loads. At 1.14 seconds the battery current decreased linearly until reaching a lower limit of around negative 100 amps after 4 seconds. The turn in the battery current at 4 seconds was due to the battery reaching constant, nominal voltage. At this point the alternator duty cycle changed

to slowly restore the BSOC while constant battery voltage was maintained; this was observed as a hyperbolic curve in the battery current after 4 seconds.

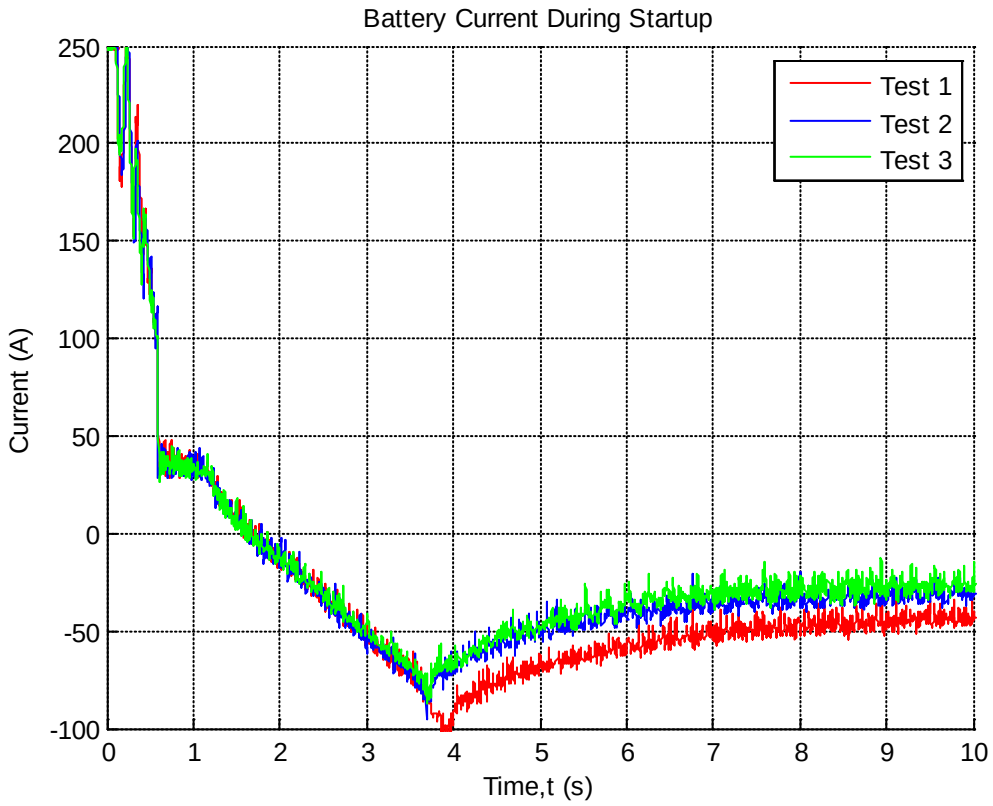

Figure 21: Battery Current during First 10 Seconds of Warm Start Testing

Figure 22 shows the alternator output current during the engine startup. It was observed that the alternator began recharging the battery at 1.14 seconds and that the turn in the alternator output current was due to the alternator controller changing the duty cycle after the battery voltage had been restored to constant, nominal 14 volts.

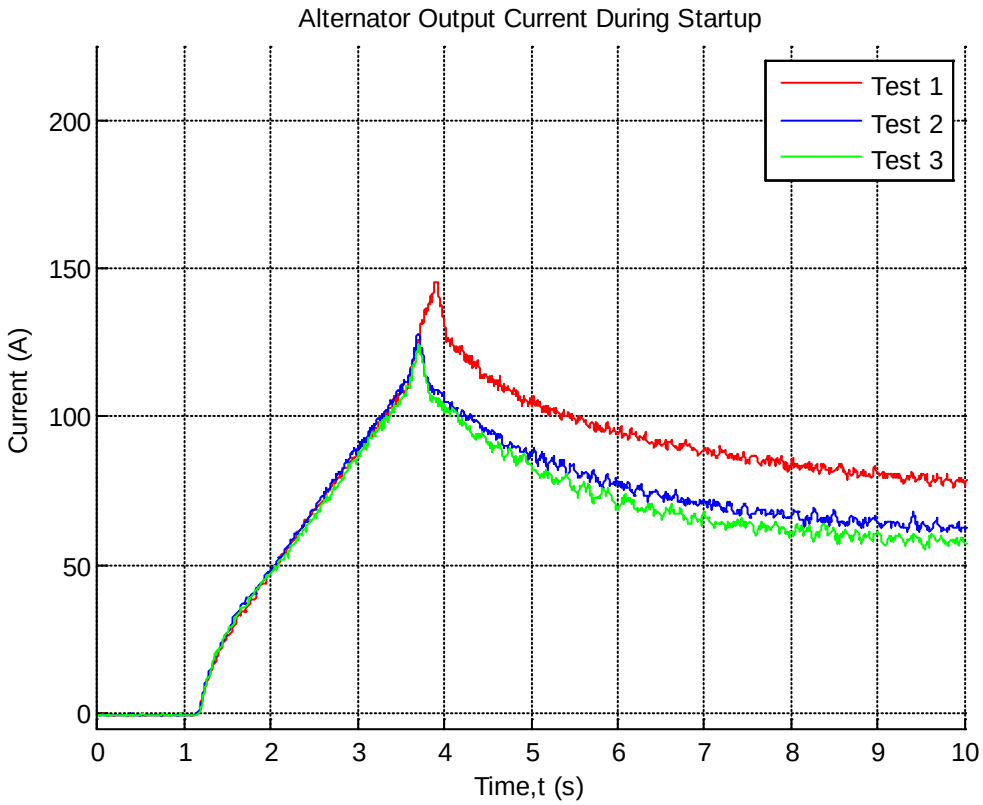

Figure 22: Alternator Output Current during First 10 Seconds of Warm Start Testing

The sum of the battery current and alternator output current allowed for the current drawn by the starter and the auxiliary loads to be isolated. As noted above, the vehicle auxiliary loads drew 30 amps continuous. The sum of the currents was scaled by this 30 amp auxiliary load current. This is referred to as the inferred starter current and is shown in Figure 23. The power consumed by the starter during the transient was found by multiplying the inferred starter current by the instantaneous battery voltage. The result is shown in Figure 24. Because the battery voltage during the first 0.6 seconds of each test was constant, the electrical power consumed by the starter was the starter current scaled by the battery voltage. This resulted in a peak power consumption of approximately 2.5 kW when the starter was cranking.

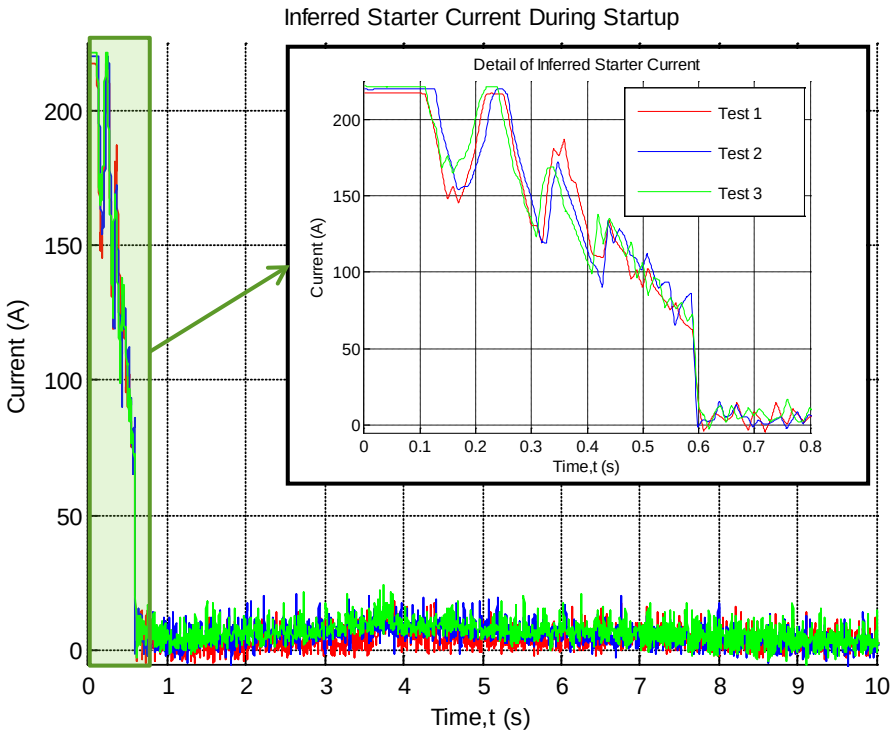

Figure 23: Inferred Starter Current during First 10 Seconds of Warm Start Testing

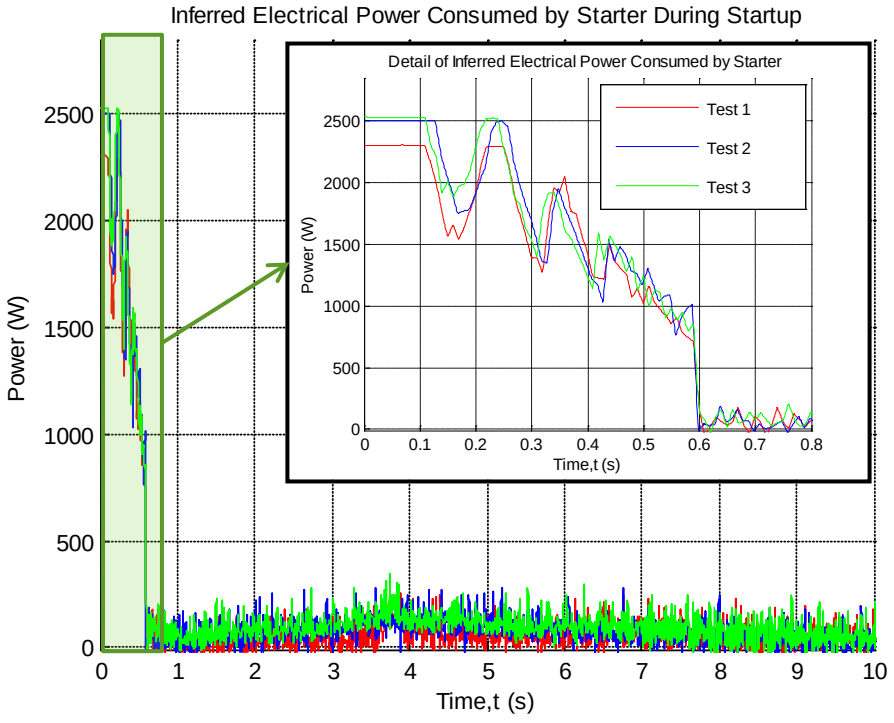

Figure 24: Inferred Starter Power during First 10 Seconds of Warm Start Testing

Figure 25 shows the torque applied to the engine crankshaft by the starter. Electrical power was converted to mechanical power by assuming a constant motor efficiency of 90% and was provided to the author by Chrysler. Power losses due to the gear reduction were ignored, so the torque applied to the engine by the starter during cranking was found by dividing the starter mechanical power by the mean angular velocity of the crankshaft during the cranking phase of the startup. For this calculation the gear ratio between the starter pinion gear and the engine flywheel was ignored because only the torque at the crankshaft was of interest.

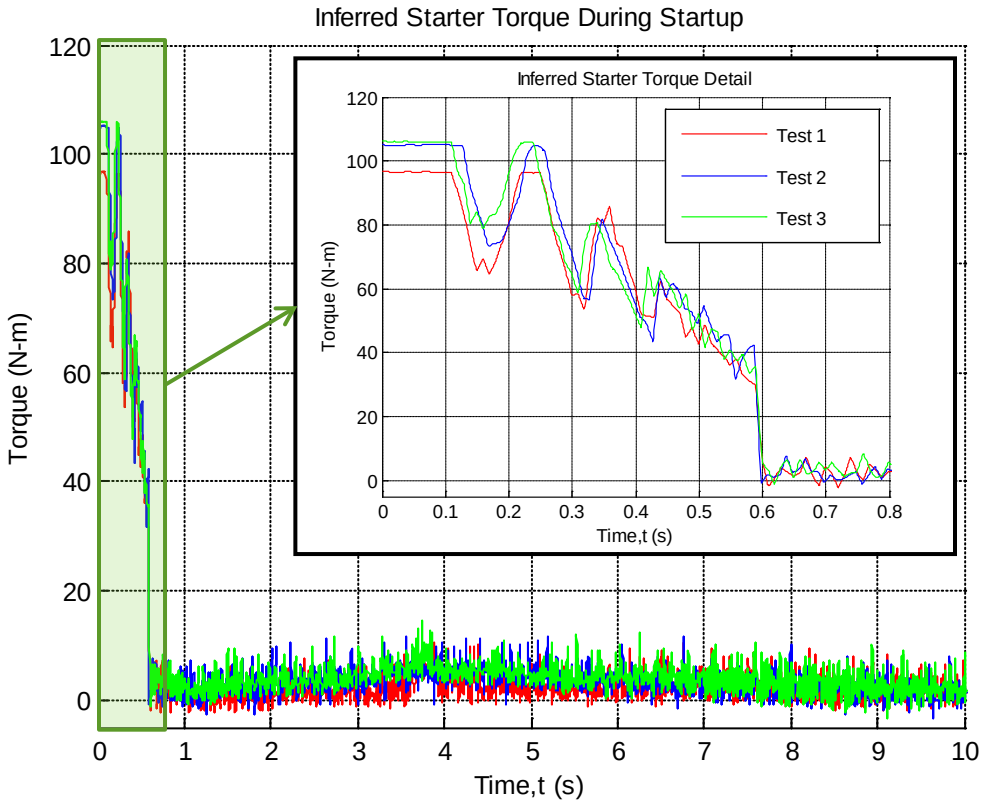

Figure 25: Inferred Starter Torque at Crankshaft during First 10s of Warm Start Testing

Figure 26 shows the intake manifold absolute pressure (IMAP) during the startup. Initially, the air drawn into the engine was at the same pressure as the atmosphere, around 100 kPa. The IMAP decreased sharply to about 40 kPa within the first second of the start transient. At the

beginning of the startup the engine speed was not high enough to draw down the IMAP. As the engine speed increased, air and fuel were sucked into the cylinders at an increasing rate. This caused the IMAP to drop as a function of engine speed.

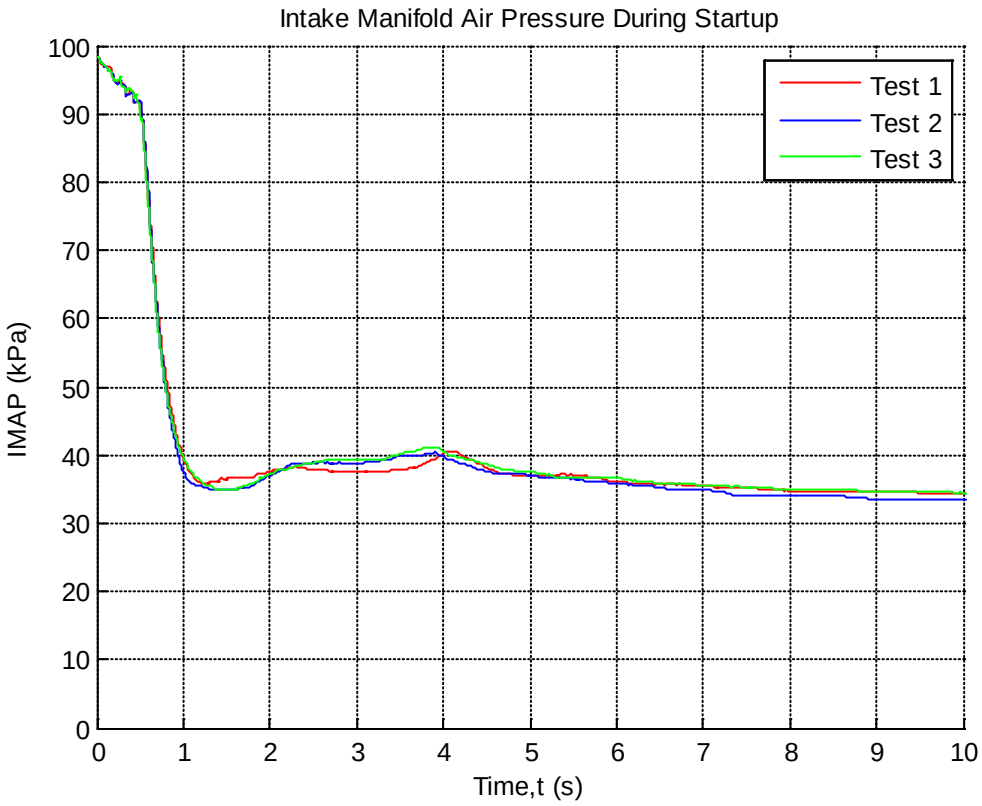

Figure 26: Intake Manifold Absolute Pressure during First 10 Seconds of Warm Start Testing

Figure 20 shows the fuel flow rate during the startup. Fuel was injected into the engine starting at around .45 seconds. Extra fuel was consumed at the beginning of each startup and peaked around 2 to 3 g/s before it decreased to the idle consumption rate of about 0.5 g/s. During the startup, the ECU injected extra fuel in order to create a rich air-fuel ratio (AFR). In typical engine operation this creates a fuel puddle in the intake port and causes cylinder wall wetting; this encourages the evaporation of the fuel, which is necessary to start combustion. The extra

fuel injected during the start also helps to prevent engine misfire, or knocking, that can be particularly damaging to the engine. Running rich at the startup prevents the uncontrolled burning of the air-fuel mixture that occurs if the mixture is detonated due to high pressure instead of spark ignition. This accidental detonation of the air-fuel mixture is called knocking and can result if the AFR is at stoichiometric during the engine startup.

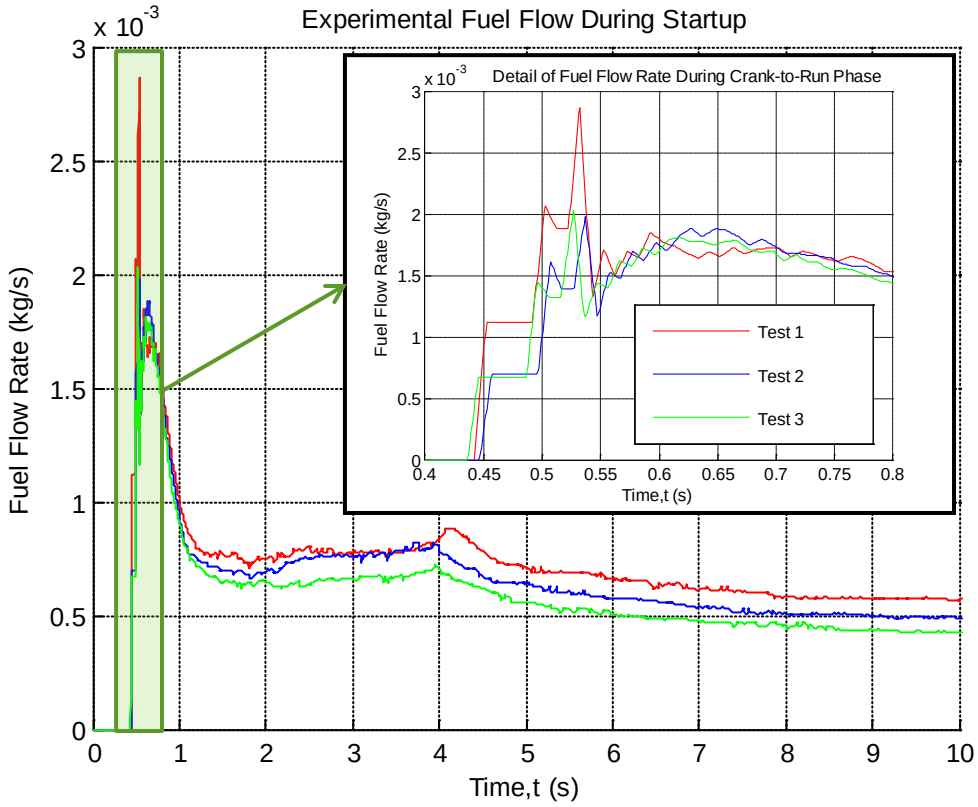

Figure 27: Fuel Flow Rate during First 10 Seconds of Warm Start Testing

The results presented in this section have focused on the physical interpretation of the complete startup for the vehicle during fully warmed conditions. This section also addressed the differences between each of the startup tests caused by the tests being run in succession. The next section focuses on breaking down a small portion of one complete test. The small portion addressed is termed the start transient and is of greatest concern for start/stop operation.

2.3.3 Isolation of Start Transient Events

For the purpose of modeling and the analysis conducted in Chapter 5 it is necessary to define the end of the start transient and isolate the various events that occur during this time. Figure 28 shows how the start transient is defined and broken down into separate events. Once the alternator output current became positive in the figure it was determined that the vehicle idle speed controller had taken over the engine dynamics. This occurred at 1.14 seconds for the second warm startup test. After this point, the alternator was turned on and the vehicle began to recharge the battery using the high idle speed as described in Section 2.3.2 . The engine consumed extra fuel to produce this high idle speed. During the high idle, the extra fuel energy was converted by the alternator into electrical energy that was stored in the battery. This energy is not part of the start transient and must not be included when considering start/stop operation. Therefore, the start transient ended at the moment in which the alternator started recharging the battery; this occurred at 1.14 seconds in test two of the warm start tests. Figure 29 shows that the end of the start transient occurred around the same time for each test conducted.

There are two phases that can be defined for the start transient: the cranking phase and the crank-to-run phase. Each phase is distinct in that the energy consumed to start the engine comes from different sources during the start transient. The cranking phase took the engine from rest to 200 rpm; the phase lasted around .45 seconds and the end of cranking was defined by when the engine speed began to rapidly increase due to combustion. The energy consumed during the cranking phase came solely from the battery. The crank-to-run phase occurred from the end of cranking at .45 seconds to the end of the start transient at 1.14 seconds. During the crank-to-run phase, the energy consumed to increase the engine speed came from fuel energy alone.

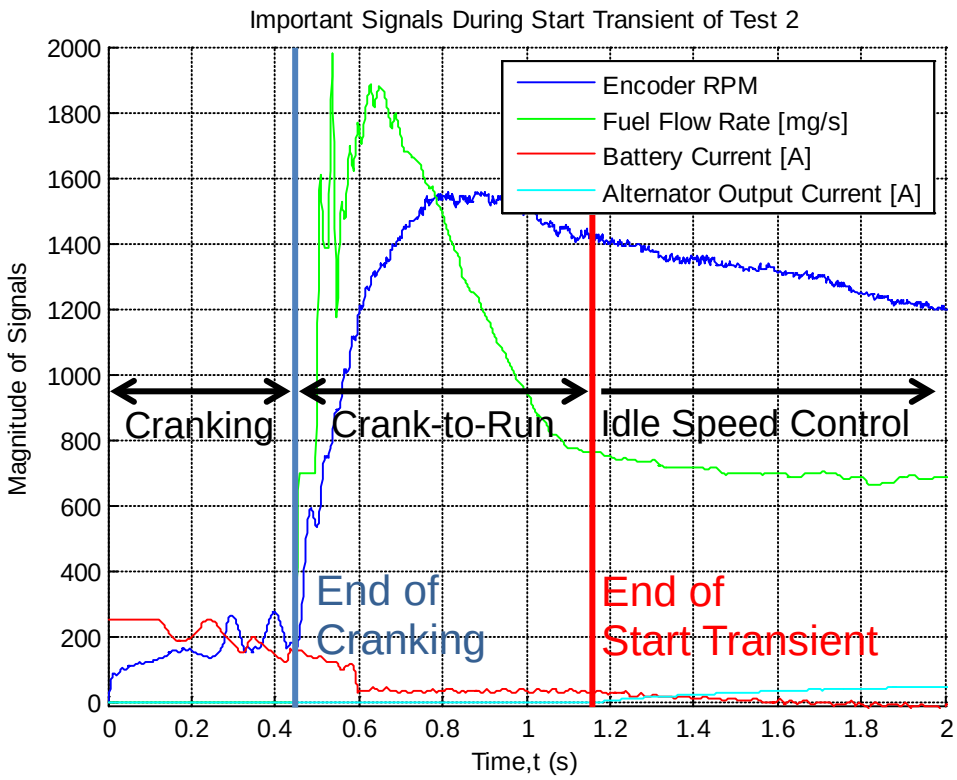

Figure 28: Isolation of Start Transient Events

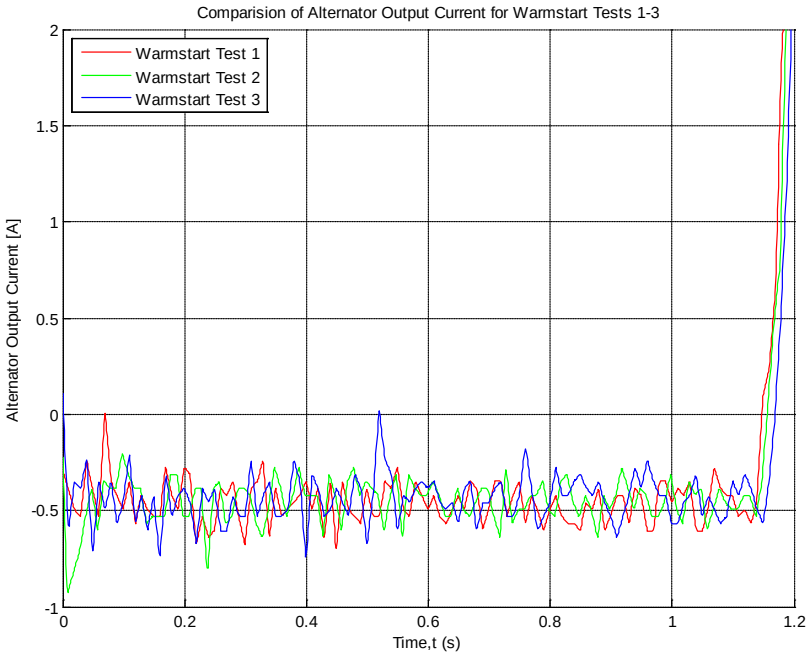

Figure 29: Alternator Output Torque for All Three Warm Start Tests

During the cranking phase, the DC electric starter was powered and provided a torque to the engine crankshaft that spun it up to the cranking speed of 200 rpm. This starter torque was determined experimentally from the variables collected during the warm start tests. Figure 30 shows the battery current and alternator output current. The superposition of these two current signals during the start transient was equal to the starter current plus the electrified auxiliary loads on the vehicle that were running during the start transient. From 0.6 to 1.14 seconds a 30 amp load was observed on the battery. This 30 amp load was equal to the current drawn by the auxiliary loads because the starter only drew current from the battery from 0 to 0.6 seconds. By scaling the superposition of the battery and alternator current the starter torque was separated from the vehicle loads and is shown as the inferred starter current in Figure 30.

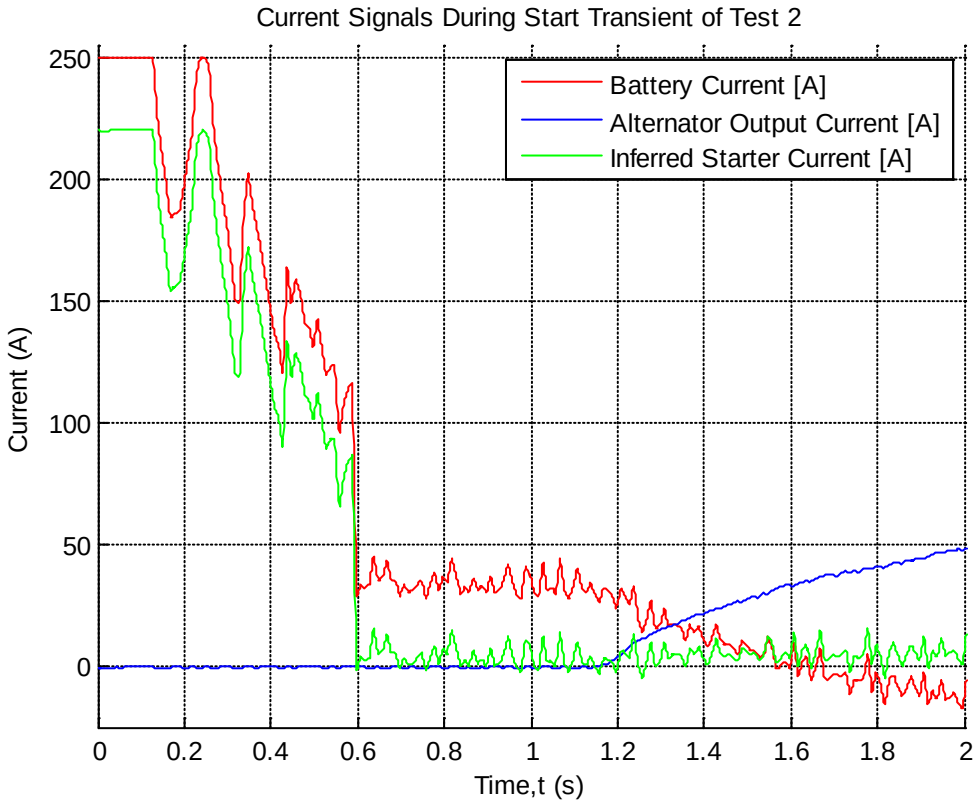

Figure 30: Current Signals for Start Transient

As mentioned above, the torque on the engine crankshaft during the cranking phase was produced by the starter. The starter consumed battery power to provide this torque; the electrical power consumption and the starter torque of warm start test two are shown in Figure 31 along with intermediate data used to calculate those values. The calculation of the electrical and mechanical power from the battery data was covered in Section 2.3.2. The figure shown here is a synopsis of that data and is presented to show how the variables changed during the start transient.

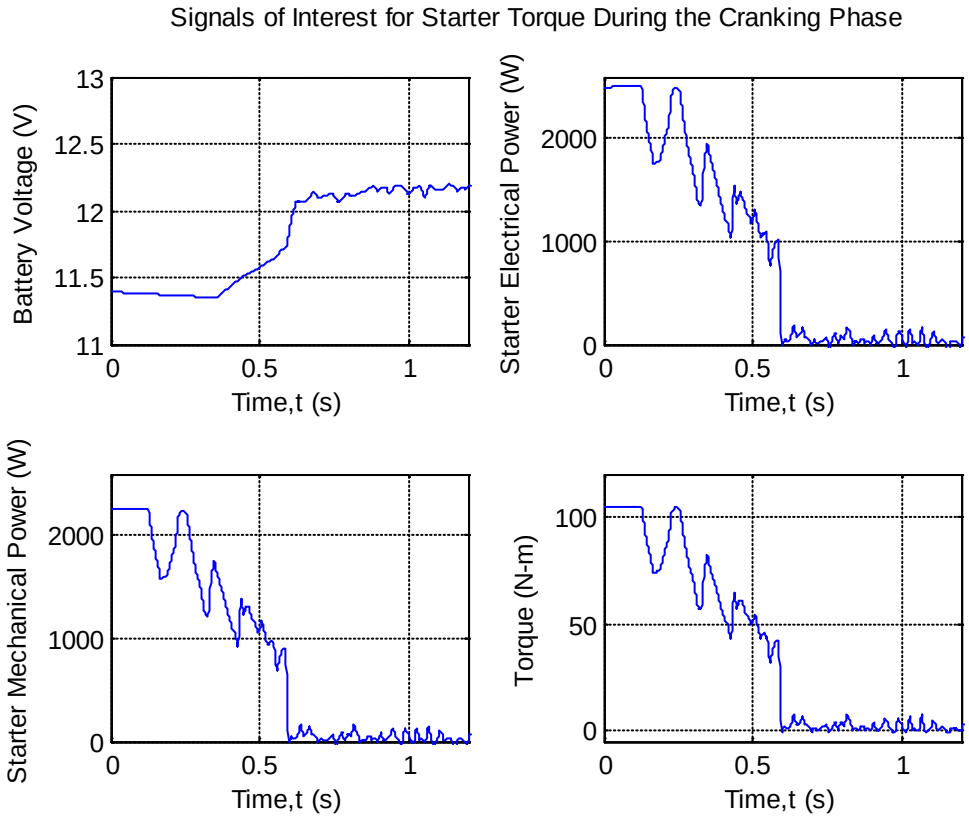

Figure 31: Variables Used to Calculate Starter Torque during Cranking Phase

The starter torque was found by dividing the mechanical power by the mean speed of the crankshaft from 0.2 to 0.4 seconds of the cranking phase, which was 205 rpm. During this portion of the cranking phase the engine speed fluctuated due to the compression events that

occurred in the unfired, or motored, cylinders of the engine. The pumping losses just described can be seen in the current, power, and torque curves as sharp drops in each signal from 0.2 to 0.4 seconds.

The cranking phase ended after around .45 seconds; however from .45 to 0.6 seconds the starter still supplied a small amount of torque to the crankshaft. This coincides with the first firing event and the beginning of fuel injection as shown in Figure 32 for the crank-to-run phase. Therefore, overlap between the battery energy and fuel energy existed in the test from .45 to 0.6 seconds.

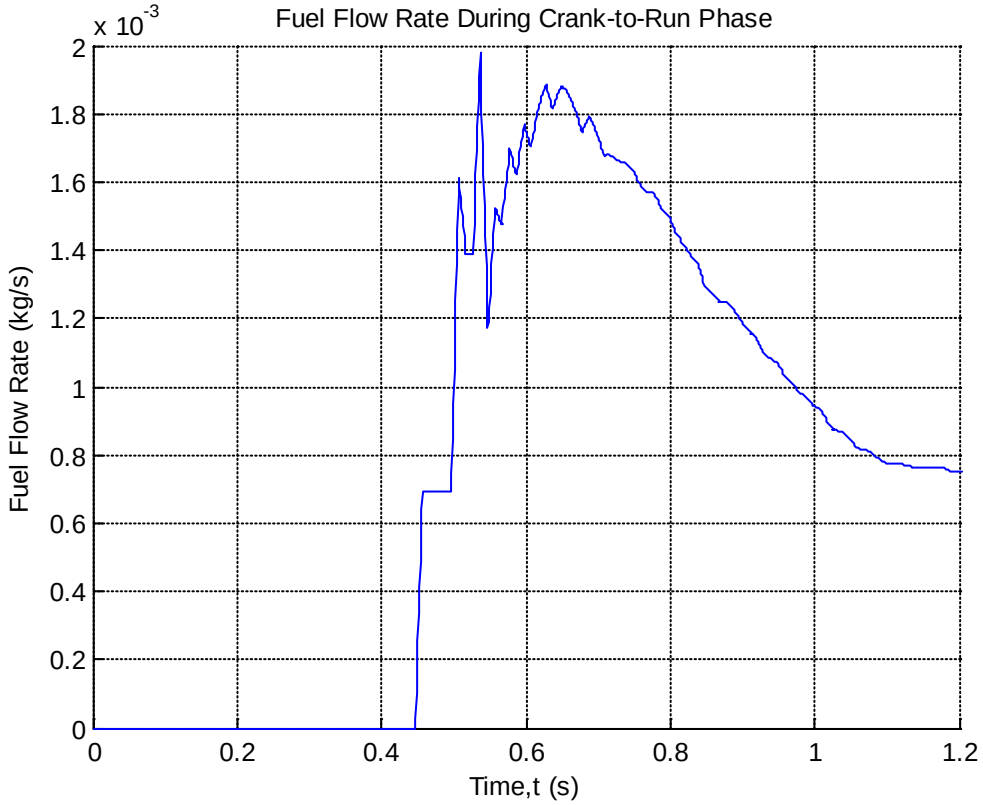

Figure 32: Fuel Flow Rate during Crank-to-Run Phase

Chapter 3: Model Development, Calibration and Validation

3.1 Model Motivation

As a result of the experimental study detailed in Chapter 3, a model of the engine startup dynamics was developed in order to further understand the relevant system dynamics and to investigate the energy consumption from fuel and the battery during the start transient. The model provided detailed information about the torque produced by the starter and the engine during the start transient. This torque was input into a single degree of freedom crankshaft model. The model was implemented in Simulink and model parameters were imported from MATLAB. The total model is capable of accurately predicting instantaneous cylinder pressure, torque, and engine speed. The model was calibrated and validated on preliminary experimental results similar to the results covered in Chapter 3.

3.2 Model Development

To capture the startup dynamics during the start transient, it was necessary for the model to have a high resolution in order to characterize the torque and speed fluctuations associated with the engine firing events. The dynamics associated with the cranking phase were accounted for by creating a saturation limited starter model that was input to the crankshaft model. The dynamics related to the crank-to-run phase and idle speed conditions were accounted for by coupling a crank angle based model of the engine torque output with the crankshaft model. Figure 33 shows a diagram of the model hierarchy. The rest of this section describes in detail the assumptions and the governing equations that characterize the system components of the engine startup model.

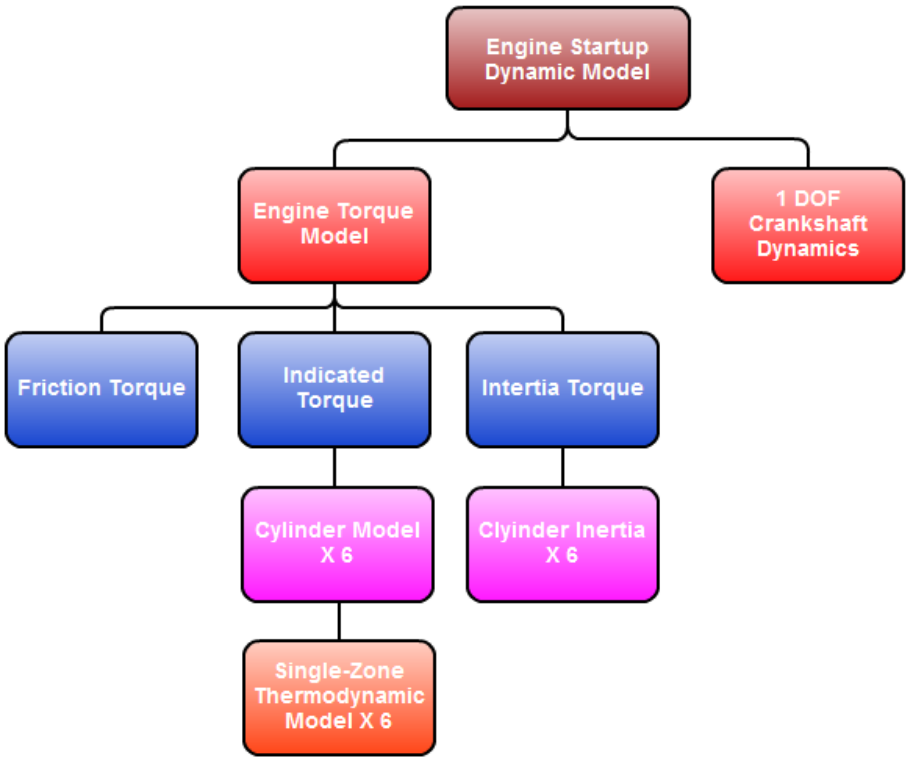

Figure 33: Crank Angle Based Model Hierarchy (Starter Model Not Shown)

3.2.1 Engine Model

Crank-Slider Geometry, Volume, and Brake Torque

The engine torque model characterized the instantaneous torque fluctuations of the six cylinder engine by accounting for the in-cylinder thermodynamics, the crank-slider dynamics, and the relationships between these subsystems. An accurate model is achieved by calculating the instantaneous torque with a resolution of 1 CAD [17]. The engine torque model, developed in the crank angle domain, considered the crankshaft position θ_E as the independent variable. Figure 34 shows the crank-slider geometry that was used to calculate the instantaneous piston position s, velocity $\dot{s}$, and acceleration $\ddot{s}$.

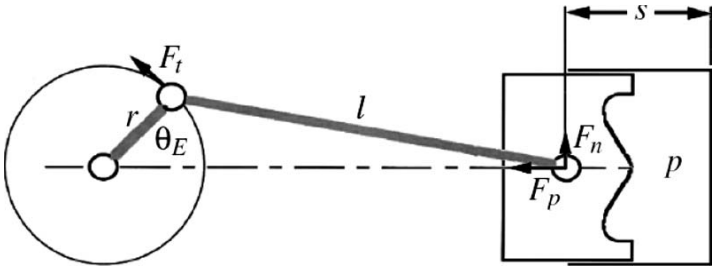

Figure 34: Idealized Crank-Slider Geometry for One Engine Cylinder [17]

The piston position s for each cylinder in the model was calculated from the geometry of the crank-slider mechanism and was found as a function of the angular crankshaft position θ_E. Equation (3.1) shows the calculation of piston position s from crank-slider geometry where $R = l/r$.

$$s = l + r\left[1 - cos\,\theta_E - (R^2 - sin^2\,\theta_E)^{\frac{1}{2}}\right] \tag{3.1}$$

The piston position, velocity, and acceleration parameters were found using engine geometry provided by Chrysler. These functions were implemented in the engine torque model as lookup tables.

The instantaneous cylinder volume and its derivative were also calculated [24] from equation (3.1) where V_c is the clearance volume and C_r is the compression ratio. The clearance volume is the volume between the piston head at TDC and the top of the cylinder that accommodates for the intake and exhaust valves [25]. The compression ratio is total volume divided by the clearance volume. The total volume is the displaced volume plus the clearance volume. The displaced volume is equal to the area of the cylinder bore multiplied by the engine stroke length. The clearance volume and the compression ratio were provided by Chrysler. Equation (3.2) shows how the instantaneous cylinder volume was calculated as a function of crankshaft position

θ_E in the model. The volume function and its derivative were also pre-calculated in MATLAB and imported to the model as lookup tables.

$$V = V_c + \frac{1}{2}V_c(C_r - 1)\left[R + 1 - \cos\theta_E - \sqrt{R^2 - \sin^2\theta_E}\right] \quad (3.2)$$

The total engine output, or brake, torque is made up of three torque terms. The indicated torque, the inertia torque, and the friction torque. The indicated torque is the torque due to combustion in the cylinders and is a net positive torque over one engine cycle. The inertia torque is due to the force needed to accelerate and decelerate the piston mass and a portion of the connecting rod mass. The torque required to move this reciprocating equivalent mass is cyclic and is a net zero torque over one engine cycle. The friction torque term is the torque needed to overcome the rubbing friction of the rotating and sliding parts of the engine, accessories, and the crankshaft. The friction torque was not crank angle resolved and was approximated over an entire cycle. It was an average of the actual friction fluctuations that occurred as cycle-based phenomena. Equation (3.3) shows the equation for the engine brake torque accounting for the indicated, inertia, and friction torques as functions of crankshaft position [17].

$$T_{cylinders}(\theta_E) = T_{indicated}(\theta_E) + T_{inertia}(\theta_E) - T_{friction}(\theta_E) \quad (3.3)$$

Engine Thermodynamics and Indicated Torque

In order to capture crank angle resolved indicated torque fluctuations, the in-cylinder pressure was calculated from a simplified single-zone, thermodynamic model [17]. This model considered the combustion chamber volume a closed thermodynamic system from Intake Valve Closing (IVC) to Exhaust Valve Opening (EVO) and assumed uniform pressure and temperature

[17]. By applying the mass and energy conservation principles to the combustion chamber volume from IVC to EVO the single-zone thermodynamic equation (3.4) [24] was derived.

$$\frac{dU}{d\theta_E} = \frac{dQ_g}{d\theta_E} - \frac{dQ_w}{d\theta_E} - p\frac{dV}{d\theta_E} \tag{3.4}$$

In equation (3.4), U was the internal energy, Q_g was the gross heat release from fuel energy during combustion, and Q_w was the heat lost to the cylinder walls and piston head mass. Because the duration of the start transient was much less than the time constant for heat loss dynamics, the Q_w term was able to be neglected [17]. Using the ideal gas law and constant specific heats equation (3.4) was simplified to equation (3.5) where γ represents the ratio of specific heats [26]. Integrating this equation yielded the estimated in-cylinder pressure from IVC to EVO [27].

$$\frac{dp}{d\theta_E} = -\gamma\frac{p}{V}\frac{dV}{d\theta_E} + \frac{(\gamma-1)}{V}\frac{dQ_g}{d\theta_E} \tag{3.5}$$

Heat release only occurred for the duration of combustion inside the CAD window from IVC to EVO. Therefore, the combustion heat release was simplified and modeled as shown in equation (3.6) where Q_{LHV} was the lower heating value of the fuel and M_{fuel} was the mass of fuel injected per cycle (per cylinder) [17]. The product of Q_{LHV} and M_{fuel} is termed the combustion gain (CG) and is addressed in Section 3.3.2.

$$\frac{dQ_g}{d\theta_E} = M_{fuel}Q_{LHV}\frac{dx_b}{d\theta_E} \tag{3.6}$$

In equation (3.6), x_b was the fuel mass burn fraction during one cycle and was expressed in the model using a function that was fit to the shape of the heat release for the duration of

combustion. This function is called the Wiebe function and is shown in equation (3.7) where m_b was the amount of burnt fuel, m_t was the total fuel, θ_0 was the start of combustion (SOC), $\Delta\theta$ was the duration of combustion, and parameters *a* and *m* where used to control the shape of the curve [24]. The Wiebe function used in the model was calibrated based on experimental results and is discussed in Section 3.3.1.

$$x_b = \frac{m_b}{m_t} = \begin{cases} 0 \; if \; \theta_E \; < \theta_0 \\ 1 - exp\left[-a\left(\frac{\theta_E - \theta_0}{\Delta\theta}\right)^{m+1}\right] \; if \theta_E \; \geq \theta_0 \end{cases} \tag{3.7}$$

The in-cylinder pressure from equation (3.5) was converted into the engine indicated torque by calculating the pressure force acting on the cylinder head and the resulting torque that acted on the crankshaft due to the geometry of the crank-slider mechanism shown in Figure 34. Equation (3.8) shows the calculation of the indicated torque based on the decomposition of the pressure force F_p acting on the piston bowl cross-sectional area multiplied the crank radius r [17]. The ambient pressure is denoted by p_{amb} in the equation.

$$T_{indicated} = rA_p(p - p_{amb})\left[sin\,\theta_E + \frac{sin\,\theta_E\, cos\,\theta_E}{\sqrt{R^2 - sin^2\,\theta_E}}\right] \tag{3.8}$$

In order to determine the pressure for the portion of the cycle outside of IVC to EVO assumptions were applied to simplify the calculation of the modeled in-cylinder pressure. Blowdown and overlap phases during the engine cycle were ignored. During the intake stroke, when the intake valve was open, the in-cylinder pressure was assumed to be equal to the IMAP as was given by a lookup table that matched experimental data from the warm start test results. When the exhaust valve was open the in-cylinder pressure was assumed constant and equal to the

ambient pressure. Figure 35 shows an example of the model based in-cylinder pressure for one cylinder over one complete engine cycle in CAD.

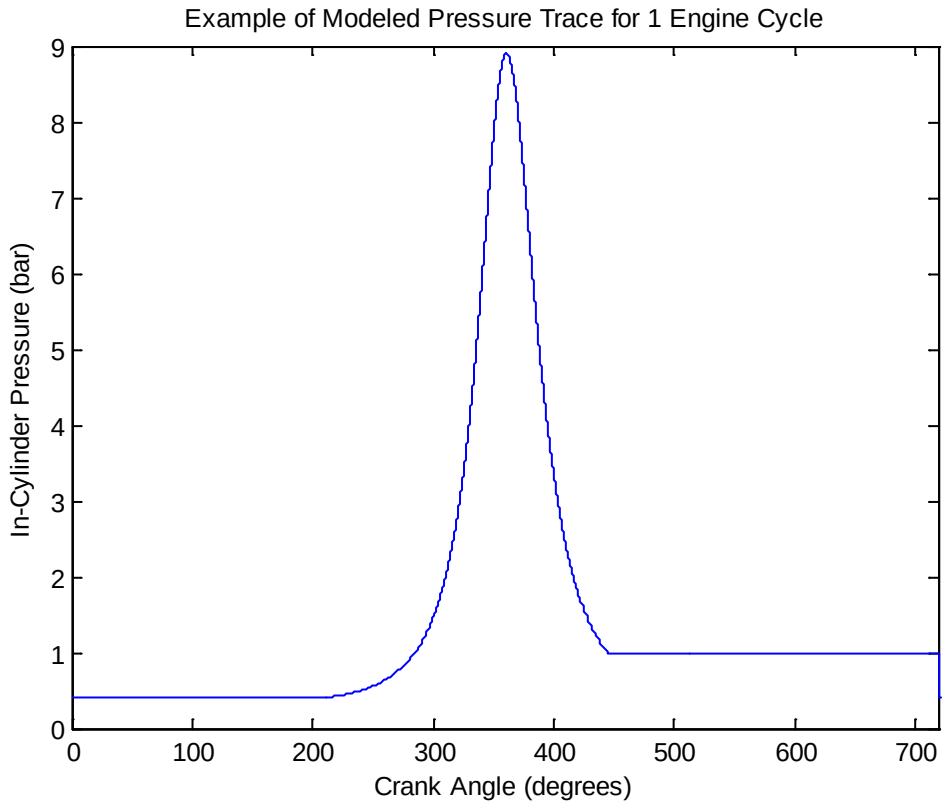

Figure 35: Example of Modeled In-Cylinder Pressure for One Complete Engine Cycle

Inertia Torque

The inertia torque was due to the force needed to accelerate and decelerate the equivalent mass of the piston, piston pin, and one third of the connecting rod mass. The rest of the connecting rod mass was lumped with the crankshaft [25]. The connecting rod was lumped into the mass of the crankshaft and the piston mass because it was idealized as a weightless, rigid body in the crank-slider geometry of Figure 34 and denoted by length *l*. The inertia torque calculation in

Equation (3.9) is based on product of the crank radius r and the decomposition of the inertia force F_m.

$$T_{inertia} = rF_m(\theta_E)\left[sin\,\theta_E + \frac{sin\,\theta_E\,cos\,\theta_E}{\sqrt{R^2 - sin^2\,\theta_E}}\right] \tag{3.9}$$

The inertia force is based on Newton's dynamics and considers the nonlinear inertia of the reciprocating mass as an external torque [17]. This inertia force F_m is calculated from the crank-slider geometry of Figure 34 and is shown in equation (3.10) where $M_{eq}$is the equivalent mass described above, $\ddot{s}$ is the piston acceleration, s is the piston position of equation (3.1), and $\ddot{\theta_E}$ and $\dot{\theta_E}$ are the crankshaft angular velocity and acceleration covered in Section 3.2.2.

$$F_m(\theta_E) = M_{eq}\ddot{s} = M_{eq}\left(\frac{ds}{d\theta_E}\ddot{\theta}_E + \frac{d^2s}{d\theta_E^2}\dot{\theta}_E^2\right) \tag{3.10}$$

Note here that the inertia torque was calculated and implemented in the model based solely on engine geometry.

Friction Torque

The friction torque was calculated as per equation (3.11) [17] based on the engine speed and the IMAP.

$$T_{friction} = T_{fr_0} + k_p p_{IM}(\theta_E) + k_{pw} p_{IM}(\theta_E)\dot{\theta}_E + k_{w_1}\dot{\theta_E} + k_{w_2}\dot{\theta_E^2} \tag{3.11}$$

Where the model coefficients T_{fr_0}, k_p, k_{pw}, k_{w_1}, and k_{w_2}were calibrated from the experimental testing detailed in Section 3.3.1.

3.2.2 Crankshaft Model

The torques developed in the engine and starter models were input to a single degree of freedom crankshaft dynamics model. The model assumed rigid body motion for the engine crankshaft and the masses connected to it. Figure 36 shows a diagram of the idealized crankshaft model.

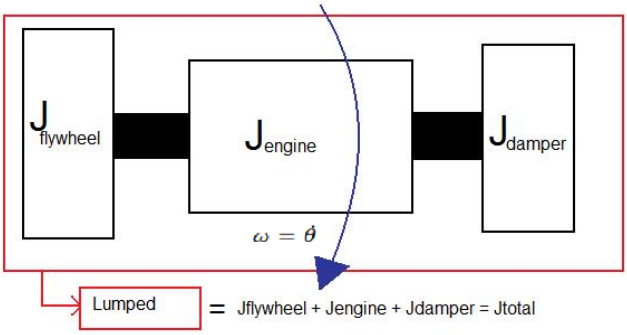

Figure 36: Single Degree of Freedom Crankshaft Model

The inertia of the model was lumped into a single, equivalent inertia equal to the sum of the inertia from the crankshaft, the flywheel, and the harmonic damper of the engine. The inertia of the connecting rod ends was also included in the crankshaft inertia. The values for the inertia were provided by Chrysler or estimated from measured geometry. Equation (3.12) shows the second order linear differential equation that describes the motion of the crankshaft dynamics.

$$J_{total}\ddot{\theta}_E = T_{cylinders} + T_{starter} + T_{load} - B\dot{\theta}_E \tag{3.12}$$

This equation was implemented in the model where $T_{cylinders}$ was the torque from the engine torque model during the crank-to-run phase, $T_{starter}$ was the torque applied during the cranking phase, T_{load} was zero in the model since only startup was concerned, and B was the damping of the system. The outputs of the crankshaft dynamics model were crankshaft angular position θ_E, velocity $\dot{\theta_E}$, and acceleration $\ddot{\theta_E}$.

3.2.3 Starter Model

The starter model was designed to input the starter torque to the engine crankshaft model during the cranking phase of the start transient. The starter on the Chrysler minivan was a DC electric motor. It was desired to create a starter model that matched DC electric starter operating characteristics.

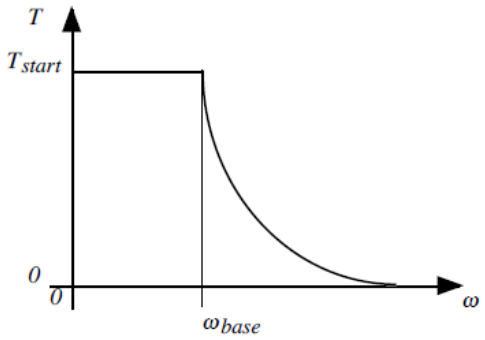

Figure 37: Sample motor torque-speed curve [28]

Figure 37 shows the torque-speed curve for an ideal electric motor. The ideal motor is characterized by its limits for torque and power. Initially, the motor operates at its maximum torque until it reaches some base speed. Once the base speed is reached, the motor reaches its power saturation limit and operates at constant power for the remainder of its speed range. Note the parabolic decrease in motor torque as the speed increases is due to equation (3.13) relating torque and power where $\omega = \dot{\theta}_E$. The peak torque and peak power of the motor were calibrated based on experimental data shown in Section 3.3.2.

$$P\,[W] = T[Nm] * \omega\,[\frac{rad}{s}] \tag{3.13}$$

A dynamic saturation was used in the starter model to capture the motor characteristics described above. The starter model was forced to operate at its saturation limits, either maximum torque or

maximum power depending on which limit was reached. Since the speed of the starter increased throughout the cranking phase, the starter model was first torque, then power limited.

3.2.4 Model Inputs/Outputs and Parameter Identification

As a result of the modeling approach used in this work, it was possible to characterize the engine startup dynamics with a limited number of parameters, as listed in Table 7.

Table 7: Identification of Model Parameters

Overview of Model Parameters		
Submodel	Parameters	Identification Source
Crank-slider geometry	r, l, V_c, C_r	Engine geometry
Engine thermodynamics and indicated torque	γ, Q_{LHV} $M_{fuel} Q_{LHV} = CG$ $a, m, \theta_0, \Delta\theta$ A_p	Fuel properties Warm start test data Idle engine dyno test data Engine geometry
Engine inertia torque	M_{eq}	Engine geometry
Engine friction torque	$T_{fr_0}, k_p, k_{pw}, k_{w_1}, k_{w_2}$	Chrysler "Big Grid" data
Crankshaft dynamics	J_{total}, B	Engine geometry
Starter	$T_{max}, P_{mech_{max}}, t_{cutoff}$	Warm start test data

In Section 3.3, the model parameters that needed to be identified by a test were calibrated using a combination of the experimental setups shown in Chapter 3. After these model parameters were calibrated the final model was determined and is summarized by the block diagram in Figure 38.

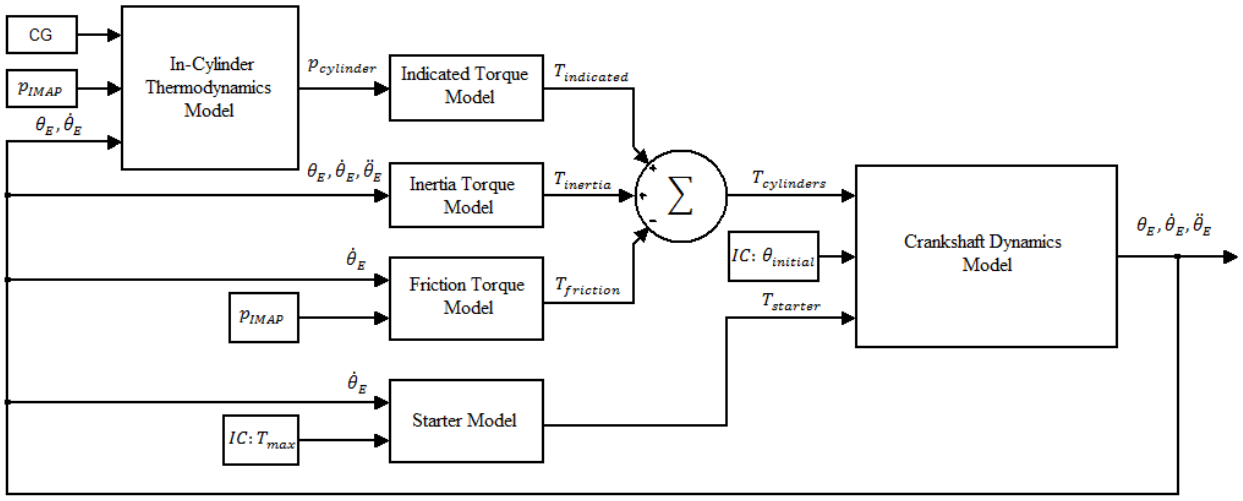

Figure 38: Model Summarized as Block Diagram

Note that Figure 38 shows only one sub-model for each of the in-cylinder thermodynamics, indicated torque, and inertia torque models. To capture the start transient of the V6 engine it was necessary to model the combination of the thermodynamics and indicated torque model along with the inertia torque model six times in total. Then each of the six models was individually implemented with the correct phasing for the V6 based on the angular location of the crankshaft pins and when TDC occurred for each cylinder. The engine has a 60 degree split-pin crankshaft.

3.3 Model Calibration

The model developed in Section 3.2 was characterized by a limited number of model parameters. Most of the model parameters were determined from engine geometry, properties, or were imposed on the model by knowing something about the operating conditions of the engine during the start transient. However, it was necessary to determine some of the model parameter experimentally. In other words, it was necessary to calibrate the model parameters based on experimental testing. This section addresses the calibration of these parameters. Included is the

calibration of the Wiebe function parameters and the friction torque coefficients from engine dynamometer testing. Calibration of the starter torque model saturation limits and cutoff time along with the calibration of the combustion gain (CG) input to the thermodynamic and indicated torque models is covered thereafter. Both of these calibrations were based on the results of a preliminary set of warm start test data. For these results, the length of the cranking phase was identified from the crankshaft speed trace and was significantly shorter than what was shown in the previous experimental results covered in Sections 2.3.2 and 2.3.3. The time stamp of the experimental starter torque was scaled to match this shortened cranking phase. The experimental fuel flow rate was also shifted to account for the shortened cranking phase.

3.3.1 Engine Dynamometer Testing

In this section, the results of the experimental tests conducted on the engine dyno for idle speed conditions were analyzed and used to calibrate the parameters of the Wiebe function described in Section 3.2.1. The testing setup, procedure, and results of the tests were covered in Chapter 3. The friction model calibration is also covered in this section and was determined from an analysis of the Chrysler Big Grid data, which were conducted on the engine dyno setup at Chrysler. The test procedure used to map the Big Grid data was also covered in Chapter 3.

Wiebe Function Fit Based on Engine Combustion Data

For the sake of modeling, it was necessary to capture the shape of the net heat release rate in order to calibrate the model parameter $\frac{dx_b}{d\theta_E}$ that described the fuel mass fraction burn rate over a single engine cycle. In order to characterize the net heat release at near idle conditions for the

3.6L V6 engine, the in-cylinder pressure trace for 3 different engine speed conditions was acquired on the engine dynamometer and used for calibration. For simplicity, the pressure traces of the three engine cylinders were ensemble-averaged to provide an indicative behavior of the engine combustion process.

Figure 39 shows the average, in-cylinder pressure of cylinders 1 through 3 for engine speeds at 625, 750, and 900 rpm; also shown is the pressure derivative that was used in the net heat release equation (3.14) introduced later in this section.

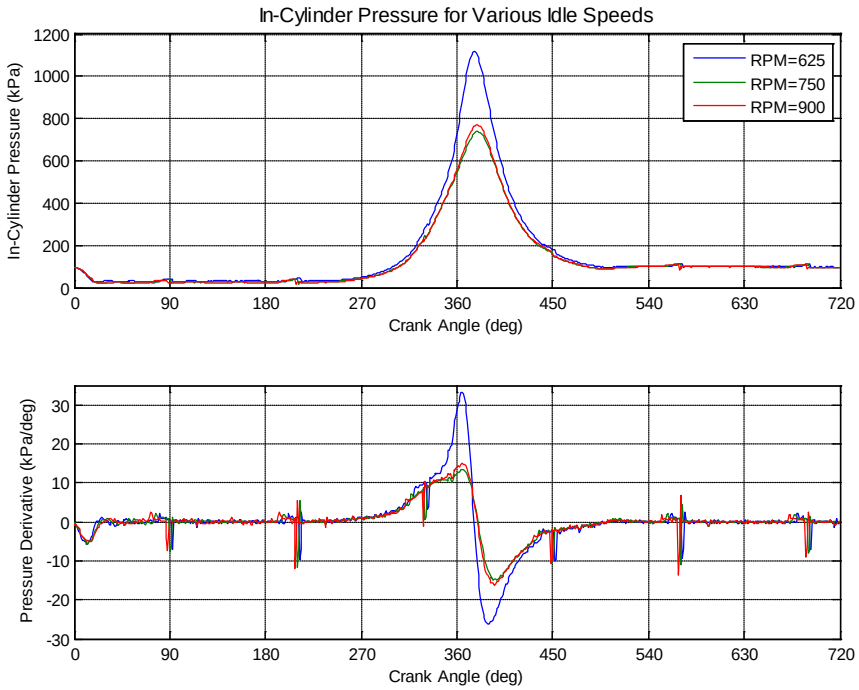

Figure 39: In-Cylinder Pressure and Pressure Derivative for Three Idle Speeds

Small fluctuations in the pressure derivative were found and shown to occur at a regular interval. Figure 16 and Figure 17 in the experimental results of Chapter 3 better show this pressure fluctuation and was especially pronounced for the cylinder one pressure trace. This fluctuation

was carried over into the average in-cylinder pressure and its derivative. This fluctuation is not physical and was a result of poor signal processing of the in-cylinder pressure during the testing. Figure 40 presents the cylinder volume and its derivative as a function of CAD over one engine cycle. The cylinder volume and the volume derivative were calculated using equation (3.2) and the derivative of this equation respectively. They are presented here because they were used to find the apparent heat release in the analysis version of the net heat release equation.

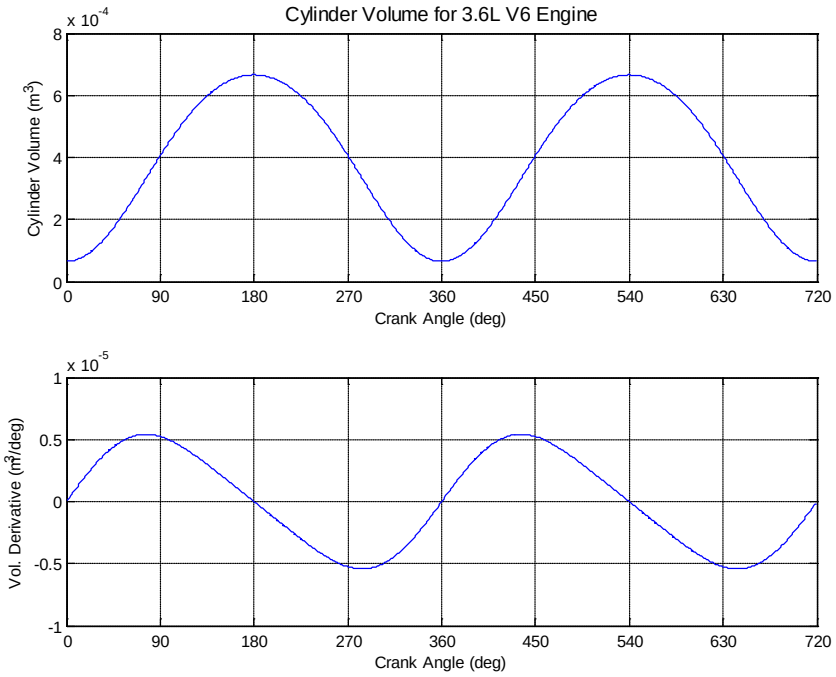

Figure 40: Cylinder Volume and Volume Derivative as a Function of CAD for One Cycle

Equation (3.14) is the analysis version of the heat release equation and was used to compute the net heat release over the one engine cycle from the start of combustion (SOC) to EVO [26]. The SOC was 337 degrees based on the spark advance of the engine around idle speed.

$$\frac{dQ_{net}}{d\theta_E} = \left(\frac{1}{\gamma - 1}\right) V \frac{dp}{d\theta_E} + \frac{\gamma}{(\gamma - 1)} p \frac{dV}{d\theta_E} \tag{3.14}$$

Figure 41 shows the net heat release rate that was calculated using equation (3.14) from SOC to EVO. The figure shows that there was a large negative spike in the heat release rate some CAD after combustion occurred. The negative spike in the net heat release rate is not related to any physical phenomena and is due to the translation of the error due to the poor signal processing of the in-cylinder pressure as discussed above. Therefore, this portion of the data was removed before the Wiebe parameters were fitted to the mass fraction burnt.

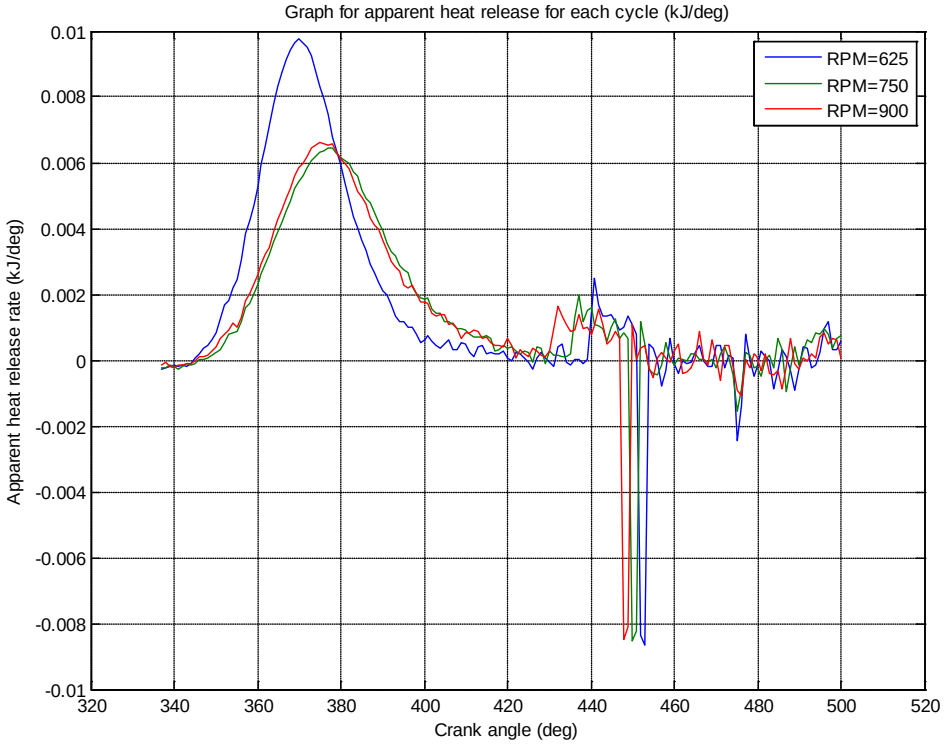

Figure 41: Net Heat Release Rate from SOC to EVO

The mass fraction burnt was calculated by taking the integral of the heat release rate, dividing it by the lower heating value of gasoline, and then normalizing the result. Figure 42 shows the total heat release found from integration and also the normalized mass fraction burnt at the three engine speeds tested.

The Wiebe function parameter θ_0 was equal to the SOC and the duration of combustion $\Delta\theta$ was the difference between the EVO (500 degrees) and SOC in degrees, which was 163 degrees.

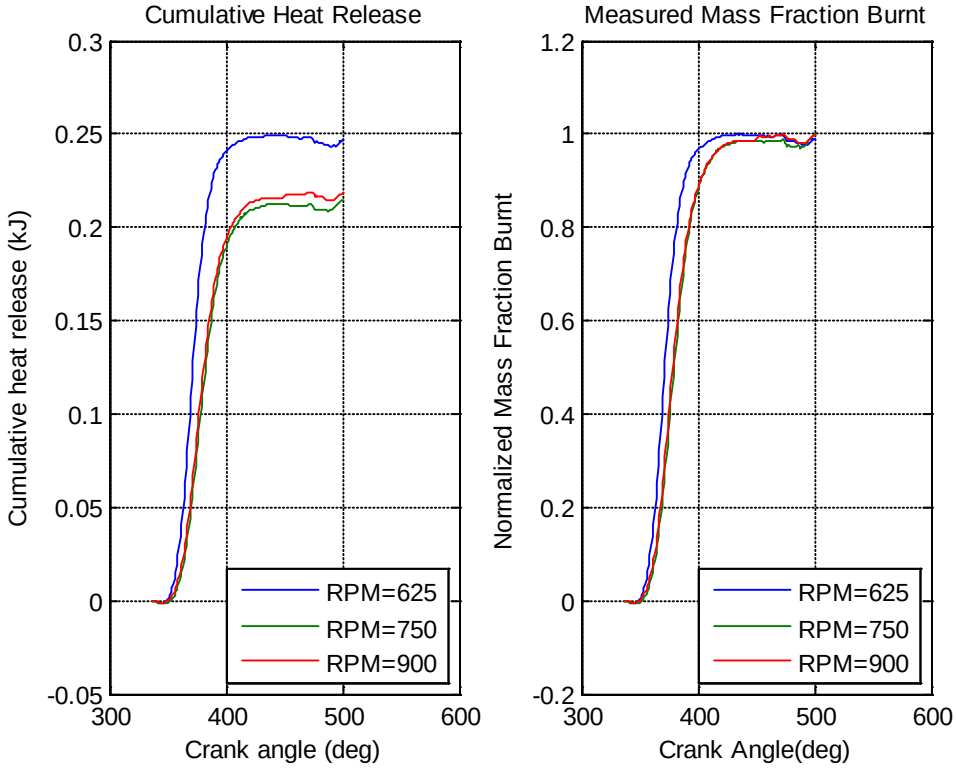

Figure 42: Total Heat Release Converted to Normalized Mass Fraction Burnt

Using MATLAB's *fminsearch* function, the Wiebe function presented in equation (3.7) was fitted to the measured mass fraction burnt by minimizing the error between the two curves. This was done by an iterative process that returned the best values for parameters *a* and *m* and is shown in Table 8. Figure 43 shows the result of the fitted Wiebe function compared to the experimentally determined mass fraction burnt. The Wiebe function provided an idealized shape for the mass fraction burnt that was implemented into the model to determine the indicated torque as described in Section 3.2.1. Figure 44 shows the derivative of the mass fraction burnt $\frac{dx_b}{d\theta_E}$, which is also the normalized heat release rate (NHRR), from SOC to EVO for the three

engine speeds tested. The NHRR for the 750 rpm test was selected for implementation in the model.

Table 8: Wiebe Function Fitting Parameters

	Wiebe Function Parameters	
Idle Speed (RPM)	"a"	"m"
625	0.3479	2.4390
750	0.4831	2.2352
900	0.5312	2.1080

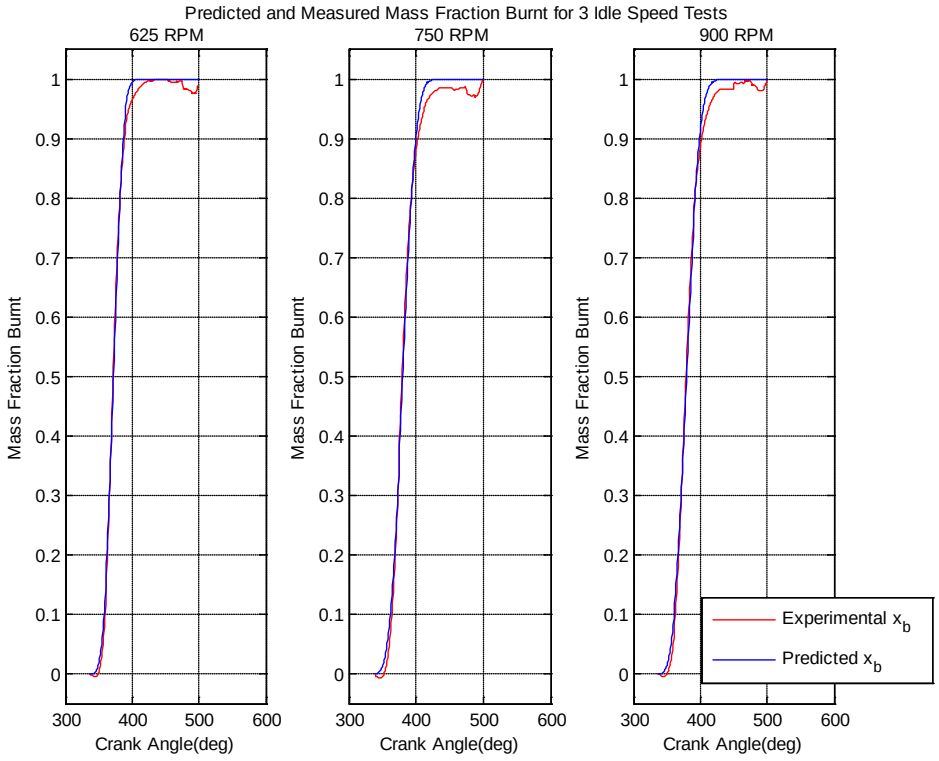

Figure 43: Wiebe Function fitted to Mass Fraction Burnt

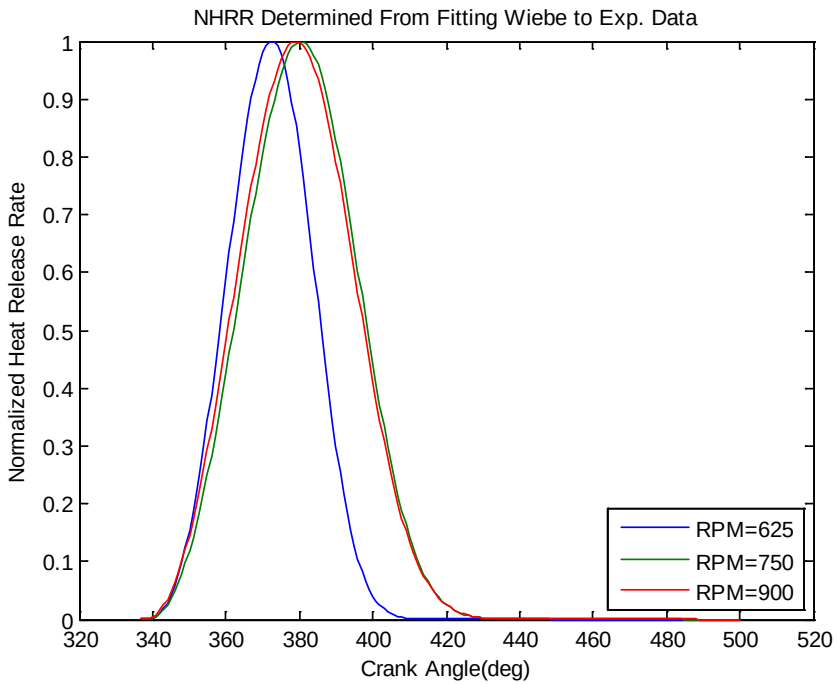

Figure 44: Normalized Mass Fraction Burnt Derivative from Fitted Wiebe Function

Friction Torque Fit Based on Engine FMEP Data

The engine temperature affects the friction torque by decreasing the friction losses as the engine fluids and mechanical parts heat up. For start/stop operation the engine is only restarted when the engine is in the fully warmed state; therefore, it is appropriate to ignore temperature affects so long as the friction model is calibrated for fully warmed conditions.

In order to calibrate the friction torque model presented in equation (3.11) it was necessary to calculate the friction torque from experiment. This was done by utilizing the Big Grid data provided by Chrysler, which contained cycle averaged data for the Pentastar engine at various steady state operating points. It was assumed that the engine was always operated at fully warmed conditions when Big Grid data points were determined. Cycle averaged data for various

types of engine pressures were recorded and used to find the friction torque. Equation (3.15) shows how friction mean effective pressure (FMEP) was calculated from experimental pressures measured during steady state testing.

$$FMEP = IMEP_G - PMEP - BMEP \tag{3.15}$$

Equation (3.15) was calculated for a range of engine speeds from 512 to 6400 rpm where $IMEP_G$ was the gross indicated mean effective pressure, $PMEP$ was the pumping mean effective pressure (positive magnitude), and $BMEP$ was the brake mean effective pressure. Using the FMEP is was possible to calculate the experimental friction torque at each operating point by equation (3.16) where V_d was total cylinder volume for all six cylinders, and N_c was the number of revolutions per cycle, which is 2 for the 4-stroke engine under consideration.

$$T_{friction} = \frac{FMEP * V_d}{2\pi * N_c} \tag{3.16}$$

Using MATLAB's *cftool* the experimental friction torque was plotted versus engine speed (rpm) and IMAP and equation (3.11) was fitted to the data. The resulting fit is shown in Figure 45 and Table 9 shows the values of the friction torque model coefficients.

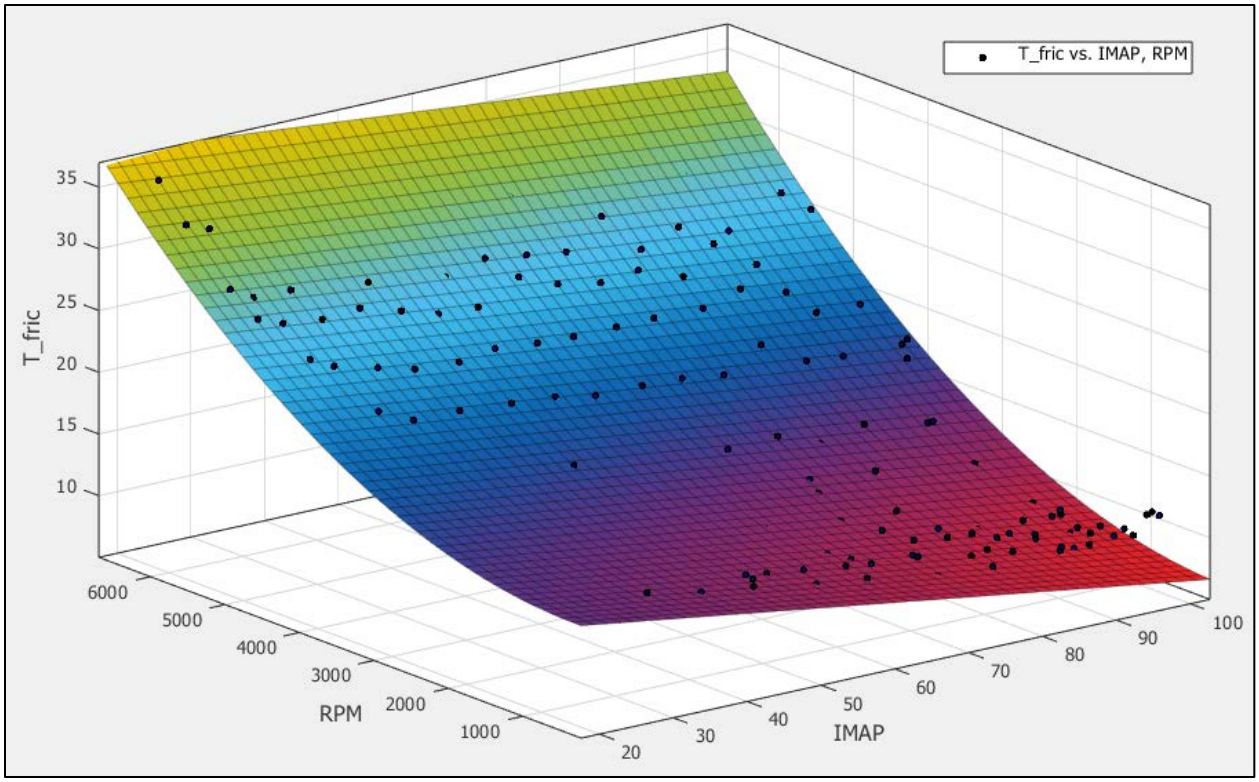

Figure 45: Friction Torque Fitting Based on Big Grid Data

Table 9: Friction Torque Parameters Fit to Big Grid Data

Friction Torque Fitting Coefficients	
T_{fr_0}	15.72
k_p	-0.08903
k_{pw}	5.202E-06
k_{w_1}	-4.201E-04
k_{w_2}	5.755E-07

3.3.2 Warm Start Vehicle Tests

At this point, the model parameters left to calibrate were the starter model saturation parameters, the starter model cutoff time, and the combustion gain (CG) profile. These parameters were determined from preliminary warm start transient test results as described in the beginning of Section 3.3.

In order to calibrate the final model parameters, it was necessary to match the simulated engine speed profile of the model with the experimental engine speed profile for the duration of the start transient. This was done in two steps. First, the simulated speed profile was matched to the experimental profile during the cranking phase. Then, the simulated profile was matched to the experimental profile during the crank-to-run phase by adjusting the model CG.

Calibrated Engine Speed Profile

The fully calibrated model was based on the agreement of the simulated engine speed matching the warm start experimental engine speed profile during the start transient. Figure 46 shows the crankshaft speed output of model matched to the warm start experimental speed trace.

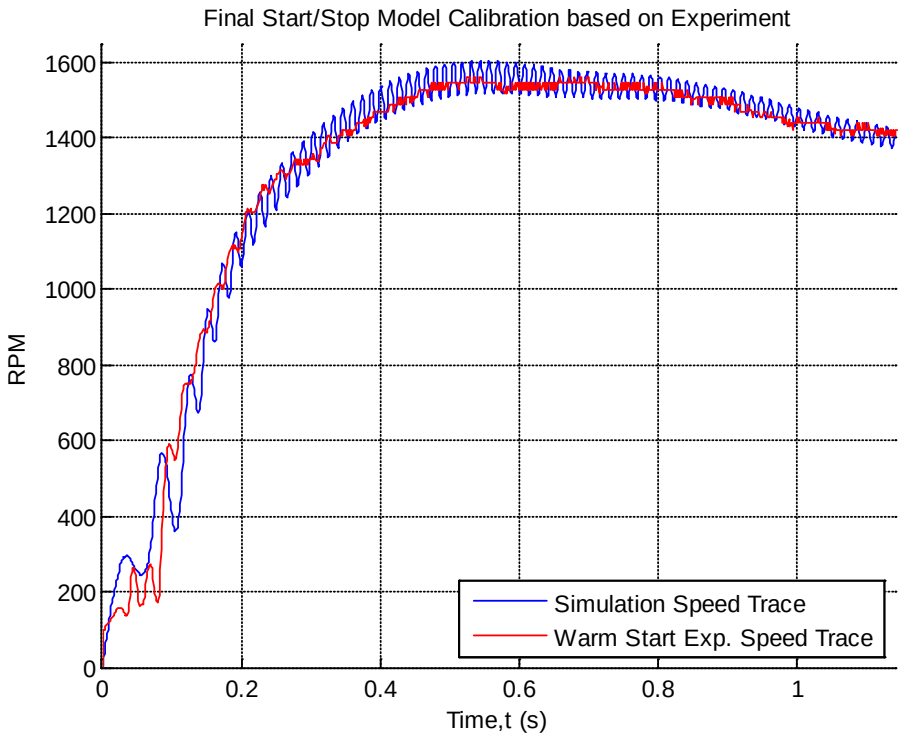

Figure 46: Simulated Engine Speed Calibrated to Warm Start Exp. Engine Speed

Starter Torque Calibration

To match the simulated speed trace to the experimental speed trace during the cranking phase, the starter model saturation limits for torque and power, as well as the torque cutoff time were determined based on the experimental data acquired from a warm start test. The maximum experimental torque during the cranking phase was 110 Nm. The maximum experimental power during cranking was 2750 W. These saturation limits were implemented in the starter model of Section 3.2.3 as the calibrated motor characteristics. At 0.06 seconds the model starter torque was cutoff in order to match the scaled experimental starter torque. The cutoff was the end of the cranking phase and was identified based on the experimental engine speed trace shown in

Figure 46. A comparison of the calibrated starter motor torque and the experimentally determined starter torque is shown in Figure 47.

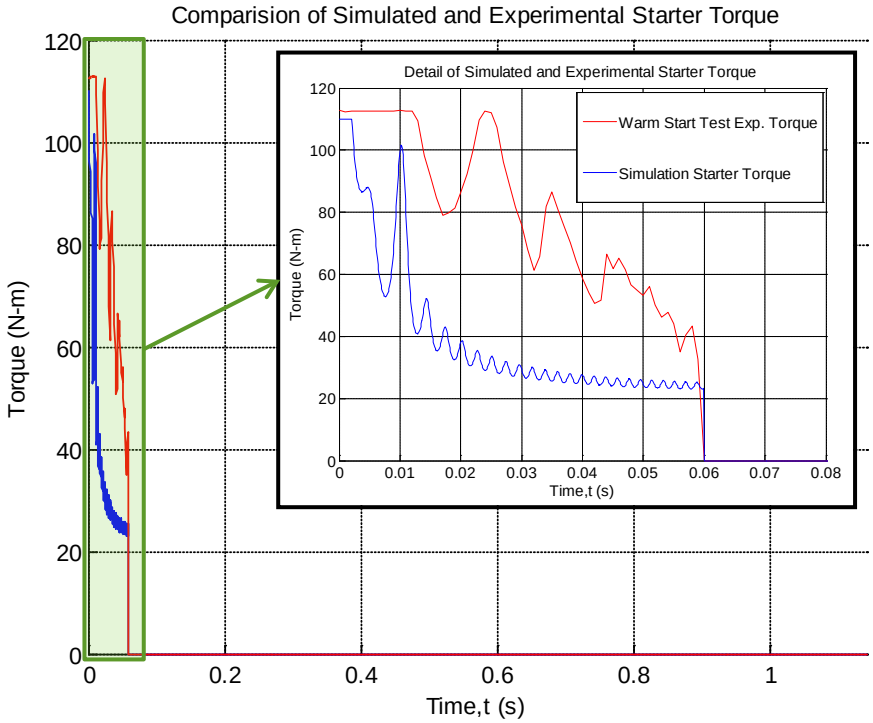

Figure 47: Calibrated Starter Torque Compared to Experimental Starter Torque

Combustion Gain Calculation and Calibration

In the thermodynamics and indicated torque model described in Section 3.2.1, the product of the lower heating value of gasoline Q_{LHV} and the mass of fuel injected per cylinder per cycle M_{fuel} was introduced as the Combustion Gain (CG). CG may be thought of as the amount of fuel energy entering each of the six engine cylinders over one complete engine cycle.

The experimental CG can be determined knowing the experimental fuel flow rate and the engine speed during the start transient. The experimental fuel flow rate used to determine CG is shown

in Figure 48. Equation (3.17) shows how CG was calculated from fuel flow rate and engine speed; the unit conversion was included for clarity.

$$CG[J/Cylinder/Cycle] = \frac{\eta_f \dot{m}_f Q_{LHV}}{N_{RPM}} \left[\frac{\frac{kg}{s} \cdot \frac{J}{kg}}{\frac{rev}{min}}\right] \cdot \left[\frac{2\,rev}{cycle} \cdot \frac{60\,s}{min} \over 6\,cylinders\right] = 20\frac{\eta_f \dot{m}_f Q_{LHV}}{N_{RPM}} \qquad (3.17)$$

In equation (3.17), η_f was the fuel conversion efficiency, $\dot{m}_f$ was the fuel flow rate, and N_{RPM} was the instantaneous engine speed sensed by the ECU in revolutions per minute.

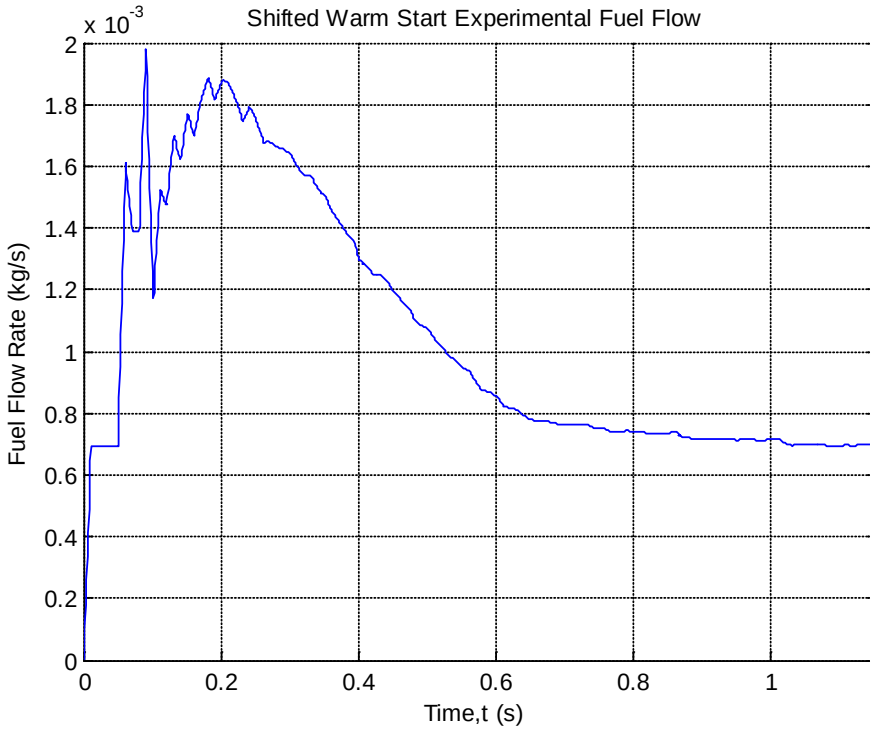

Figure 48: Experimental Fuel Flow Rate for Calibration

Equation (3.18) [24] shows how the fuel conversion efficiency η_f was found for idle speed based on the Big Grid data where P_{brake} was the brake power recorded by the engine dyno.

$$\eta_f = \frac{P_{brake}}{\dot{m}_f Q_{LHV}} \qquad (3.18)$$

In order to calibrate the model, the simulated speed trace during the start transient was matched to the warm start experimental speed trace. A comparison of the calibrated CG and the experimental CG is shown in Figure 49. A constant fuel conversion efficiency of 20% was used for calculating the experimental CG shown in the figure.

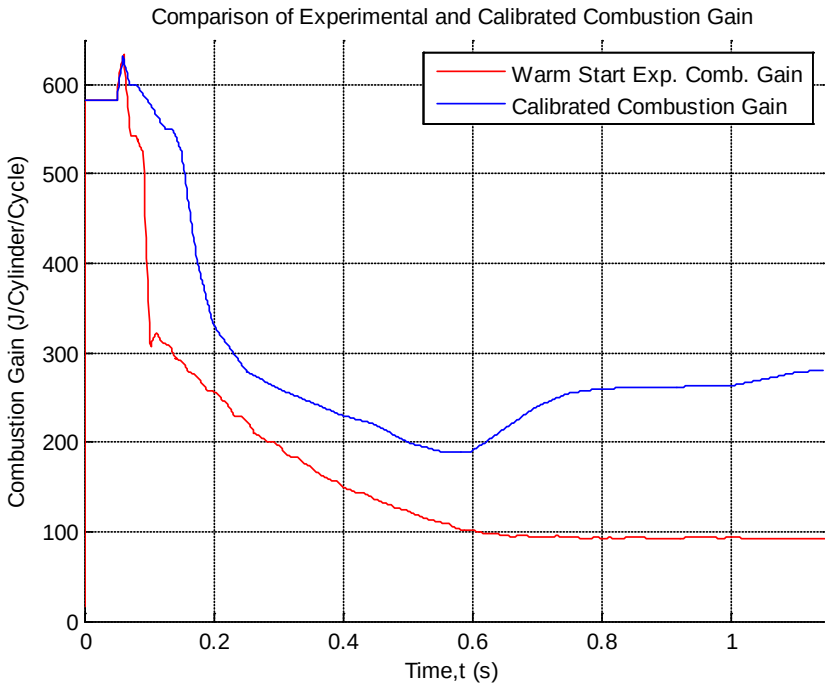

Figure 49: Comparison of Warm Start Experimental and Calibrated Combustion Gain

The focus for the CG calibration was on the portion of the profile during the crank-to-run phase of the start transient. However, it was noteworthy that according to the experimental data for fuel flow rate and CG, extra fuel was injected during the cranking phase of the start transient. This consumption of extra fuel appeared in the model calibrated CG as well. The extra fuel injected at the beginning of the start transient caused the engine to accelerate from the 250 rpm cranking speed to idle speed. The reduction of the extra fuel consumed during the start transient is analyzed using the fully calibrated model in Chapter 5.

3.4 Model Limitations

The startup dynamic model developed was based on approximations and assumptions that were detailed throughout Chapter 4. Figure 47 shows a comparison of the modeled starter torque and the experimental starter torque. The differences in the two torque traces caused a significant difference in the amount of total battery energy consumed between the model and the experiment during the engine cranking phase. This difference could be due to errors in determining the experimental peak torque and power, which were used as calibration parameters for the model. These values were found by inferring the starter current during the cranking phase as was detailed in Section 2.3.2. Instead of inferring the starter torque it could be measured directly by placing a current shunt on the starter. Also note that the experimental starter was approximated as an ideal DC motor, which may not be accurate enough for characterizing the starter.

Figure 49 shows the model CG compared to the experimental CG. The difference between the two traces was the resulting cumulative error of the modeling approach and errors in acquiring the experimental data. The error was likely due to inaccuracies in the friction model, which were twofold. First, the calibrated friction torque was inaccurate for low engine speeds during cranking due to extrapolation of the friction model for speeds below 512 rpm. This could be accounted for in the model by adding a calibration parameter for the cranking portion of the test, and could be calibrated by matching the model speed trace to the experimental speed trace during a stop transient. Second, the friction model was a cycle-resolved model, which averaged the friction fluctuations over each cycle. A more accurate way to capture the friction fluctuations during the start transient would be to develop a friction model that was based in the crank angle domain. This could be developed from experiment by using the methods described in [25].

3.5 Model Validation

Figure 50 shows the start transient of the fully calibrated model compared against three different warm start transients. The agreement between the simulated model speed trace and the various experimental speed traces was good.

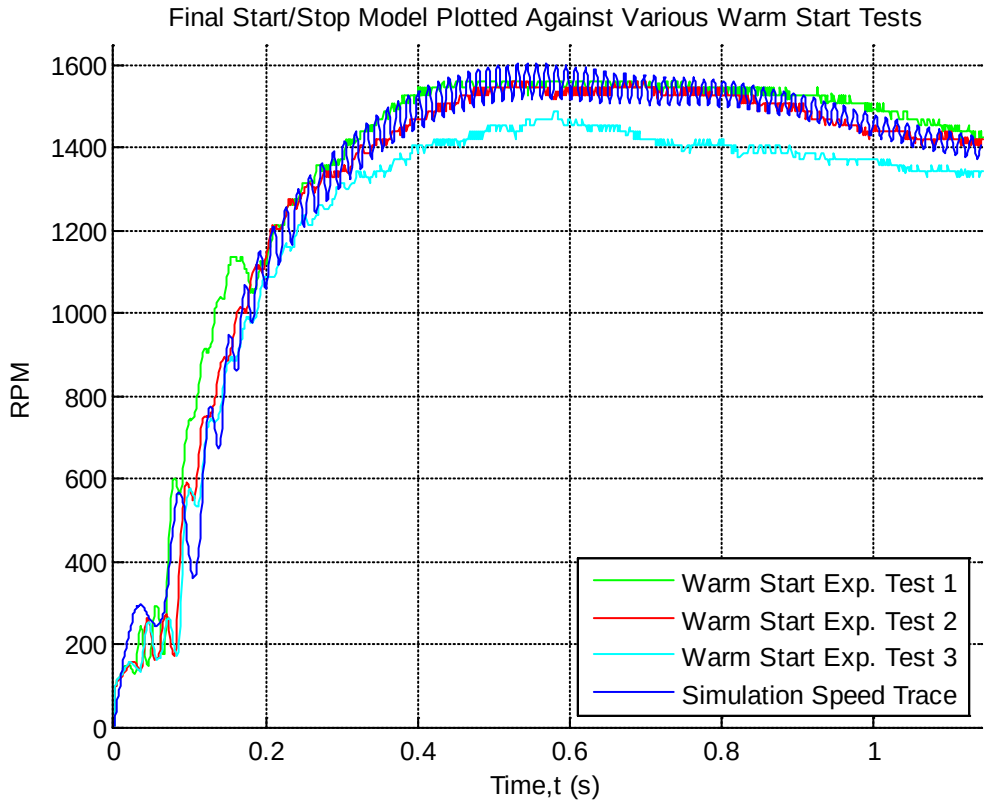

Figure 50: Start/Stop Model Validation against Warm Start Tests

Therefore, it was determined that the model could be used to analyze the fuel and battery energy consumption during the start transient. By adjusting the power of the starter, the cranking speed during the cranking phase was increased. This made it possible to observe what happened to the combustion gain, and after manipulation, the total fuel consumed during the start transient.

Chapter 4: Energy Analyses and Start Transient Optimization

4.1 Overview of Analyses

The purpose of the analyses covered in this chapter was to investigate and analyze the total energy consumption during the start transient using the startup dynamic model developed in Chapter 4. For each analysis, the energy consumption was broken down into two parts: the battery electrical energy consumed by the starter during the cranking phase and the fuel energy consumed in order to bring the engine to idle speed in the crank-to-run phase. After converting the electrical energy to fuel equivalent battery energy it was possible to compute and compare the total energy consumption of each analysis. For each analysis, the total fuel consumed per restart was also quantified and compared. Section 4.2 covers the procedure used to perform each of the analyses. Five different analyses were performed and the results are shown in Section 4.3. Section 4.3.1 covers four analyses for conventional start transients where the starter model torque and power were scaled to increase the engine speed during the cranking phase. Then, the simulated engine speed was matched to the warm start experimental speed trace during the crank-to-run phase. The result was that the CG decreased for the start transient. The analysis covered in Section 4.3.2 used the same concept of a implementing a high-power starter model during the cranking phase. However, for the crank-to-run phase, instead of matching the simulated engine speed to the high idle speed of the experimental start transient, the simulated speed was taken to the normal idle speed of 700 rpm as described in Section 2.3.2 . This optimized start transient eliminated the extra fuel consumption during the start transient.

4.2 Procedure for Analyses

The basic procedure used for all the analyses was to first pick a desired cranking speed, scale the starter torque and power to match the desired speed, then adjust the combustion gain to match the desired idle speed during the crank-to-run phase. Afterwards, the energy consumed during each phase was calculated, converted to equivalent fuel energy, and manipulated for comparison.

4.2.1 Scaling Starter Torque

To perform the analyses that follow, it was desired to investigate the effect of increasing the engine speed during the cranking phase. During the cranking phase the only torque applied to the crankshaft was the starter torque. The starter torque profile was increased by scaling the starter torque until the desired cranking speed was reached. The saturation limited starter model described and calibrated in Sections 3.2.3 and 3.3.2 was not used in the analyses because that would have required changing two parameters at once; namely the peak power and peak torque. Instead, a simpler approach was adopted by first linearly scaling the warm start experimental torque profile that was used to calibrate the starter model. Then, the mechanical power was determined from the scaled starter torque by equation (4.1) where N_{crank} was the mean speed during the cranking phase.

$$P_{mech}[W] = \frac{T_{starter}\ [Nm] \cdot 2\pi\ \left[\frac{rad}{rev}\right] \cdot N_{crank}\left[\frac{rev}{min}\right]}{60\ \left[\frac{s}{min}\right]} \tag{4.1}$$

Table 10 shows the scaled starter parameters for the 5 cases that were investigated in the analyses. The first case was a baseline case and had the same starter characteristics as the warm

start experimental data used for calibration in Section 3.3.2. The cases where the desired cranking speed was 500, 600, and 800 rpms were chosen arbitrarily. The case where the desired cranking speed was 700 rpm was chosen based off of the normal engine idle speed determined in Section 2.3.2.

Table 10: Scaled Starter Model Parameters

Desired Cranking Speed [RPM]	Scaling Factor	Peak Torque [Nm]	Peak Mechanical Power [kW]
250 (Baseline)	1	113	2.8
500	1.5	169	8.9
600	1.7	192	12.0
700	1.9	214	15.7
800	2.1	237	19.8

4.2.2 Combustion Gain Recalibration

After scaling the starter model, the simulated engine speed matched the desired cranking speed during the cranking phase for each analysis. Then the CG profile was recalibrated such that the simulated engine speed matched the desired engine idle speed during the crank-to-run phase. For the conventional start transient analyses the simulated engine speed trace was matched with the warm start experimental speed trace shown in Figure 46 for the crank-to-run phase. The optimized start transient crank-to-run phase, simulated speed was matched to the normal engine idle speed of 700 rpm as discussed in Section 2.3.2.

4.3 Analyses Results

This section shows the results of the analyses performed and shows how the battery and fuel energy were determined from the model.

4.3.1 Conventional Start Transients

The electrical power consumed by the starter for the various desired cranking speeds is shown in Figure 51. The electrical power consumed by the starter was equal to the electrical power drained from the battery during the cranking phase. The starter mechanical power shown in Table 10 was converted to electrical power by using a constant efficiency of 90% for all of the analyses performed. This efficiency was adopted from the motor efficiency provided by Chrysler as discussed in Section 2.3.2.

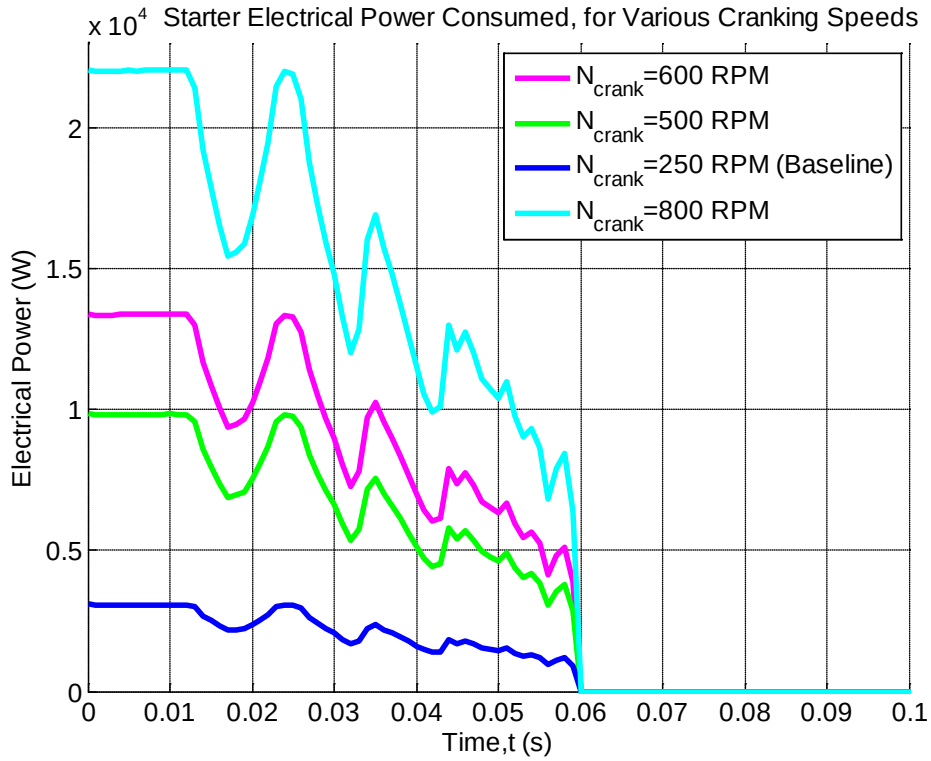

Figure 51: Electrical Power Consumed during Cranking

The electrical energy consumed during the cranking phase was quantified for each analysis by time integration of the electrical power consumption over the duration of the cranking phase, which is shown in equation (4.2).

$$E_{elec}\,[J] = \int_{0\,s}^{0.06\,s} P_{elec}[W]\;dt \tag{4.2}$$

After the simulated engine speed was matched to the desired speed during the cranking phase, the simulated speed matched to the warm start experimental speed trace during the crank-to-run phase. The resulting start transients for all of the conventional restart analyses are shown in Figure 52.

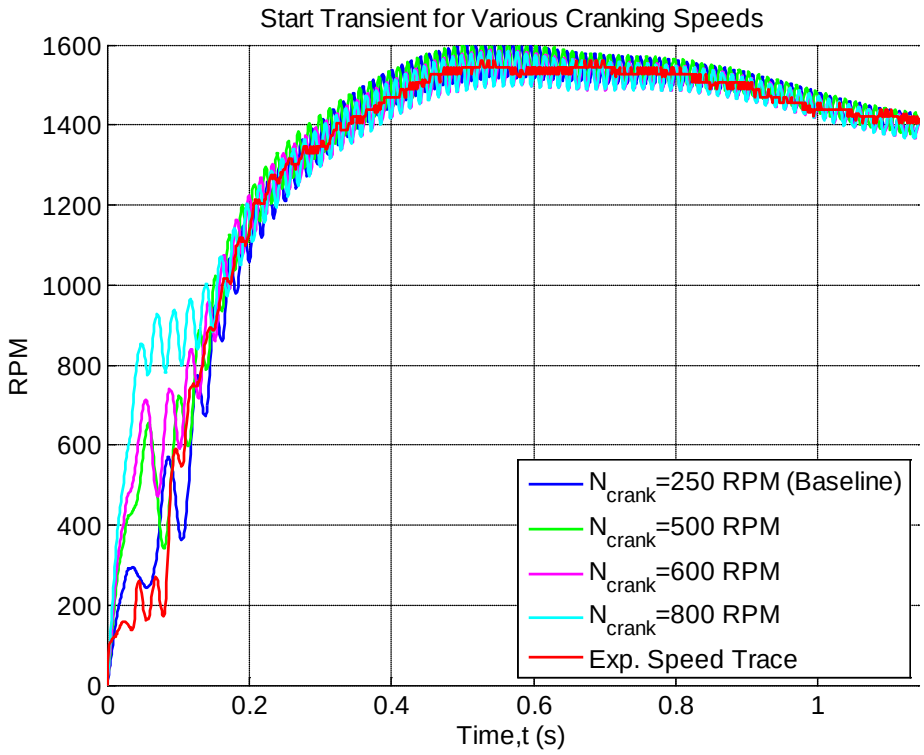

Figure 52: Start Transients for Conventional Restarts

In order for the simulated speed trace to match the experimental speed trace during the crank-to-run phase, the model CG profile had to be recalibrated. The result is shown in Figure 53. The figure shows that the fuel consumption, trending like the CG, decreased as the starter power

increased. This trend is true in general for any start transient and was applied in order to develop the optimized start transient analysis of Section 4.3.2.

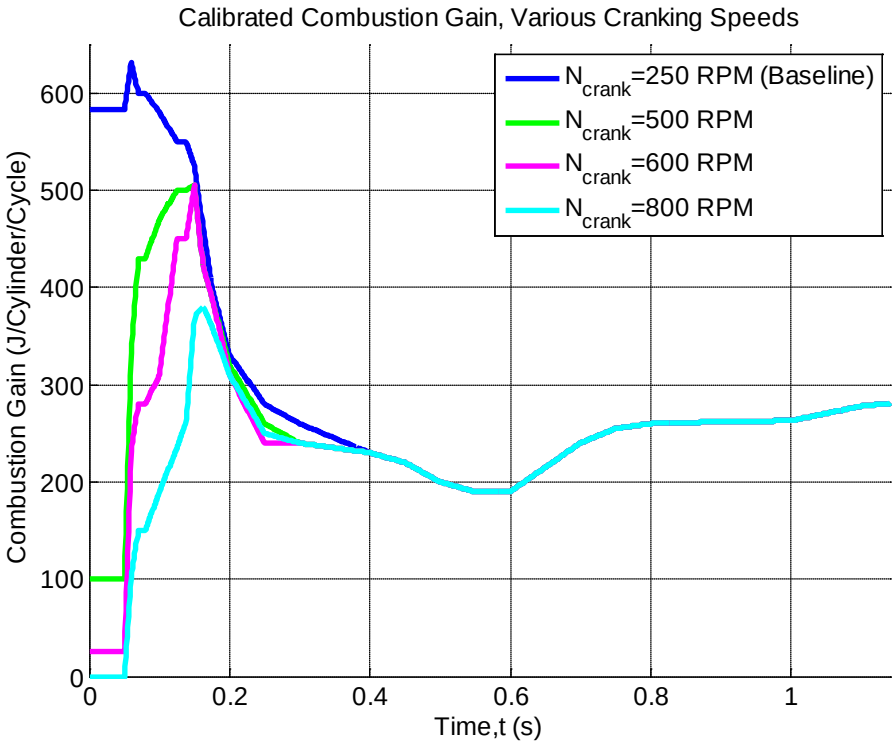

Figure 53: Recalibrated CG for Conventional Restarts

The recalibrated CG was converted to fuel flow rate for each analysis based on rearranging equation (3.17) to solve for the fuel flow rate as shown in equation (4.3).

$$\dot{m}_{fuel}[kg/s] = \frac{CG[J/Cylinder/Cycle] \cdot N_{RPM}}{20\eta_f Q_{LHV}} \tag{4.3}$$

In equation (4.3), N_{RPM} was the instantaneous simulated engine speed and η_f was the fuel conversion efficiency determined using equation (3.18). For each analysis, the mass of fuel consumed was found by time integration of the fuel flow rate over the duration of the start transient and is shown in equation (4.4).

$$M_{fuel}\,[kg] = \int_{0\,s}^{1.14\,s} \dot{m}_{fuel}\,[kg/s]\;dt \tag{4.4}$$

Knowing the mass of fuel consumed, the fuel energy consumed during the start transient was calculated based on equation (4.5) .

$$E_{fuel}\;[J] = M_{fuel}[kg] \cdot Q_{LHV}[J/kg] \tag{4.5}$$

An accurate comparison of the total energy consumed during the conventional restart analyses can be made by summing the electrical and fuel energy consumption for the cranking and crank-to-run phases. However, the battery electrical energy is not physically equivalent to the fuel energy. To make them equivalent, it was necessary to convert the electrical energy to fuel equivalent battery energy by a chain of efficiencies that accounts for energy losses and energy transfer throughout the vehicle. Essentially, the energy consumed from the battery must be replenished by fuel energy via the engine and the alternator. An overall efficiency of 13% was determined and is presented in equation (4.6) where the battery energy conversion efficiency $\eta_{battery}$ was 98%, the alternator efficiency $\eta_{alternator}$ was 67% [22], and the fuel conversion efficiency η_f was 20% as calculated using equation (3.18).

$$\eta_{overall} = \eta_{battery} \cdot \eta_{alternator} \cdot \eta_f \tag{4.6}$$

The electrical energy consumed during the start transient was converted to fuel equivalent battery energy using equation (4.7)

$$E_{fuel\,equiv}\;[J] = \frac{E_{elec}[J]}{\eta_{overall}} \tag{4.7}$$

Finally, the battery weighted fuel energy, or more simply, the total energy consumed during the start transient was found by summing the fuel energy and the fuel equivalent battery energy. The total fuel consumed during each conventional restart was found by dividing the total energy by the lower heating value of gasoline. Equation (4.8) shows both the total energy consumption and the total fuel consumption for the start transient.

$$M_{fuel_{total}}\,[kg] = \frac{E_{fuel}[J] + E_{fuel\,equiv}\,[J]}{Q_{LHV}[J/kg]} = \frac{E_{total}\,[J]}{Q_{LHV}[J/kg]} \tag{4.8}$$

Table 11 shows a summary of energy and fuel consumption for each of the conventional start transients analyzed in this section. Although the fuel energy consumed decreased as the electrical energy consumed increased, the total energy and fuel consumed did not follow this trend due to the weighting of battery energy using the chain of efficiencies described in equation (4.6).

Table 11: Energy and Fuel Consumption for Conventional Restart Analyses

Cranking Speed [RPM]	Electrical Energy Consumed [A-h]	Electrical Energy Consumed [J]	Fuel Equivalent Battery Energy [J]	Fuel Energy Consumed [J]	Total Energy Consumed [J]	Total Fuel Consumed [kg]
250 (Baseline)	2.59E-03	130.7	995.3	98780	99775.3	2.268E-03
500	8.27E-03	417.0	3175.4	97160	100335.4	2.280E-03 (+0.53%)
600	1.13E-02	567.1	4318.5	94280	98598.5	2.241E-03 (-1.19%)
800	1.85E-02	934.0	7112.4	91810	98922.4	2.248E-03 (-0.88%)

The total fuel consumed was smallest for the case where cranking was 600 rpm. The case with 500 rpm cranking increased fuel consumption compared to baseline, and 800 rpm cranking did not reduce overall fuel consumption as much as the 600 rpm case.

4.3.2 Optimized Start Transient

For the optimized start transient described in this section a different restart strategy was adopted for the start transient. It is typical in start/stop applications to utilize a belted starter alternator (BSA) as the system component to restart the engine and recharge the battery. Besides functioning as a high-power starter, the BSA has increased flexibility over a conventional alternator in that it can harvest more energy during braking than a conventional alternator due to its increased power output and efficiency [29] [30]. To harvest this energy, the BSOC is kept below 100% while driving. This is because the dynamic charge acceptance (DCA) of the battery is inversely proportional to the BSOC [31]. Therefore, when the engine is restarted during a start/stop event it is not necessary to command the alternator duty cycle to recharge the battery immediately after startup as was observed in the current vehicle operating strategy covered in Section 2.3.2. This means that the high idle speed maintained after the start transient can be eliminated and that the engine can be restarted to the normal idle speed of 700 rpm.

By taking the engine straight to idle speed during the cranking phase with a high-power starter alone, it was only necessary to inject enough fuel to keep the engine at idle speed. The resulting optimized start transient is shown in Figure 54. The optimized start transient considerably reduced the time to restart the engine. For the conventional restart, extra fuel was injected to rapidly increase the engine speed once the crank-to-run phase began. In the optimized start transient, the crank-to-run phase was eliminated since extra fuel injection was not necessary. This operating technique can be utilized so long as the partial-BSOC is maintained to within an acceptable range. Numerous restarts within a short time frame will cause the BSOC to fall

outside of the acceptable range, and then it will be necessary to run the engine in order to recharge the battery.

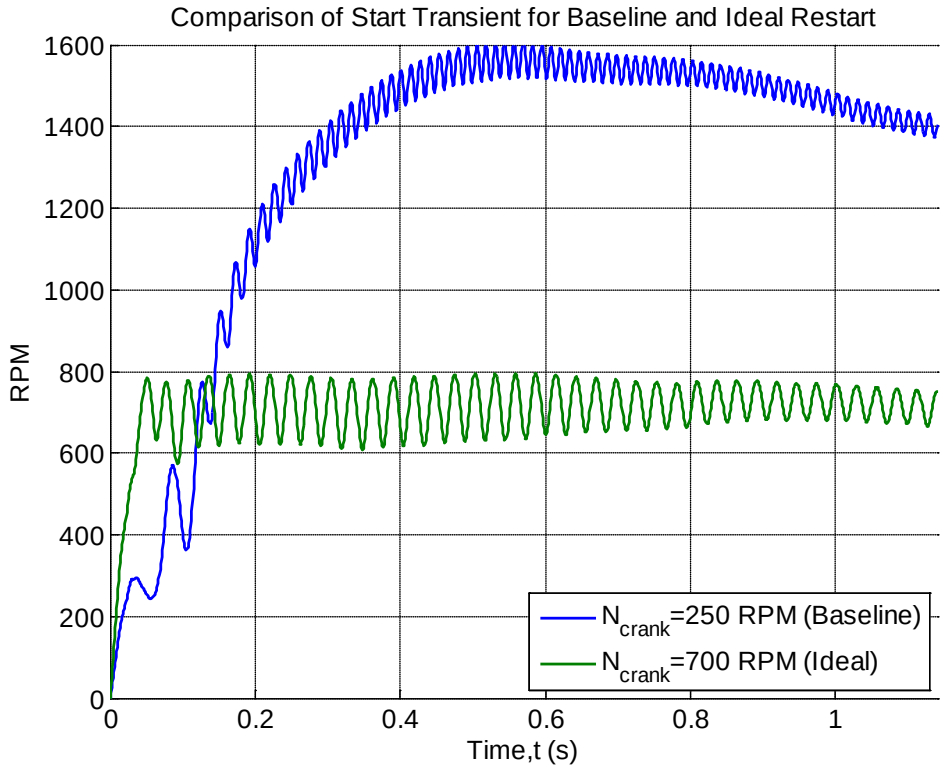

Figure 54: Start Transient for Ideal and Baseline, Conventional Restart

For the optimized start transient it was assumed that a BSA's operating characteristics were comparable to the starter on the minivan and that a linear scaling of the start torque and power was acceptable. The desired engine speed during the cranking phase was selected so that the starter provided enough torque to bring the engine to idle speed before fuel injection and the first firing event. Table 10 shows the scaled starter model parameters needed to achieve the desired 700 rpm cranking speed. Figure 55 shows the electrical power consumed during the cranking phase, which was found using a constant efficiency of 90% from the scaled mechanical power

profile. The mechanical power profile was found by applying equation (4.1) to the scaled warm start experimental torque profile.

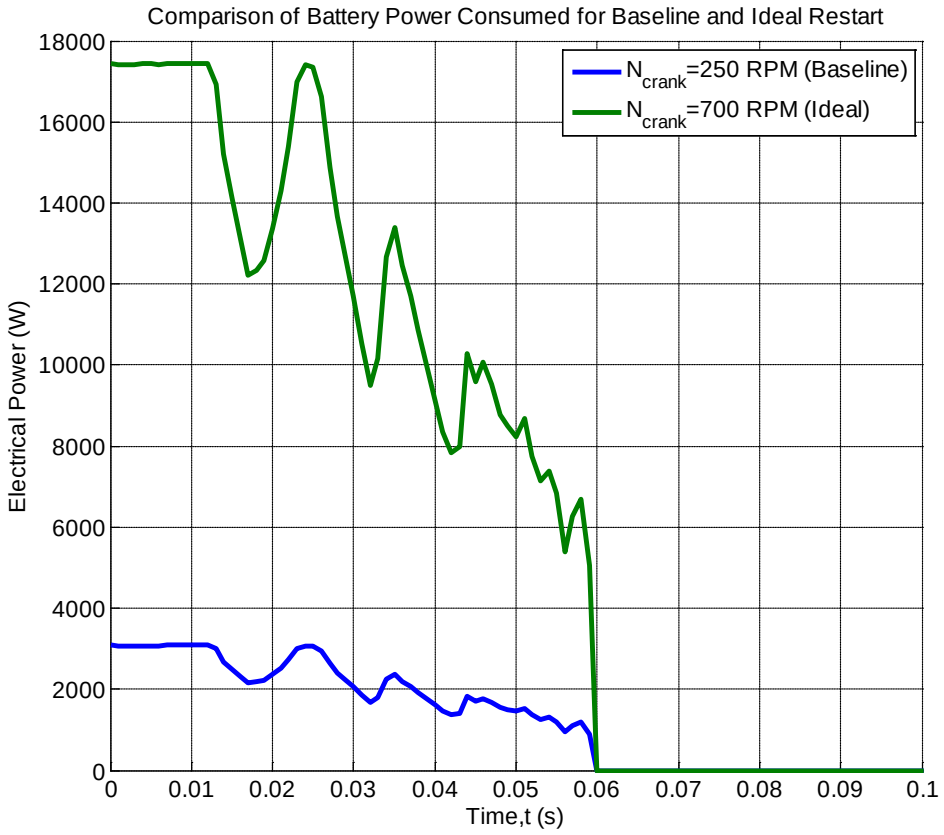

Figure 55: Electrical Power Consumed for Ideal and Baseline, Conventional Restart

The CG profile of the optimized start transient was recalibrated and is shown in Figure 56. Because the starter brought the engine speed to idle during the cranking phase, the extra fuel consumed in the beginning of the start transient was eliminated and it was possible to inject only enough fuel to keep the engine speed at 700 rpm.

For the optimized restart, equations (4.2) through (4.8) were applied to calculate the battery and fuel energy consumption. The battery electrical energy was converted to fuel equivalent battery energy and totaled with the fuel energy to quantify the total energy consumed. The total energy

was converted to the total amount of fuel consumed during the ideal restart. These results are shown in Table 12. Using the ideal restart, there was a 63% decrease in the total fuel consumed compared to baseline case.

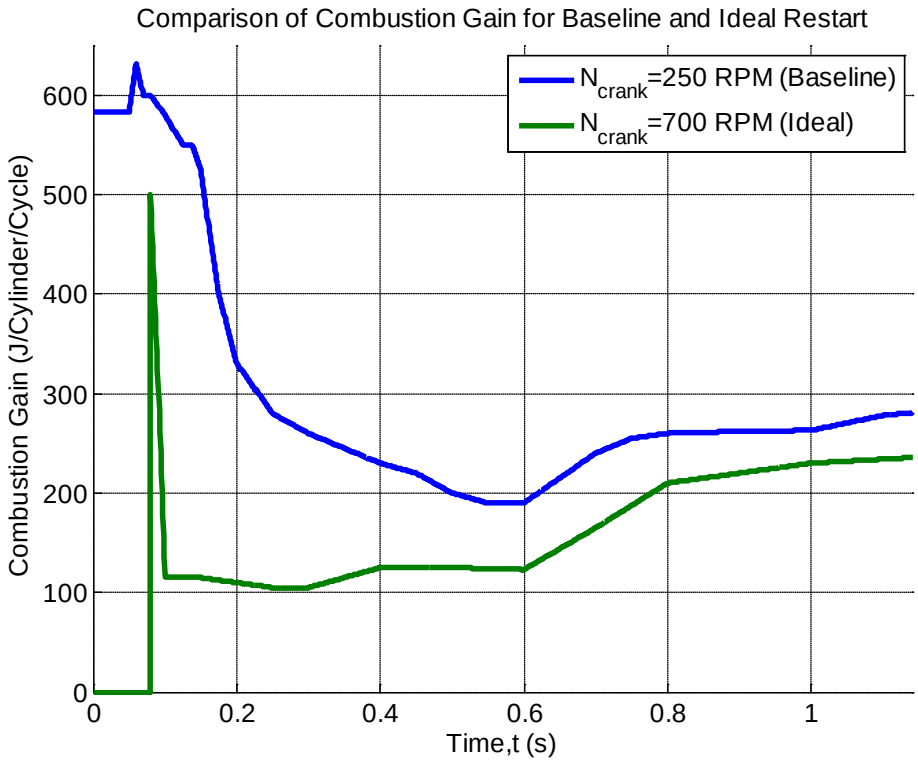

Figure 56: Combustion Gain for Ideal and Baseline, Conventional Restart

Table 12: Energy and Fuel Consumption for Ideal and Baseline, Conventional Restart

Cranking Speed [RPM]	Electrical Energy Consumed [A-h]	Electrical Energy Consumed [J]	Fuel Equivalent Battery Energy [J]	Fuel Energy Consumed [J]	Total Energy Consumed [J]	Total Fuel Consumed [kg]
250 (Baseline)	2.59E-03	130.7	995.3	98780	99775.3	2.268E-03
700	1.47E-02	739.4	5630.5	31260	36890.5	8.384E-04 (-63.03 %)

4.4 Start/Stop Fuel Economy Improvement for FTP Cycle

Section 1.5 discussed the Environmental Protection Agency's FTP cycle that is used to determine a vehicle's standardized FE and emissions. As explained in Section 1.4, the VES is a forward-looking, energy-based modeling tool created by OSU CAR in order to simulate the 2011 Chrysler Town and Country's powertrain and auxiliary systems. By running the VES over the first 1370s of the FTP cycle it was possible to show an estimated FE improvement of almost 8% by using start/stop and is shown in Table 3. This estimate was determined by making the fuel flow rate of the baseline case shown in Figure 8 equal to zero during every engine idling period in the cycle [21]. Any time idling occurred during the cycle it was used as an instance for a start/stop event. There were 18 instances where the fuel flow rate was made equal to zero during the UDDS portion of the FTP cycle. By accumulating the fuel saving for each instance it was possible to quantify the decrease in cumulative fuel use for SS $M_{fuel_{savedSS}}$, the percent decrease in FC $\%\Delta FC$, and also the percent FE improvement $\%\Delta FE$ using SS over the baseline. The calculation of these parameters is explained in Section 1.5 by equations (1.1) to (1.5) respectively. The calculated values are shown respectively in columns 1 through 3 of Table 3. The resulting 8% FE improvement was only an estimate because this analysis did not account for the FC required for restarting the engine after every start/stop event.

The FC per restart $M_{fuel/restart}$ is equal to the total fuel consumed $M_{fuel_{total}}$ quantified in Section 4.3 in equation (4.8) for the conventional and optimized start transients and is shown in the last column of Table 11 and Table 12. From this point forward, the conventional restart refers only to the baseline analysis performed in Section 4.3.1. In order to quantify the actual FE

improvement for SS on the UDDS it was necessary to calculate the actual decrease in cumulative fuel use $M_{fuel_{cumulative}}$ when accounting for the FC per restart from the conventional and optimized restart over the UDDS portion of the cycle. This was found by using equation (4.9).

$$M_{fuel_{cumulative}}[kg] = M_{fuel_{savedSS}}[kg] - M_{fuel/restart}[kg] \cdot N_{restarts} \quad (4.9)$$

In equation (4.9), the number of restarts $N_{restarts}$ had to be determined for both the conventional and optimized restart over the UDDS. The number of restarts was quantified by considering the tradeoff between FC per restart and the FC if the engine were to remain idling instead of using SS. The tradeoff time $t_{tradeoff}$ is shown in equation (4.10) where $\dot{m}_{fuel_{idle}}$ was the fuel flow rate of the vehicle at the normal 700 rpm idle speed.

$$t_{tradeoff}[s] = \frac{M_{fuel/restart}[kg]}{\dot{m}_{fuel_{idle}}[kg/s]} \quad (4.10)$$

The tradeoff time for the conventional restart was 6.2 seconds and 2.3 seconds for the optimized restart. Therefore, it was possible to determine the number of realizable restarts during the UDDS by making the fuel flow rate zero only when the idle events lasted longer than the tradeoff time. For the conventional restart there were 12 instances where the idling time was longer than the tradeoff time, and for the optimized restart there were 14 possible start/stop instances.

After calculating the decrease in cumulative fuel use for both restart cases considered it was possible to make a more accurate determination of the percent decrease in FC and percent increase in FE by applying equations (1.3) and (1.5). The results are shown in Table 13.

Table 13: Start/Stop Fuel Savings over FTP Cycle Accounting for Restart Fuel Consumption

	Decrease in Cumulative Fuel Use [kg]	Decrease in Fuel Consumption [%]	Increase in Fuel Economy [%]	Accounts for Fuel to Restart
VES Estimate	0.0842	7.3680	7.9540	No
Conventional Start	0.0434	3.7998	3.9499	Yes
Optimized Start	0.0691	6.0531	6.4431	Yes

The analyses performed in this chapter were used to quantify the FC per restart event using a conventional and an optimized restart transient. The analyses were carried out on the engine startup dynamic model developed in Chapter 4. The FC per restart was taken into account over the UDDS portion of the FTP cycle in order to show the actual increase in FE using SS technology in the 2011 Chrysler Town and Country minivan. The conventional restart strategy showed a 4% increase in FE, while the optimized restart strategy showed almost a 6.5% increase.

Chapter 5: Conclusion and Future Work

5.1 Summary and Conclusion

This work investigated the use of start/stop (SS) technology as a means of increasing vehicle fuel economy (FE) for the 2011 Chrysler Town and Country minivan. An ideal 8% increase in FE was estimated during the EPA Urban Drive Cycle using CAR's Vehicle Energy Simulator (VES) to compare the fuel consumption (FC) of the minivan for a baseline case and one where start/stop was enabled. However, this result did not account for the energy required to restart the engine after the elimination of each idle event. The analysis was used as motivation for investigating start/stop technology as means to significantly increase the FE of the vehicle. Experimental data from three vehicle start transients were collected for keyed starts with the vehicle at fully warmed conditions. The results were compared, analyzed, and broken down into separate events. A model of the startup dynamics was created to further investigate the energy consumption during the start transient. The model was calibrated and validated using the experimental data collected. By separating the start transient into two main phases, the cranking phase and the crank-to-run phase, it was possible to separate the battery energy and fuel energy. Various starter/battery combinations were considered by scaling the baseline start transient starter torque and power in order to increase the engine speed during the cranking phase. This resulted in decreased fuel consumption during the start transient since less fuel energy was required to bring the engine to idle speed during the crank-to-run phase. The battery and fuel energy were combined for an ideal and conventional start transient and the result was quantified as the FC per restart. The product of each restart FC and the number of plausible start/stop

events was subtracted from the ideal fuel saving over the EPA UDDS. The conventional start process penalized the ideal fuel savings by 50%, whereas the optimized restart only penalized the ideal fuel saving by 20%. By using a high-power starter to bring the engine speed directly to idle during the cranking phase, it was possible to realize an optimal start transient where the extra fuel consumed due to the conventional starting process was eliminated. A FE improvement of over 6% is achievable for the Chrysler Town and Country using this start/stop strategy to eliminate idling losses during the EPA Urban Drive Cycle.

5.2 Future Work

In the future, it is likely that a start/stop system will be implemented on the test vehicle. Before it will possible to properly select components for the system and develop the controls for the system, it will be necessary to refine experimental testing and the startup dynamic model developed in this work.

5.2.1 Experimental and Modeling Refinement

One way to reduce the model error and better capture the low speed engine dynamics would be to improve the friction torque model. A simple approach to increase the friction torque accuracy of the model for low engine speeds would be to perform a stop transient calibration by matching the model speed trace to a few experimental stop transients that start at a few different idle speeds. This will allow an additional friction coefficient to be obtained for low speeds and will yield a better CG calibration. A more sophisticated way to improve the friction model would be to design an experimental test to measure the friction in the crank domain. Developing a crank

angle based friction torque model [25] would significantly improve the model accuracy during the cranking phase.

Proper selection of the high-power starter for the SS system is imperative for a fast, smooth, and efficient startup. To get a better idea of the starter needed for SS, Willans line approach [24] [27] could be applied to the starter model to scale the starter torque-speed curve instead of using a linear scaling of the experimental starter torque. Experimental testing could be used to obtain a more appropriate starter model. By placing a current shunt on the starter, the power consumption of the starter can be captured directly from the vehicle DAQ, instead of inferring the starter current and power from the battery and alternator current. This would help to better characterize the starter. The vehicle starter motor could also be characterized by testing the operating regime of the starter on a test bench setup.

The locations of the pumping loss peaks during the cranking phase are dependent on the initial angular position of the crankshaft. Using the crank encoder signal bypassing the ECU, it is possible to experimentally determine the initial position of the crankshaft before a startup by knowing the geometric construction of the engine crankshaft, crank encoder wheel, piston pin locations, and TDC relationships. Using this knowledge in conjunction with the engine stop estimator scheme depicted in [32] the benefits are twofold. First, the engine startup dynamics can be more accurately depicted during the cranking phase with an accurate initial condition for the crankshaft dynamics model. Second, using the stop estimator and the crank encoder hall-effect sensor information it is possible to restart the engine more quickly after a start/stop event than compared to a normal keyed start because the vehicle electronics/ECU remain electrified, which means the crankshaft position during the stop can be found. The ECU can then inject fuel

into the next closest cylinder to fire without having to reestablish the TDC locations. This tactic can be used in the development of the start/stop controls to reduce NVH and the restart time [18].

5.2.2 Start/Stop Component Selection and Control Development

Once the refinements mentioned above are made, the model can be exercised in number of ways to select SS components and develop controls.

It is possible to couple the engine startup dynamics model with the electrical system model developed in [22] for the Chrysler minivan. The startup model is capable of suggesting the starter component characteristics in terms of power and torque, but is not capable of suggesting battery selection criteria like nominal voltage and peak current output needed for a robust start/stop system. Pairing the two models would allow the main SS system components, the starter and battery combination, to be properly selected for successful integration with the other vehicle auxiliary loads that would also be electrified during a stop event [13] [33]. After selecting the proper battery characteristics for the SS system, CAR's battery testing cells could be used to explore the effects of SS operation on battery health, aging, partial-BSOC, DCA, and other important battery parameters. The battery analysis could be performed on various battery chemical compositions including conventional lead-acid, AGM lead-acid, Ni-Cd, NiMH, and Li-ion batteries to determine the most suitable battery composition for SS operation. The starter life is another parameter that would need to be considered in the component selection process.

In terms of controls for a SS system, a closed-loop controller is needed for the starter operation in order to eliminate the NVH signature and to acquire a quick speed of response during engine cranking. The equivalent consumption minimization strategy (ECMS) controller [22] for the alternator or BSA duty cycle would need to be redesigned to include a battery charging strategy

that incorporated regenerative braking as in [4] [14] [18]. In order to avoid NVH and vehicle lurching it would be necessary to add/modify controls for the vehicle transmission [5] [6] and electrified auxiliary loads [13]. Lastly, the paired startup dynamic model and electrical system model could be used to develop a logic algorithm for the supervisory controller to manage the start/stop operation in conjunction with the tasks it normally oversees.

References

[1] U.S. Department of Energy website. (2011). “Vehicle Fuel Economy and Greenhouse Gas Emissions Standards,” http://www.afdc.energy.gov/afdc/laws/law/US/385.

[2] National Highway Traffic Safety Administration website. (2012). “Obama Administration Finalizes Historic 54.5 mpg Fuel Efficiency,” http://www.nhtsa.gov/fuel-economy/.

[3] Chiara, F., M. Canova, and G. Rizzoni. *Future Mobility Challenges, Where Will We Find Fuel Efficient Solutions?* 24 April 2012. Print.

[4] Gao, B., K. Svancara, and A. Walker. (2009). “Development of a BISG Micro-Hybrid System.” SAE Paper 2009-01-1330.

[5] Bishop, J., Nedungadi, A., et al. (2007). “An Engine Start/Stop System for Improved Fuel Economy.” SAE Paper 2007-01-1777.

[6] Robinette, D., and M. Powell. (2011). “Optimizing 12 Volt Start-Stop for Conventional Powertrains.” SAE Paper 2011-01-0699.

[7] “Ford Concentrates on Control Strategies for Low-Cost Start-Stop System for Fusion.” *Green Car Congress*. 19 July 2012. Web.

[8] Schaeck, S., A. O. Stoermer, and E. Hockgeiger. “Micro-Hybrid Electric Vehicle Application of Valve-Regulated Lead-Acid Batteries in Absorbent Glass Mat Technology: Testing a Partial-State-of-Charge Operation Strategy.” *Journal of Power Resources* (2008). Print.

[9] Hawkins, S., F. Billotto, et al. (2012). “Development of General Motors’ eAssist Powertrain.” SAE Paper 2012-01-1039.

[10] Samarins website. Accessed March, 2013. “Starting system, Starter motor,” http://www.samarins.com/glossary/starter.html.

[11] Canova, M., Y. Guezennec, and S. Yurkovich. (2004). “On the Control of Engine Start/Stop Dynamics in a Hybrid Electric Vehicle.” GATE Presentation. The Ohio State University, Center for Automotive Research.

[12] Nichols, W.G. Chilton’s Easy Car Care. (1998). “The Starting System,” Accessed March, 2013 from Green Light Auto Care website, http://www.greenlightautocare.com/shared/Library/encyclopedia/resourcecenter_encyclopedia_starting1.asp.

[13] Prucka, M. (2005). “Development of an Engine Stop/Start at Idle System.” SAE Paper 2005-01-0069.

[14] Ferrari, A., E. Morra, and E. Spessa. (2011). “Analysis of Energy-Efficient Management of a Light-Duty Parallel-Hybrid Diesel Powertrain with a Belt Alternator Starter.” SAE Paper 2011-24-0080.

[15] Guezennec, Yann. "Secondary Energy Storage: Batteries." ME784 Lecture. The Ohio State University, Columbus, OH. Lecture.

[16] Reese, R. (2012) “A MultiAir/Multifuel Approach to Enhancing Engine System Efficiency.” Presentation. Chrysler and U.S. Dept. of Energy, ACE062.

[17] Canova, M., Guezennec, Y., and Yurkovich, S., 2009, “On the Control of Engine Start/Stop Dynamics in a Hybrid Electric Vehicle.” Journal of Dynamic Systems, Measurement, and Control.

[18] Furushou, M., Nishizawa, K., et al. “Stop-Start System with Compact Motor Generator and Newly Developed Direct Injection Gasoline Engine.” *SAE Int. J. Engines* 4(16):2012, doi:10.4271/2012-01-0410.

[19] Agarwal, Neeraj. “Modeling, Validation and Analysis of an Advanced Thermal Management System for Conventional Automotive Powertrains.” Thesis. The Ohio State University, 2012. Print.

[20] Merical, Kyle. “Model-Based Multi-Variable Control Development for an Advanced Thermal Management System for Conventional Automotive Powertrains.” Thesis. The Ohio State University, 2013. Print.

[21] Grimm, Benjamin. “Modeling and Analysis of Crankshaft Energy Harvesting for Vehicle Fuel Economy Improvement.” Thesis. The Ohio State University, 2012. Print.

[22] Couch, Jeremy. “An ECMS-based Control Strategy for the Electrical System of a Conventional Vehicle.” Thesis. The Ohio State University, 2013. Print.

[23] “Federal Test Procedure Revisions.” *Environmental Protection Agency.* Web. 27 Jan. 2013.

[24] Heywood, J. B. *Internal Combustion Engine Fundamentals*. New York: McGraw-Hill, 1988. Print.

[25] Chiara, Fabio. “Module 2: Mechanical Modeling.” ME 730 Lecture. The Ohio State University, 2011.

[26] Chiara, Fabio. “Module 3: Combustion Modeling.” ME 730 Lecture. The Ohio State University, 2011.

[27] Canova, M., Sevel, K., Guezennec, Y., and Yurkovich, S., 2006, “Control of the Start/Stop of a Diesel Engine in a Parallel HEV: Modeling and Experiments,” *Proceedings of the ASME International Mechanical Engineering Congress and Exposition*.

[28] Rizzoni, Giorgio. “ElectroMechanical Systems.” ME 482 Lecture 17. The Ohio State University, 2012.

[29] Venkkateshraj, A. V. K., B. Vijayakumar, V. Narayanan, and K. R. Anandakumaran Nair. (2007). “High Power and High Efficiency Alternators for Passenger Cars.” SAE Paper 2007-26-058.

[30] Perreault, D., and V. Caliskan. (2004). “Automotive Power Generation and Control.” IEEE Transactions on Power Electronics. Vol. 19, No. 3 May, 2004.

[31] Schaeck, S., A. O. Stoermer, J. Albers, et al. “Lead-acid batteries in micro-hybrid applications. Part II. Test Proposal.” *Journal of Power Resources* (2010). Print.

[32] Mueller, M. “Engine Stop Position Estimation.” *SAE Int. J. Engines* 5(2):2012, doi:10.4271/2012-01-0720.

[33] Knorr, R. (2011). “Start/Stop Systems on the Home Straight.” ATZ: Industry Assistance Systems, Vol. 113, September, 2011.